UNIVERSITÀ
DEGLI STUDI
DI PADOVA

UNIVERSITÀ DEGLI STUDI DI PADOVA

Department of Civil, Environmental and Architectural Engineering

Master degree in Environmental Engineering

Master thesis

Geomechanical simulation of underground gas storage in a faulted reservoir: a case study in northern Italy

Supervisor

Prof. Eng. Pietro Teatini

Co-supervisors

Prof. Eng. Massimiliano Ferronato

Dr. Andrea Franceschini

Candidate

Valentina Maoret

2013906

Academic Year 2021/2022

Abstract

Underground gas storage (UGS) is a very common practice currently adopted to meet the growing energy demand, especially in North America and Europe. The gas is stored in reservoirs through a seasonal cycle of injection and removal. Factors such as the reservoir depth, the pressure change, and the geomechanical properties of the soil control the expansion and contraction of the reservoir and, consequently, the movements of the land surface. Furthermore, faults may exist and, as a result of pressure variations, they might be reactivated, raising several safety and economical issues due to the induced seismicity phenomena. For these and many other reasons, a geomechanical simulation of the soil response during UGS activities is of paramount importance.

In this work, the simulation of a case study in northern Italy is performed applying a one-way coupled modeling approach with the Finite Element method that is used to solve the partial differential equations of the flow and the equilibrium. The geomechanical simulator is calibrated using land movements provided by an interferometric synthetic aperture radar (InSAR) technique. The aim of the study is the analysis of the geomechanical response of the system mainly during the storage cycles, with a particular attention to the possible fault reactivation.

The model outcomes show that the displacements associated to the UGS cycles do not exceed 4 mm, both in the vertical and horizontal directions, and are concentrated above the center of the reservoir. Moreover, the maximum displacements will remain limited to 5 mm also in scenarios of future development, when the pressure change during the injection-production phases will be larger than those experienced during the last years. The stress field change caused by the UGS activity does not propagate more than 20 m above the top of the unit used for UGS activities, and also the horizontal propagation within the aquifer hydraulically connected to the reservoir is limited. The safety factor for the regional faults remains equal to 0.1, in a range [0,1] where 0 is the safest condition, leading to the conclusion that UGS activities in this reservoir cannot be responsible of induced seismicity.

Contents

List of Figures

List of Tables

Chapter 1

Introduction

The current gas crisis is highlighting the importance of a strategy able to assure its constant supply. For this reason, techniques such as underground gas storage (UGS) are gaining popularity among the general public nowadays. This practice is very common and has already been adopted to meet the growing energy demand especially in North America and Europe where the number of UGS plants at the end of 2017 was 450 and 142, respectively (Cornot-Gandolphe [2018]). The basic aim behind this activity is that huge quantities of gas must be stored during periods of low demand and then reintroduced in the supply system when it is more needed. However, the construction of specific surface storage infrastructures is very expensive, unsafe and, possibly, highly impacting on the surrounding environment. Hence, a different solution is needed and it was found in the use of depleted underground reservoirs where the gas is stored through a seasonal cycle of injection and removal.

However, the implementation of UGS activities can lead to environmental impacts, in particular geomechanical issues both on the land surface and subsurface (Teatini et al. [2011]). Factors such as the reservoir burial depth, the change of pressure, and the geomechanical properties of the soil rule the expansion and contraction of the reservoir layer and the related uplift and settlement movements of the land surface. Furthermore, if faults exist in the reservoir surroundings, they might be reactivated, creating problems of induced seismicity, or also new fractures may activate because of the change of the natural stress regime caused by the pressure change within the reservoir and the connected geologic layers.

The geomechanical simulation of the soil response during UGS activities is of great importance. With proper simulators the behaviour of the reservoir and and nearby

faults can be analyzed during the whole period of the working life of the reservoir.

Numerical models are generally based on the Finite Element method that allow to solve the partial differential equations governing the problem. Two different models are considered in the case of interest: a flow model, which is used to propagate the pressure variations from the reservoir into the hydraulically connected aquifers, and a geomechanical model that allows quantifying the displacement and stress variations due to the storage activity. This approach was already been implemented in many works related to reservoirs studies such as Gambolati et al. [1984], Ferronato et al. [2004], Teatini et al. [2011] and Orlic et al. [2013]. Moreover, the use of land measurements made available by interferometric synthetic aperture radar (InSAR) allows to calibrate the model parameters, similarly to what was utilised in previous papers, such as in Teatini et al. [2011] and Ferronato et al. [2013].

In this thesis, the Finite Element model is firstly presented and then applied to a real case study located in northern Italy. Stogit S.p.A., the company managing the reservoir, has provided the basic information about field and data regarding reservoir pressure and land displacements. The modeling approach properly accounts for the presence of several local discontinuities and regional faults in the reservoir area through the use of Interface Elements. The thesis initially investigates the mechanical response of the continuous system during the primary production and the UGS cycles and then analyzes the possible fault reactivation.

In Chapter 2, a site description, with the main geological information, the production history, and the available data are presented. Then, the mathematical and numerical models used to describe and solve the flow and geomechanical problems are introduced in Chapter 3. In Chapter 4, the simulation framework is applied to the study case and the main outcomes are presented and discussed. Finally, Chapter 5 contains some some conclusions and future prospects.

Chapter 2

Site description

Stogit S.p.A., which is part of the main group Snam S.p.A., has the control over the main underground gas storage sites in Italy (Figure 2.1). Since the middle of the 20th century, numerous gas and oil reservoirs have been found in northern Italy, in the area of the Po river plain which is bounded by the Alps to the West and North, the Apennines to the South, and the Adriatic Sea to the East.

The site analyzed in this thesis, which is located in this region, was discovered in 1948 and was initially employed for primary production, mainly of gas; however, the exploitation of the original hydrocarbons nearly wiped out the reservoir, which was later interested in conversion into an underground gas storage field (Figure 2.2). The stratigraphic layer of interest is at a depth of 1400-1600 m below mean sea level and is composed of two distinct hydraulically separated porous levels called respectively, starting from the shallower to the deeper, Pool A and Pool C.

2.1 Geological framework

Based on the geological study report provided by Stogit S.p.A., the reservoir is situated within the deposits of the sands of the Late Messinian. The formation has settled inside a piggyback basin partially isolated by the Apennines foredeep during the end of the Miocene.

The structural asset of this part of the Po river plain is connected with the evolution of the buried Apennines chain. The deformation events involved the whole formation of the Cenozoic sedimentation and only in part the Mesozoic underlayer developing a

FIGURE 2.1: Location of the UGS sites managed by Stogit S.p.A. in Italy. [Source: https://www.snam.it/en/about-us/snam-infrastructures/storage-sites]

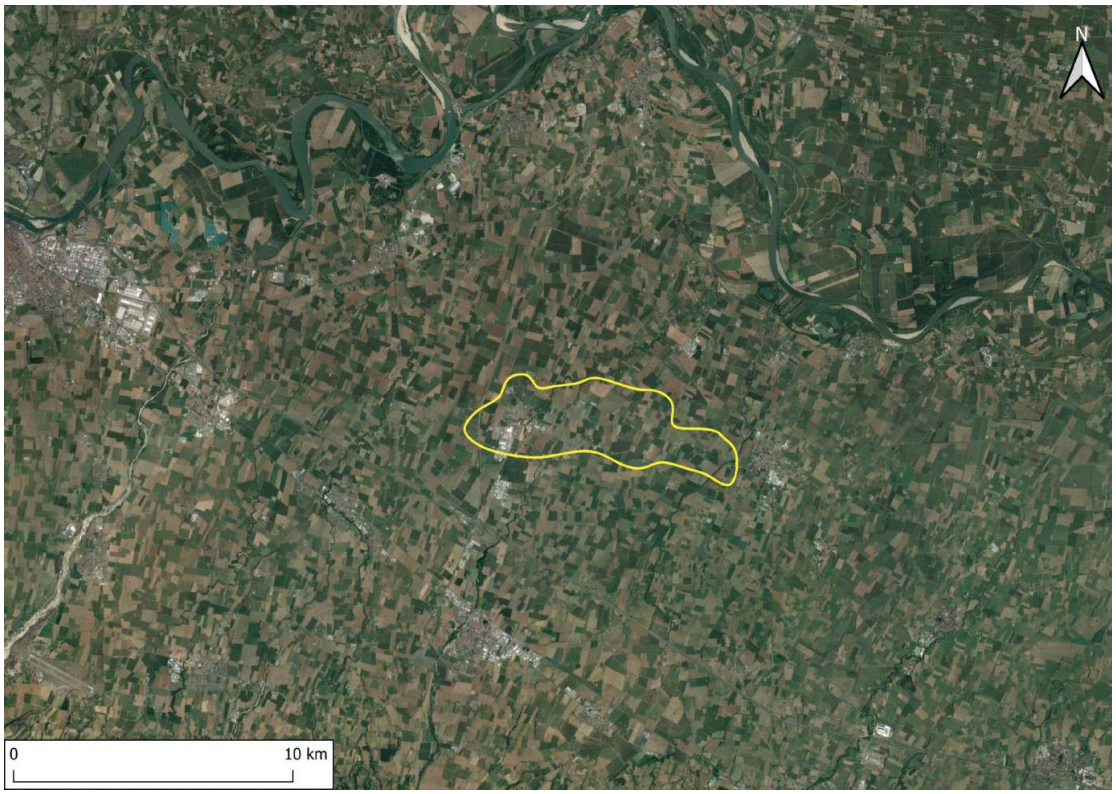

FIGURE 2.2: Satellite image of the study area. The yellow line indicates the trace of the reservoir.

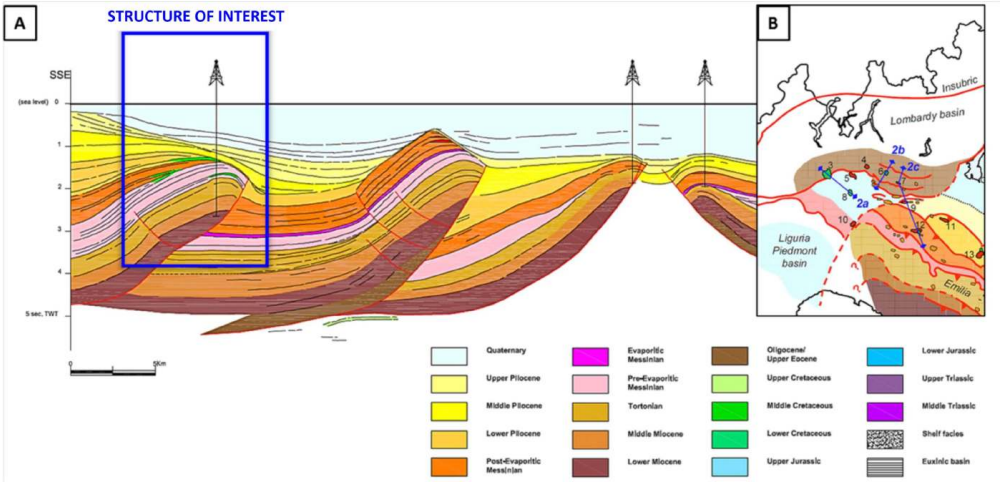

FIGURE 2.3: (A) Interpretation of the geological section of the underground of the Po river Plain. (B) Location of section A (indicated as section 2c). [Source: Stogit S.p.A. Geological study report.]

system of buried folds and overthrusts with northern vergence constituting the Emilia Folds (Figure 2.3).

From the upper Miocene to the Pliocene, Cenozoic deformation events separated the internal sector of the chain, where there is the piggyback basin, and the external sector, corresponding to the principal foredeep basin, located further to the north. A different evolution of the Miocene-Pliocene stratigraphic sequences is therefore present as shown in Figure 2.4. The lower part of the stratigraphic sequence is composed, from the bottom to the top, of:

1. limestone and dolomite rocks;
2. prevailing marls and marls with sandy intercalations;
3. banks of sands with marly intercalations and alternations of sands and marls of Miocene.

In the external sector on the north-east, the next geological formation is of Messinian sands; then, there is the Pliocene succession composed of an alternation of clays and silty clays, Santerno clays, and sands.

In the internal sector on the south-west, delimited on the north by the system of thrusts controlling the reservoir structure, the Messinian formation includes:

1. marls, chalky-clayey marls with intercalations of sands and gypsums;

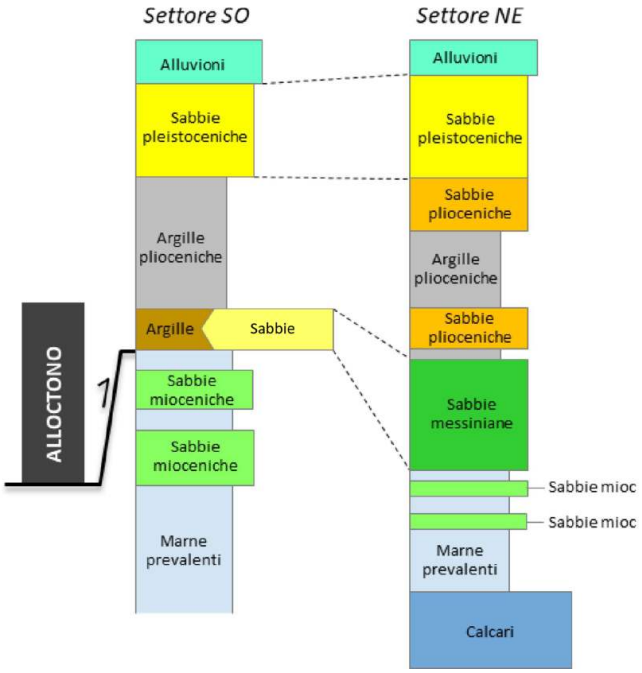

FIGURE 2.4: Schematic representation of the stratigraphy of the site (not in scale). [Source: Stogit S.p.A. Geological study report.]

2. clays and clays to marls with sands intercalations;

3. alternation of more or less silty clays, silt, and sands.

These deposits are covered by Santerno clays. In the southwest sector, an allochthonous sequence composed of scaly clays, clayey marl with calcareous and arenaceous intercalations, and alternation of calcareous marl, marly limestone, and sandstone is present. This sequence is stratigraphically covered by Messinian sands and Santerno clays.

Lastly, the Quaternary succession, covering completely and with continuity the interest area, is represented by the sandy-clayey succession of Pleistocene (i.e., Sands of Asti, Formation of Ravenna + Porto Garibaldi) and by the recent alluvial deposits.

Taking a deeper look into the structure of the reservoir, Pool A is composed of sandy layers and silty-clayey intercalations with a lenticular geometry progressively decreasing thickness towards the east ranging from 100 m to roughly 20 m. A clay formation, in the order of 200-300 m of depth and with a large horizontal extent, belonging to Santerno clays (Pliocene) ensures good hydraulic isolation from the shallower layers.

The material in the area of Pool C is mainly composed of fine to very fine sands, silt, and silty clays. The average thickness at wells is 12 m decreasing towards the

east until a complete closure by pinch-out defines a stratigraphic gap. Based on log data and profiles from wells, a great lithological variability, both areal and vertical, has been identified, preventing a continuity correlation between silty-sandy intervals or clayey layers. So, these clay intercalations, where present, do not create vertical compartmentation inside the reservoir. A continuous range of clays and marly clays with thicknesses ranging from metric to decametric, belonging to the same Messinian sands and separating Pool C from the overlying Pool A, ensures coverage over the entire area of the deposit.

The system of faults at regional scale, which is bounding the reservoir, consists of a series of faults oriented from E-W to NW-SE, in particular there is an overthrust with Apennines vergence to the north and a back-thrust with meridional vergence to the south. The structure of the reservoir is an asymmetrical anticline with an axis extending from E-W to NW-SE. The trap characterizing the reservoir is mainly of structural type and closes by slope in all directions. Pool C presents also a stratigraphic closure by pinch-out toward E-NE. Along the top zone and the southern side of the trap, there is a system of extensional/ transtensive faults which are locally interconnected and caused by tensional release phenomena that occurred after the setting up of the structure. These faults, present only at local scale, have limited throws with the prevalent direction being parallel or sub-parallel to the bending axis of the reservoir and variable orientation from NE-SW to almost E-W. In general, these discontinuities present a high inclination (vertical or sub-vertical faults). The position of the faults considered in the following analysis is shown in Figure 2.5 with a zoom on the reservoir area in Figure 2.6.

2.2 Production and storage

Stogit S.p.A. has provided the dynamic models of the reservoir, developed through the software Eclipse by Schlumberger [2014], used for the management of the site. Two separate models have been created, one for each pool. Based on them and on the technical reports, the behaviour of the pressure field in the reservoir over time has been

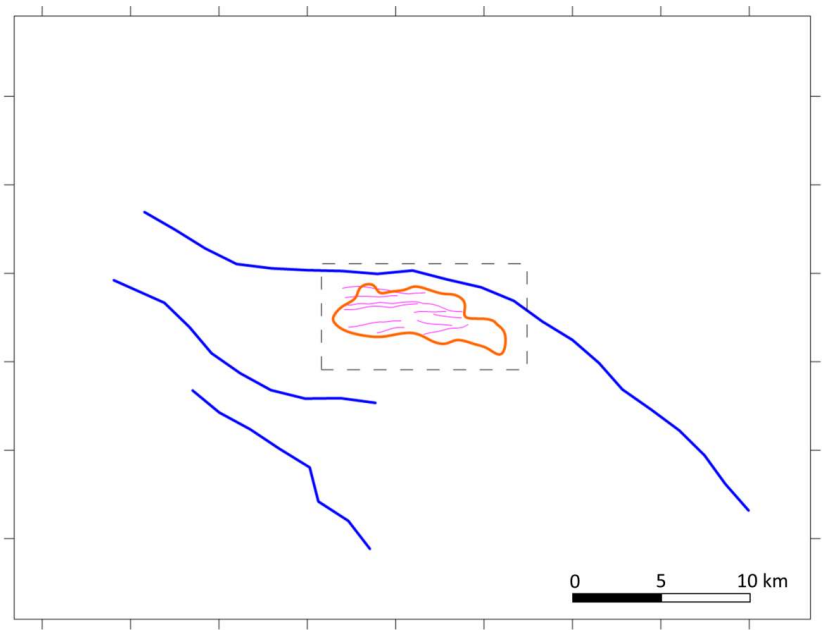

FIGURE 2.5: Position of the regional faults (in blue) and the main local discontinuities (in purple). The boundary of the reservoir is in orange.

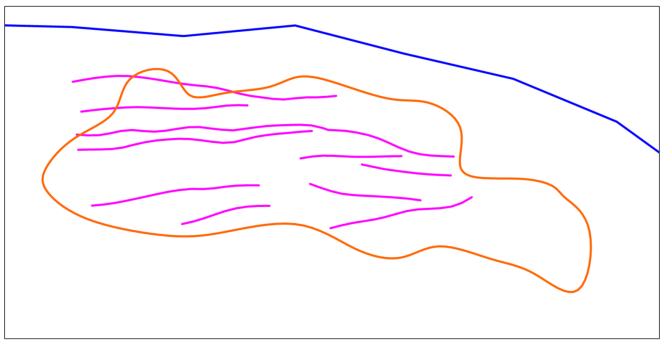

FIGURE 2.6: A zoom in the area of the reservoir, indicated in Figure 2.5 with a dashed line.

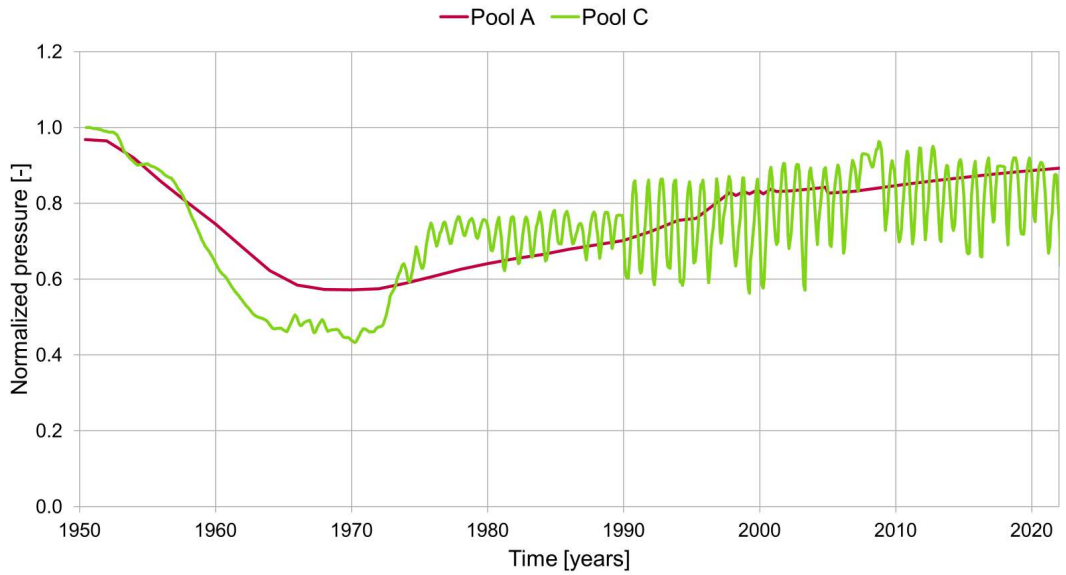

FIGURE 2.7: Behaviour over time of the normalized average pressure in the two pools.

recreated. As the original data are confidential, in this work the pressures are shown normalized to the initial value of pressure in Pool C as represented in Figure 2.7.

Primary production started in 1950 for both pools and mainly ended in 1964 for Pool C and 1971 for Pool A. In 1964 Pool C was converted into a storage field, however some wells continued with the primary production until 1996. Also in Pool A the extraction continued after 1971 for some wells and was definitely concluded in 1991 when the storage conversion has begun. However, the storage in Pool A was temporarily stopped in 2002 due to the low efficiency observed after some annual cycles. The storage phase of Pool C is still ongoing at the present time and it is expected to continue also in the next years.

2.3 Monitoring of displacements on the reservoir area

Stogit S.p.A. has also provided an integrate monitoring report about the displacements occurred on the area where the reservoir is located. The interferometric SAR (Synthetic Aperture Radar) technique was applied to analyse the radar images acquired in ascending and descending geometry by the Radarsat-1, Radarsat-2 and Sentinel-1 satellites. In particular, Radarsat-1 and Radarsat-2 together took 227 and 239 images in

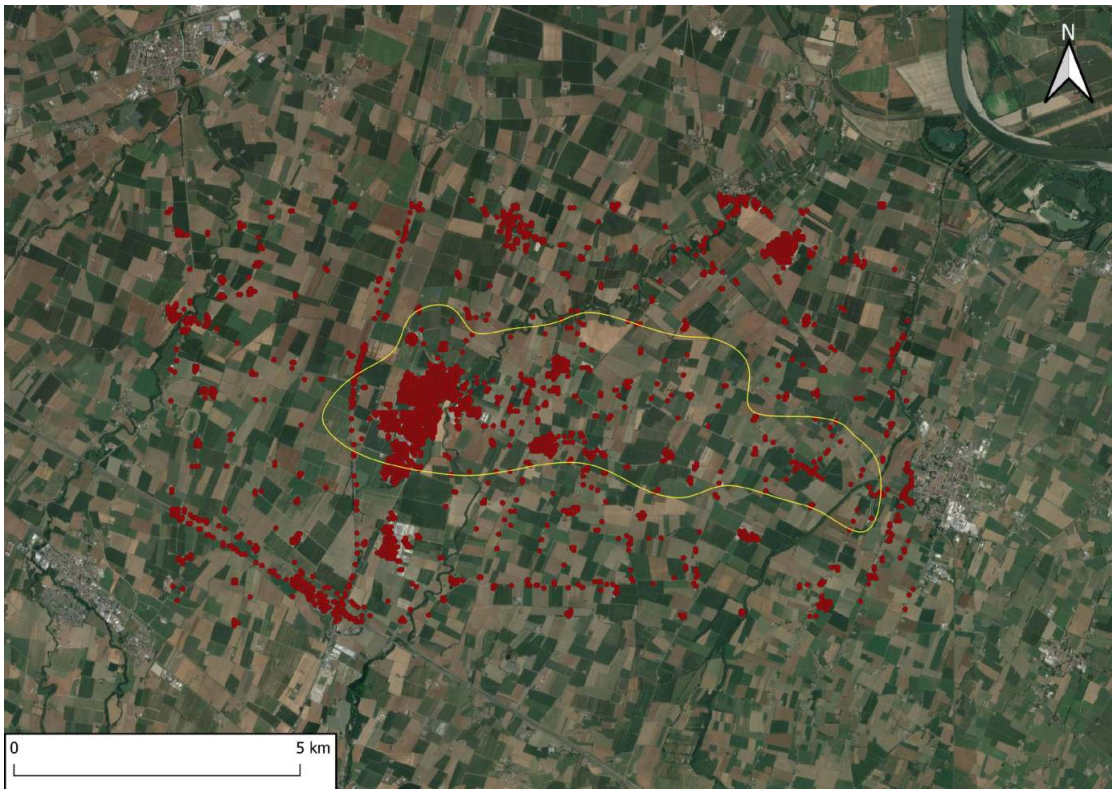

FIGURE 2.8: Position of the detected PS with respect to the area of the reservoir (in yellow).

ascending and descending geometry, respectively, from October 2003 to October 2020 almost every month, while Sentinel-1 took 337 and 350 images from March 2015 to October 2021 almost every week. Hence, combining the two databases it is possible to monitor a longer temporal interval. As the same area can be seen from ascending and descending orbits, the data of the two acquisition geometries can be combined to calculate the vertical and horizontal components of the motion. In the horizontal plane only the components along the West-East direction was considered. The applied technique requires a great number of images acquired on the same area in order to find some elements on the soil called PS (Persistent Scatterers) which present a high stability in the amplitude values and great coherence in phase in all the acquisitions. These points are mainly recognizable on urbanized areas. Figure 2.8 shows the dispositions of the detected PS: unfortunately, the distribution of the points is not homogeneous above the reservoir with a greater concentration on the western part.

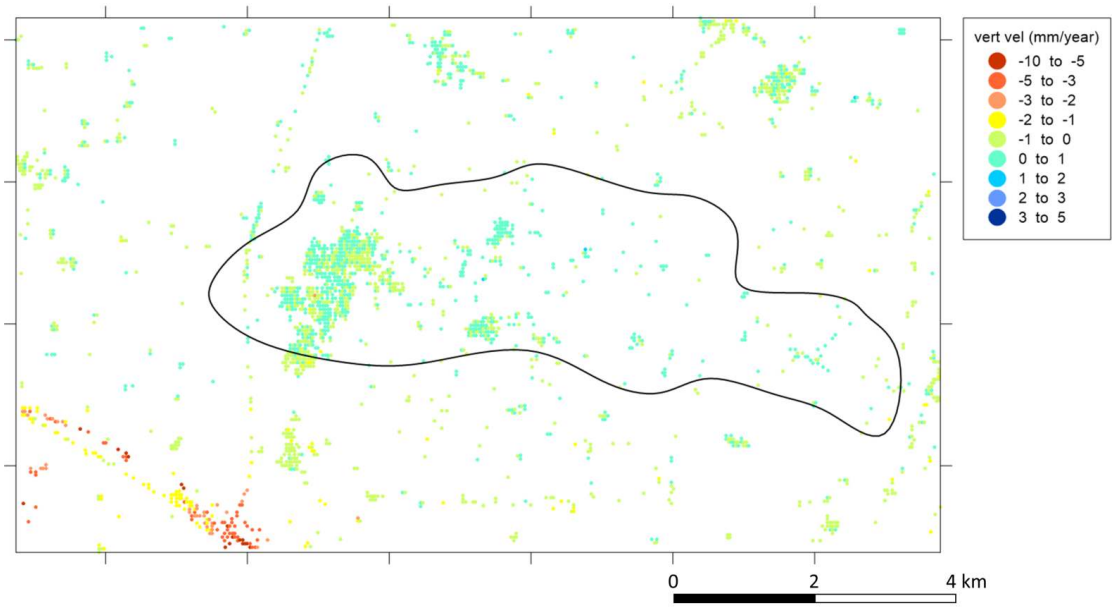

FIGURE 2.9: Average vertical velocity (mm/years) for the period 2003-2021 of the identified PS. The trace of the reservoir is indicated with the black line.

2.3.1 Average velocity of displacement

Firstly, the average velocity over the period of acquisition of the satellites data can be checked. Looking at the vertical component (Figure 2.9), the area is mainly stable with the only exception on the South-West sector near the highway and the High Speed Train line where major movements are recorded. This downward trend began during the years of construction of the High Speed Line (2001-2003) and is essentially linked to the adjustment of the infrastructures. About the points inside the area of the reservoir the average vertical velocity is between -1 and 1 mm/year. Hence, it can be said that the underground gas storage does not affect the stability of the area in a significant way. Moreover, also considering the horizontal component of velocity the area shows a good stability (Figure 2.10).

2.3.2 Displacement variation during storage and supply cycles

Of greater interest, especially for the calibration of the geomechanical model, are the displacements analyzed during a storage cycle (usually from spring to autumn) and during a supply cycle (from autumn to spring). An example of the vertical displacement obtained from the interferometric analysis during these two phases is reported in

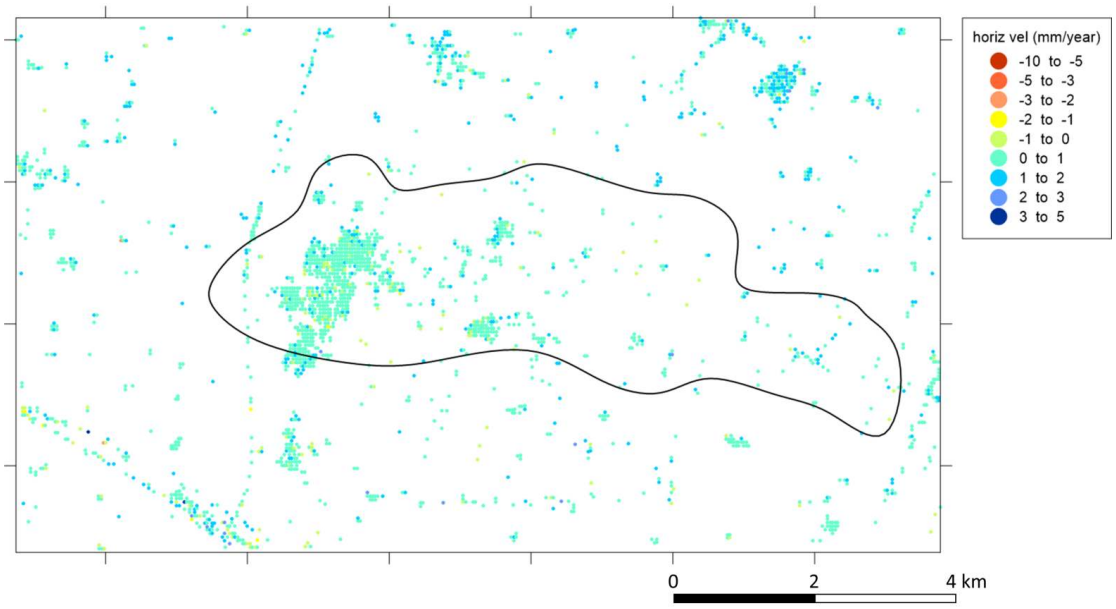

FIGURE 2.10: Average horizontal velocity (mm/years) for the period 2003-2021 of the identified PS. The trace of the reservoir is indicated with the black line.

the following figures: Figure 2.11 for the period from May 2015 to November 2015 and Figure 2.12 from November 2015 to May 2016.

From these images we can say that, as expected, during the storage phase the variation of vertical displacements has positive values (about 3 to 5 mm), especially at the center of the reservoir, indicating an uplift of the soil because of the injection of the gas. The opposite result during the supply cycle is less evident as the vertical displacements are generally limited with variations of just a few millimeters; however, we can still see a few points with greater displacement values (around -5 mm) in the middle of the area.

For the same cycles also the horizontal displacement, in the W-E direction, has been analyzed and the results are shown in Figure 2.13 for the storage cycle and in Figure 2.14 for the supply cycle. Also in this case the movements are in general of about few millimeters but with some exceptions. In fact, during the storage phase the points are supposed to move away from the baricenter of the reservoir, while during the supply phase they should move toward it. This behaviour can be seen in Figure 2.13 where some points show higher negative values (around 5 mm), indicating that they are moving away from the center, and in Figure 2.14 where points have mainly positive values

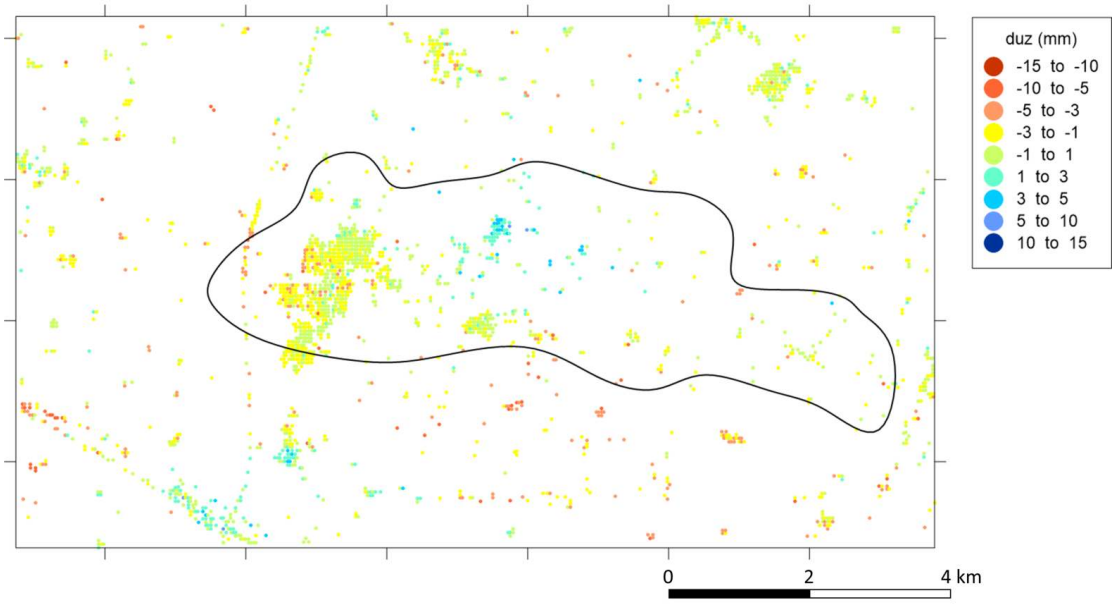

FIGURE 2.11: Vertical displacement obtained from the interferometric analysis during the storage cycle from May 2015 to November 2015. The trace of the reservoir is indicated with the black line.

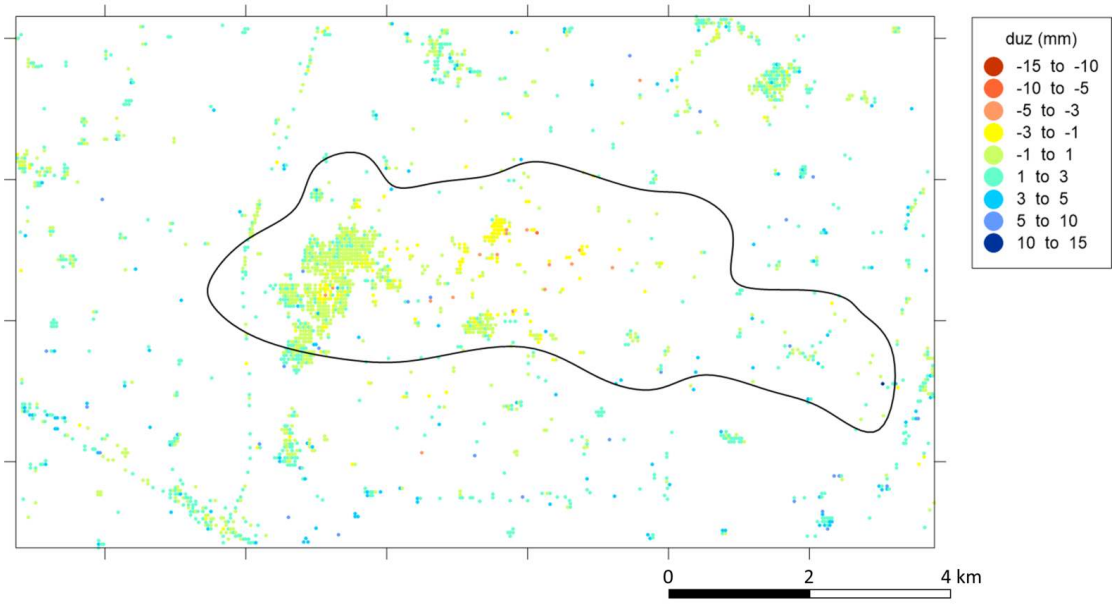

FIGURE 2.12: Vertical displacement obtained from the interferometric analysis during the supply cycle from November 2015 to May 2016. The trace of the reservoir is indicated with the black line.

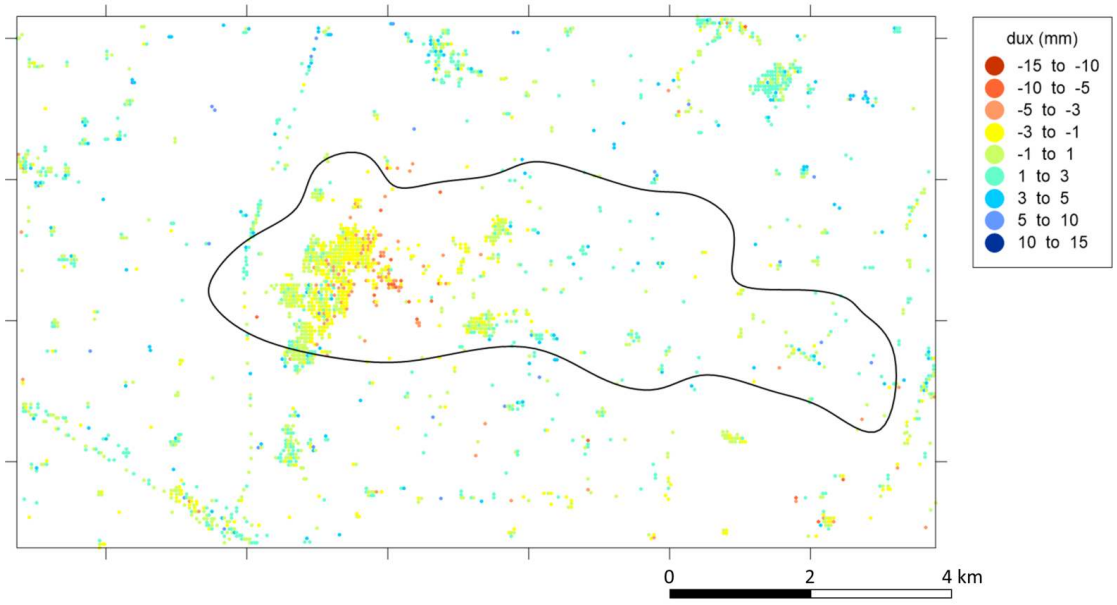

FIGURE 2.13: Horizontal displacement obtained from the interferometric analysis during the storage cycle from May 2015 to November 2015. The trace of the reservoir is indicated with the black line.

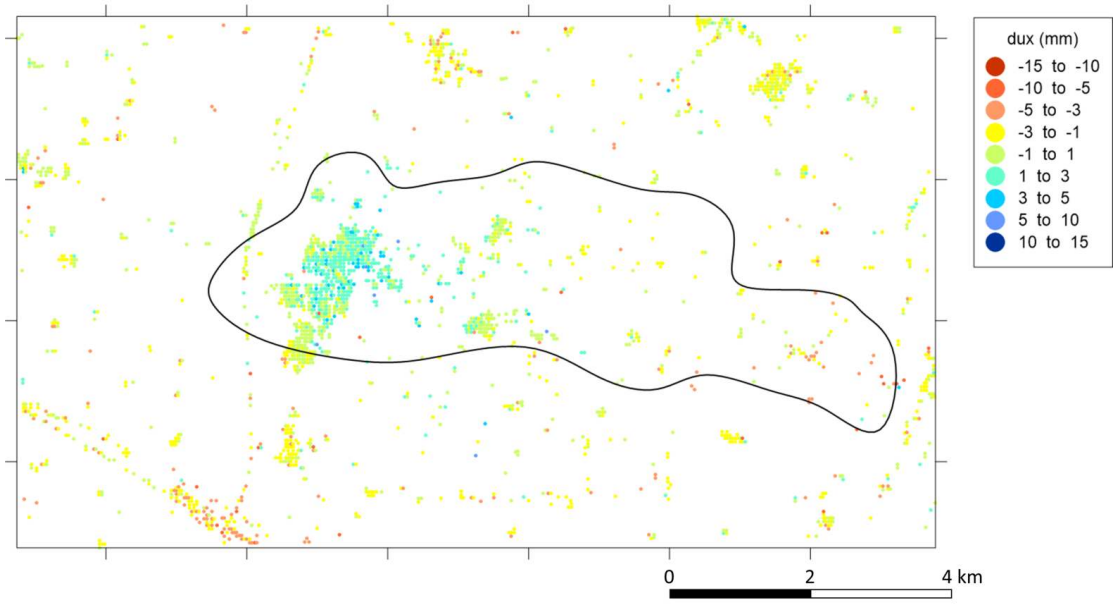

FIGURE 2.14: Horizontal displacement obtained from the interferometric analysis during the supply cycle from November 2015 to May 2016. The trace of the reservoir is indicated with the black line.

as they are moving towards the baricenter.

2.3.3 Vertical displacements over time

In order to understand if there is a correlation between the displacements of the land surface and the storage activity of the underground reservoir, six PTs have been chosen to analyse in details their vertical displacements over time. The location of these points is shown in Figure 2.15: three of them are inside the boundary of the reservoir, while the other three are external points. Their behaviours in time are shown together with the average pressure of Pool A and Pool C from Figure 2.16 to Figure 2.21, starting with the internal points and then the external ones.

The analysis shows a correlation between the vertical displacements and the pressure behaviour over time for the two points situated above the reservoir, near the center where the peak is located. The correlation is evident mainly during the period between 2013 and 2022. Their variations have oscillations between the cycles of about 5 millimeters and a behaviour over time comparable with the one of the pressure. Furthermore, a slight upward trend in the cyclic oscillations can be identified. The other internal point, which is located more to the western side of the reservoir, has almost no correlation between vertical displacements and the pressure behaviour; moreover, in some cases the peaks of maximum and minimum are in contrast between the two plots. About the three external points, no evident correlation can be recognized.

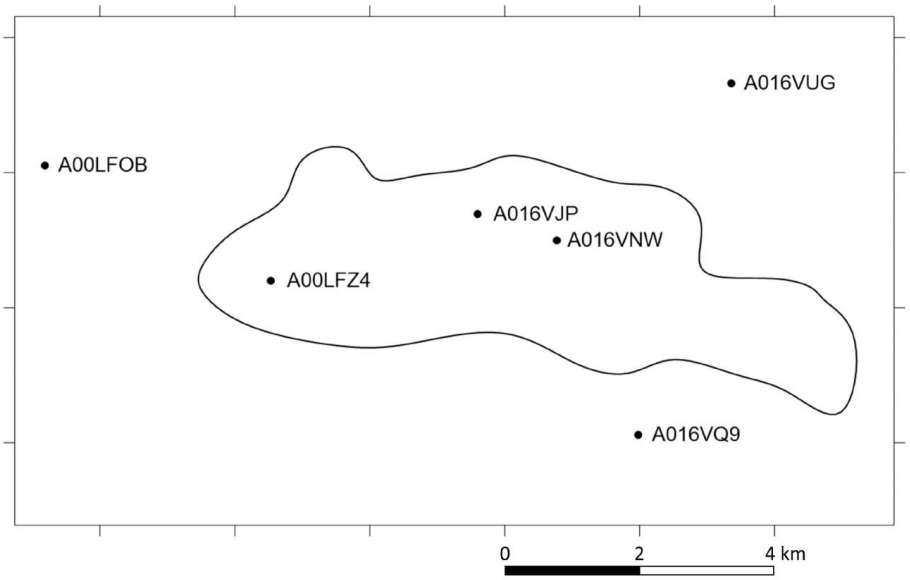

FIGURE 2.15: Position of the selected points for the analysis of the vertical displacements over time. The trace of the reservoir is indicated with the black line.

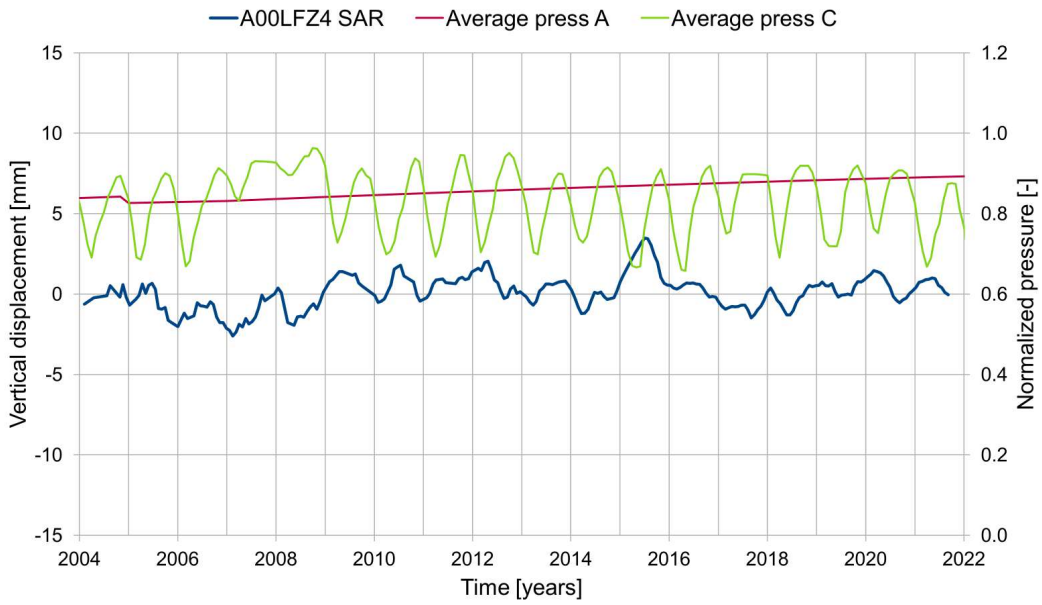

FIGURE 2.16: Vertical displacement over time of the internal point A00LFZ4 and of the average pressure of Pool A and Pool C between 2003 and 2021.

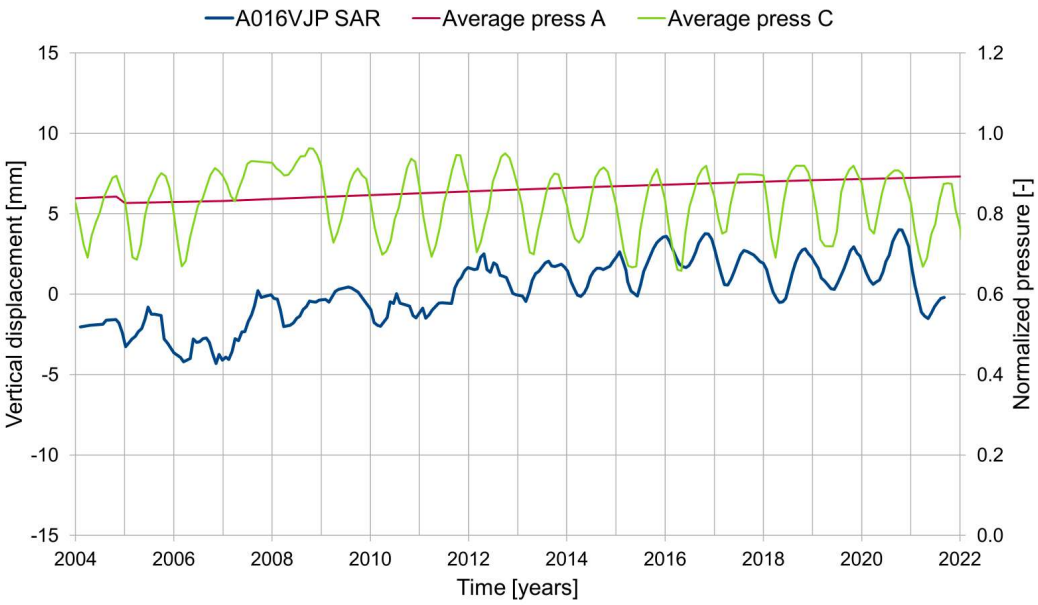

FIGURE 2.17: Vertical displacement over time of the internal point A016VJP and of the average pressure of Pool A and Pool C between 2003 and 2021.

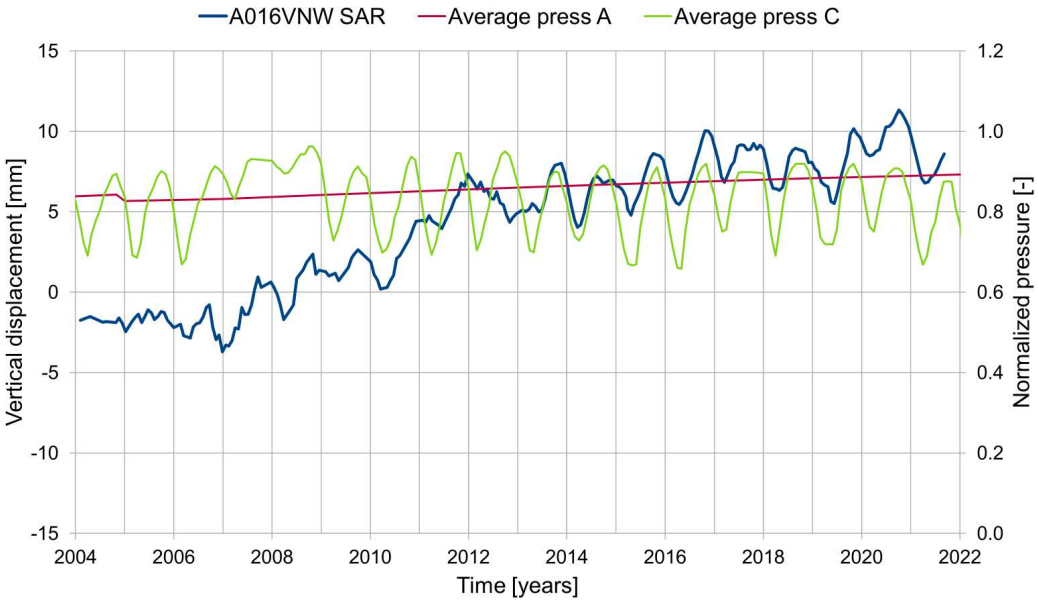

FIGURE 2.18: Vertical displacement over time of the internal point A016VNW and of the average pressure of Pool A and Pool C between 2003 and 2021.

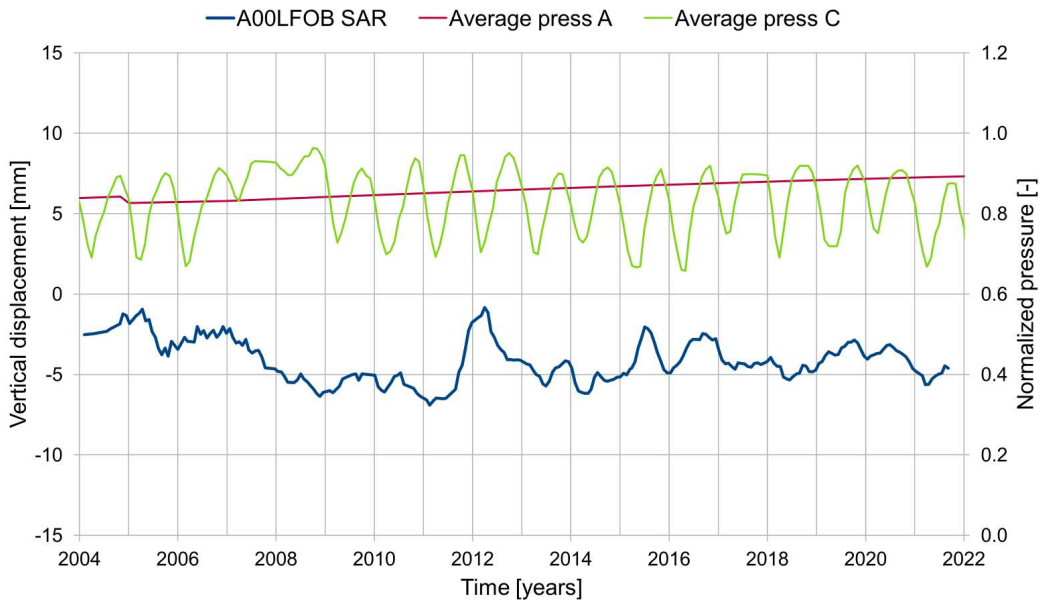

FIGURE 2.19: Vertical displacement over time of the external point A00LFOB and of the average pressure of Pool A and Pool C between 2003 and 2021.

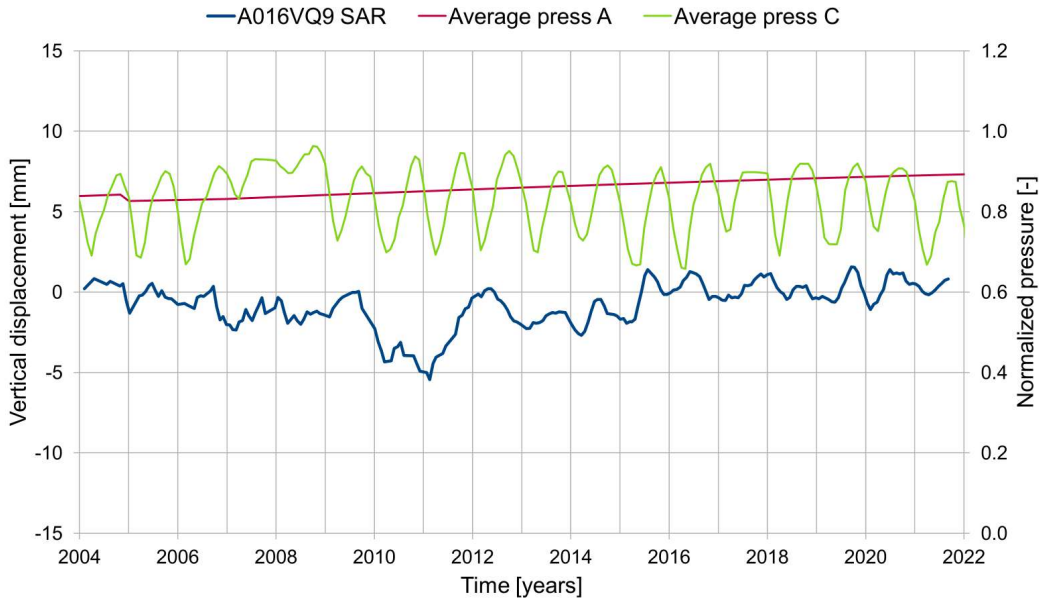

FIGURE 2.20: Vertical displacement over time of the external point A016VQ9 and of the average pressure of Pool A and Pool C between 2003 and 2021.

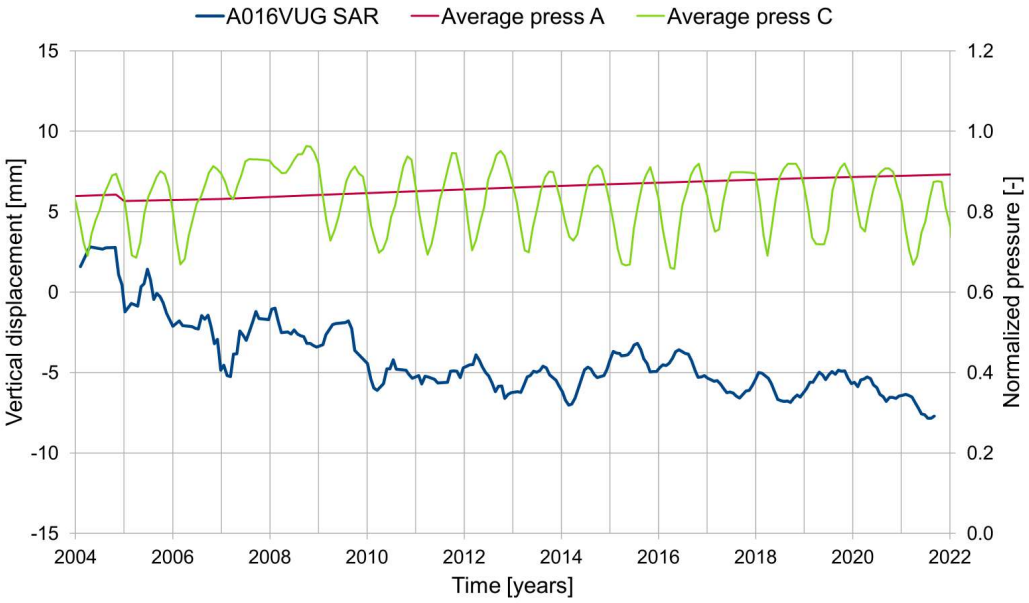

FIGURE 2.21: Vertical displacement over time of the external point A016VUG and of the average pressure of Pool A and Pool C between 2003 and 2021.

Chapter 3

Methodology

3.1 General theory of poro-elasticity

The soil can be assumed as a porous medium where two phases are present: the solid phase and the void space where one or more fluids, either gas or liquid, are flowing.

Poro-elasticity is a field in materials science and mechanics that studies the interaction between fluid flow and solid strain within a linear porous medium and it is an extension of elasticity (linear momentum balance) and porous medium flow (diffusion equation). The strain of the medium influences the flow of the fluid and vice versa. The theory was proposed by Biot [1941].

The final aim of the analysis is to find the changes within the soil volume in terms of displacements, strains and stresses in the entire domain. In a mathematical approach, this is equal to find the components of the displacement vector and of the two tensors of strains and stresses:

$$\boldsymbol{u} = \begin{bmatrix} u \\ v \\ w \end{bmatrix} \qquad \boldsymbol{\epsilon} = \frac{1}{2}(\nabla \boldsymbol{u} + \nabla \boldsymbol{u}^T) = \begin{bmatrix} \epsilon_x & \gamma_{yx} & \gamma_{zx} \\ \gamma_{xy} & \epsilon_y & \gamma_{zy} \\ \gamma_{xz} & \gamma_{yz} & \epsilon_z \end{bmatrix} \qquad \boldsymbol{\sigma} = \begin{bmatrix} \sigma_x & \tau_{yx} & \tau_{zx} \\ \tau_{xy} & \sigma_y & \tau_{zy} \\ \tau_{xz} & \tau_{yz} & \sigma_z \end{bmatrix} \tag{3.1}$$

The conservation of angular momentum, that can be summarized as

$$\tau_{xy} = \tau_{yx} \qquad \tau_{xz} = \tau_{zx} \qquad \tau_{yz} = \tau_{zy} \tag{3.2}$$

is applied to the tensor $\boldsymbol{\sigma}$ which is symmetric and composed of 6 independent terms, hence the tensors can be written as the following vectors:

$$\boldsymbol{\sigma} = [\sigma_x, \sigma_y, \sigma_z, \tau_{yz}, \tau_{xz}, \tau_{xy}]^T \tag{3.3}$$

$$\boldsymbol{\epsilon} = [\epsilon_x, \epsilon_y, \epsilon_z, \gamma_{yz}, \gamma_{xz}, \gamma_{xy}]^T \tag{3.4}$$

Considering a fully saturated soil, any variation of the conditions of the flux field, for instance injection or removal of the fluid, produces a propagation of the perturbation in the fluid itself but also a stress variation and consequently a strain in the solid matrix. Hence, the stresses present in the soil skeleton are acting both on the water, through the hydrostatic pressure in the voids, and on the solid matrix, through the average effective stress. The partition between the two phases is described by Terzaghi's effective stress principle:

$$\hat{\boldsymbol{\sigma}} = \boldsymbol{\sigma} - \alpha p \boldsymbol{i} \tag{3.5}$$

where:

- $\hat{\boldsymbol{\sigma}} = [\hat{\sigma}_x, \hat{\sigma}_y, \hat{\sigma}_z, \hat{\tau}_{xy}, \hat{\tau}_{yz}, \hat{\tau}_{xz}]^T$ is the vectorial form of the tensor of total stresses;
- $\boldsymbol{\sigma} = [\sigma_x, \sigma_y, \sigma_z, \tau_{yz}, \tau_{xz}, \tau_{xy}]^T$ is the vectorial form of the tensor of effective stresses;
- $\alpha = 1 - \frac{C_r}{C_b}$ is Biot's coefficient, where C_r is the volumetric compressibility of grains and C_b is the bulk modulus;
- p is the pore fluid pressure;
- $\boldsymbol{i} = [1, 1, 1, 0, 0, 0]^T$ is the vectorial form of the Kronecker delta.

The usual sign convention is applied: positive and negative stresses indicate tension and compression, respectively, while a positive pressure acts normal to, and in a direction toward, the surface of the body.

A set of equations is needed to fully describe the poro-elasticity theory. It includes the flow equation, for a fluid in a porous medium, and the structural equations, describing the soil equilibrium. The mathematical explanation of these models is presented in the next subsections.

3.1.1 Fluid dynamics in porous media

In order to define the flux of a fluid in a porous medium, the first equation to be considered is Darcy's law:

$$\mathbf{v} = -K_{ij}\nabla\Phi \tag{3.6}$$

where:

- $\mathbf{v}$ is Darcy's velocity vector;
- K_{ij} is the hydraulic conductivity tensor;
- ∇ is the gradient operator $[\frac{\partial}{\partial x}, \frac{\partial}{\partial y}, \frac{\partial}{\partial z}]^T$;
- Φ is the hydraulic potential of the fluid.

K_{ij} and Φ can be expressed as:

$$K_{ij} = k_{ij}\frac{\gamma_w}{\mu}$$

$$\Phi = \int_{z_0}^{z} dz + \int_{p_0}^{p} \frac{dp}{\gamma_w(p)}$$

where:

- k_{ij} is the permeability tensor;
- γ_w is the specific weight of the fluid;
- μ is the viscosity of the fluid;
- p_0 and z_0 are the reference values for pressure and vertical coordinates (positive upwards), respectively.

Darcy's velocity vector, in saturated conditions, is equal to:

$$\mathbf{v} = n(\mathbf{v}_w - \mathbf{v}_s) \tag{3.7}$$

where $\mathbf{v}_w$ and $\mathbf{v}_s$ are the vectors of the absolute velocity of the fluid and of the porous medium, respectively, while n is the porosity.

Considering that the soil is fully saturated, only the solid and the liquid phases are present and so their state equations can be written as:

$$\gamma_s = \text{const} \quad \text{for the solid phase} \tag{3.8}$$

$$\gamma_w = \gamma_{w_0} e^{\beta(p-p_0)} \quad \text{for the liquid phase} \tag{3.9}$$

where:

- γ_s is the specific weight of grains;
- γ_{w_0} is the specific weight of the reference fluid;
- β is the compressibility of the fluid;
- p is the pressure of the fluid;
- p_0 is the initial pressure of the fluid.

The second equation to be considered is the continuity equation referring to an elementary fixed volume for both phases:

$$-\nabla[(1-n)\gamma_s \mathbf{v}_s] = \frac{\partial[(1-n)\gamma_s]}{\partial t} \quad \text{for the solid phase} \tag{3.10}$$

$$-\nabla[n\gamma_w \mathbf{v}_w] = \frac{\partial[n\gamma_w]}{\partial t} \quad \text{for the liquid phase} \tag{3.11}$$

Taking into account the continuity equations, assuming that $\mathbf{v}_s \simeq 0$, using Darcy's equation to express the pore fluid velocity and considering the state equation for the fluid, the final equation of the flow model is:

$$\nabla \left[K_{ij} \left(\frac{\nabla p}{\gamma_w} + \nabla z \right) \right] = n\beta \frac{\partial p}{\partial t} + \frac{\partial \epsilon}{\partial t} \tag{3.12}$$

where ϵ is the volumetric strain of the porous medium:

$$\nabla \boldsymbol{u} = \frac{\partial u}{\partial x} + \frac{\partial v}{\partial y} + \frac{\partial w}{\partial z} = \epsilon_x + \epsilon_y + \epsilon_z = \epsilon$$

The unknowns in the flow equation (3.12) are p and ϵ, so it is not possible to determine the pressure field of the fluid in a non-stationary regime at the moment. Another

equation is needed to solve the problem and it is the one describing the elastic equilibrium of the solid matrix.

3.1.2 Elastic equilibrium of the porous medium

Poro-elasticity theory uses a mathematical approach to describe the soil behavior, but it needs some assumptions in order to provide a simplified but appropriate solution. The hypothesis are:

- the soil has a linear elastic behaviour, so it can be described through Hooke's law;
- only small displacements and small strains can happen;
- the main strain is in the porous matrix and the single grains are considered incompressible;
- Terzaghi's principle holds, so the deformation of the porous matrix depends only on the variations of the effective intergranular stress.

Considering a cubic elementary volume of porous medium (Figure 3.1), oriented with the lateral faces parallel to the direction of the main axes, the stress tensor components can be described with Terzaghi's principle (3.5):

$$\begin{aligned} \hat{\sigma}_x &= \sigma_x - \alpha p & \hat{\tau}_{yz} &= \tau_{yz} & \hat{\tau}_{zy} &= \tau_{zy} \\ \hat{\sigma}_y &= \sigma_y - \alpha p & \hat{\tau}_{zx} &= \tau_{zx} & \hat{\tau}_{xz} &= \tau_{xz} \\ \hat{\sigma}_z &= \sigma_z - \alpha p & \hat{\tau}_{xy} &= \tau_{xy} & \hat{\tau}_{yx} &= \tau_{yx} \end{aligned} \tag{3.13}$$

where:

- σ are the normal stresses, with the index indicating the direction along which they develop;
- τ are the shear stresses, with the first index indicating the direction normal to the plane containing them and the second one indicating the direction along which they develop.

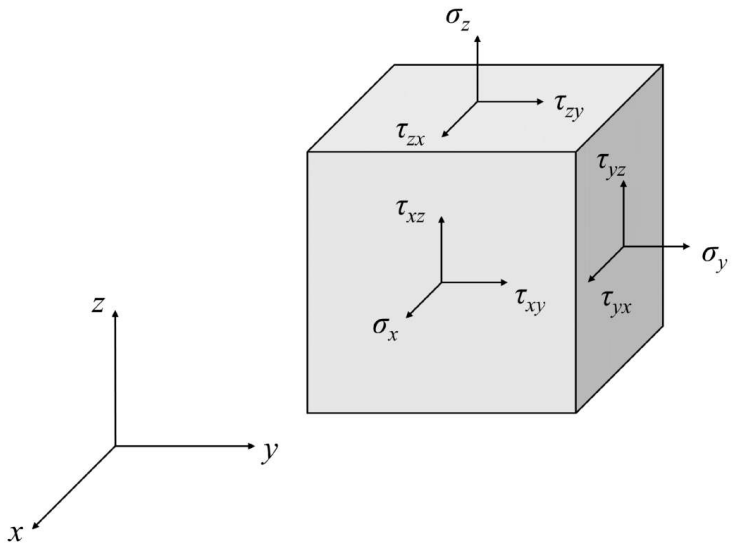

FIGURE 3.1: Cubic elementary volume with indications of the stress components.

The stresses in the soil must be in equilibrium with the volume forces. This relation can be expressed by Cauchy's equations:

$$\begin{aligned}
\frac{\partial \hat{\sigma}_x}{\partial x} + \frac{\partial \hat{\tau}_{yx}}{\partial y} + \frac{\partial \hat{\tau}_{zx}}{\partial z} + F_x = 0 \\
\frac{\partial \hat{\tau}_{xy}}{\partial x} + \frac{\partial \hat{\sigma}_y}{\partial y} + \frac{\partial \hat{\tau}_{zy}}{\partial z} + F_y = 0 \\
\frac{\partial \hat{\tau}_{xz}}{\partial x} + \frac{\partial \hat{\tau}_{yz}}{\partial y} + \frac{\partial \hat{\sigma}_z}{\partial z} + F_z = 0
\end{aligned} \tag{3.14}$$

where F_x, F_y and F_z are the three components of the strength per unit volume.

Supposing that the initial stress tensor is in equilibrium, each variable represents the increment of stress starting from the initial undisturbed state. Furthermore, substituting equations (3.13) into equations (3.14) a new system, expressed in terms of effective stresses and pressures, is obtained:

$$\begin{aligned}
\frac{\partial \sigma_x}{\partial x} + \frac{\partial \tau_{yx}}{\partial y} + \frac{\partial \tau_{zx}}{\partial z} = \alpha \frac{\partial p}{\partial x} \\
\frac{\partial \tau_{xy}}{\partial x} + \frac{\partial \sigma_y}{\partial y} + \frac{\partial \tau_{zy}}{\partial z} = \alpha \frac{\partial p}{\partial y} \\
\frac{\partial \tau_{xz}}{\partial x} + \frac{\partial \tau_{yz}}{\partial y} + \frac{\partial \sigma_z}{\partial z} = \alpha \frac{\partial p}{\partial z}
\end{aligned} \tag{3.15}$$

However, the unknowns of the flow model are expressed in terms of displacements, not of stresses. The relation between stress and strain is stated through Hooke's law which, for isotropic soil, reads:

$$\begin{aligned} \epsilon_x &= \frac{1}{E}[\sigma_x - \nu(\sigma_y + \sigma_z)] & \gamma_{yz} &= \frac{\tau_{yz}}{2G} \\ \epsilon_y &= \frac{1}{E}[\sigma_y - \nu(\sigma_z + \sigma_x)] & \gamma_{xz} &= \frac{\tau_{xz}}{2G} \\ \epsilon_z &= \frac{1}{E}[\sigma_z - \nu(\sigma_x + \sigma_y)] & \gamma_{xy} &= \frac{\tau_{xy}}{2G} \end{aligned} \tag{3.16}$$

where:

- ϵ_i and γ_{ij} are the strain vector components presented in equation (3.4) of the normal and shear stresses, respectively;
- E is Young's modulus;
- ν is Poisson's ratio;
- G is the shear modulus.

Therefore, under the hypothesis of small displacements, the strain vector can be expressed as:

$$\begin{bmatrix} \epsilon_x \\ \epsilon_y \\ \epsilon_z \\ \gamma_{yz} \\ \gamma_{xz} \\ \gamma_{xy} \end{bmatrix} = \begin{bmatrix} \frac{\partial}{\partial x} & 0 & 0 \\ 0 & \frac{\partial}{\partial y} & 0 \\ 0 & 0 & \frac{\partial}{\partial z} \\ 0 & \frac{\partial}{\partial z} & \frac{\partial}{\partial y} \\ \frac{\partial}{\partial z} & 0 & \frac{\partial}{\partial x} \\ \frac{\partial}{\partial y} & \frac{\partial}{\partial x} & 0 \end{bmatrix} \begin{bmatrix} u \\ v \\ w \end{bmatrix} \tag{3.17}$$

The shear modulus G is related to E and ν through the formula:

$$G = \frac{E}{2(1+\nu)}$$

The stress components can be explicitly obtained from equations (3.16) and then,

considering the hypothesis of small displacements and small strains, the elastic equilibrium equations expressed in terms of the displacements u, v and w are:

$$\begin{aligned} G\nabla^2 u + (\lambda + G)\frac{\partial \epsilon}{\partial x} &= \frac{\partial p}{\partial x} \\ G\nabla^2 v + (\lambda + G)\frac{\partial \epsilon}{\partial y} &= \frac{\partial p}{\partial y} \\ G\nabla^2 w + (\lambda + G)\frac{\partial \epsilon}{\partial z} &= \frac{\partial p}{\partial z} \end{aligned} \tag{3.18}$$

where λ is the Lamé constant which is equal to

$$\lambda = \frac{\nu E}{(1-2\nu)(1+\nu)}$$

and ∇^2 is the Laplace operator $\frac{\partial^2}{\partial x^2} + \frac{\partial^2}{\partial y^2} + \frac{\partial^2}{\partial z^2}$.

The equations (3.18) together with equation (3.12) represent a system of four equations in four unknowns (u, v, w and p) able to provide the pressure field and the displacements inside the porous medium at each time step.

In the geomechanical analysis of reservoirs, a common assumption is that the stress-strain relation is isotropic, as underlined by Teatini et al. [2011], and so can be written in a compact form as:

$$\boldsymbol{\sigma} = D\boldsymbol{\epsilon} \tag{3.19}$$

where D is the constitutive matrix for an isotropic elastic medium relating the tensor of effective stress $\boldsymbol{\sigma}$ and the strain tensor $\boldsymbol{\epsilon}$ and is equal to:

$$D = \frac{E(1-\nu)}{(1+\nu)(1-2\nu)} \begin{bmatrix} 1 & \frac{\nu}{1-\nu} & \frac{\nu}{1-\nu} & 0 & 0 & 0 \\ \frac{\nu}{1-\nu} & 1 & \frac{\nu}{1-\nu} & 0 & 0 & 0 \\ \frac{\nu}{1-\nu} & \frac{\nu}{1-\nu} & 1 & 0 & 0 & 0 \\ 0 & 0 & 0 & \frac{1-2\nu}{2(1-\nu)} & 0 & 0 \\ 0 & 0 & 0 & 0 & \frac{1-2\nu}{2(1-\nu)} & 0 \\ 0 & 0 & 0 & 0 & 0 & \frac{1-2\nu}{2(1-\nu)} \end{bmatrix} \tag{3.20}$$

The parameters E, G, λ and ν are related to the vertical uniaxial compressibility c_M through the relations:

$$c_M = \frac{(1+\nu)(1-2\nu)}{E(1-\nu)} = \frac{\nu}{\lambda(1-\nu)} = \frac{(1-2\nu)}{2G(1-\nu)} \tag{3.21}$$

Mechanically isotropic soil can be generalized through the hypothesis of transversal isotropy, where the elastic properties of the medium are subdivided into those on the horizontal plane (subindex h) and those on the vertical direction (subindex z). Hence, the constitutive elastic matrix D will become:

$$D = \begin{bmatrix} \frac{1}{E_h} & -\frac{\nu_h}{E_h} & -\frac{\nu_z}{E_z} & 0 & 0 & 0 \\ -\frac{\nu_h}{E_h} & \frac{1}{E_h} & -\frac{\nu_z}{E_z} & 0 & 0 & 0 \\ -\frac{\nu_z}{E_z} & -\frac{\nu_z}{E_z} & \frac{1}{E_z} & 0 & 0 & 0 \\ 0 & 0 & 0 & \frac{2(1+\nu_h)}{E_h} & 0 & 0 \\ 0 & 0 & 0 & 0 & \frac{1}{G_z} & 0 \\ 0 & 0 & 0 & 0 & 0 & \frac{1}{G_z} \end{bmatrix}^{-1} \tag{3.22}$$

where E_h and E_z and ν_h and ν_z are the Young and the Poisson moduli in horizontal and vertical direction, respectively, and G_z is the vertical shear modulus. The shear modulus G_h depends on E_h and ν_h based on the relation $G_h = E_h/[2(1+\nu_h)]$. Hence, as Gambolati et al. [1984] proposed, equation (3.21) can be written in a more general way as:

$$c_M = \frac{1}{E_z}\left(1 - \frac{2\nu_z^2}{1-\nu_h}\frac{E_h}{E_z}\right) \tag{3.23}$$

Equation (3.21) holds when $E_z = E_h = E$ and $\nu_z = \nu_h = \nu$. Referring to land displacements, Gambolati et al. [1984] reported that they are more related to E_z than to E_h, while the Poisson ratios have lower influence as their variability range is not so large (between 0 and 0.5).

3.2 Fault mechanics

A geological fault can be generally described as an internal discontinuity in a continuous porous medium, constituted of two frictional surfaces in contact one to the other.

When the stress states violate a failure criterion, usually the Mohr-Coulomb law, relative displacements between corresponding points are possible. In this situation compenetration is not allowed [Franceschini et al., 2016].

For any point $\mathbf{x}$ along the fault, the acting strength can be subdivided into its two components, σ_n and τ_s, which are acting in the normal and tangential direction, respectively, to the surface. Hence, the Mohr-Coulomb failure criterion can be written as:

$$\tau_s \leq \tau_L = c - \sigma_n \tan \varphi \tag{3.24}$$

where φ and c are the friction angle and the cohesion, respectively, and τ_L is the limit shear strength. Negative normal stress is conventionally assumed as compression, hence, a positive value is not admissible since faults cannot resist to tensile strength. About the angle φ, laboratory studies are normally conducted to obtain a non-linear relation linking it with the fault slippage; however, if tests are not available, a constant φ is commonly assumed.

The Mohr-Coulomb criterion is a scalar relation that does not give any information about the direction where the limiting shear vector τ_L occurs. To overcome this problem the "Principle of Maximum Plastic Dissipation" is applied, as explained by Franceschini et al. [2016].

Let us consider the set $\boldsymbol{T} \subset \mathbb{R}^3$ composed of vectors $\boldsymbol{\tau}(\mathbf{x})$ belonging to the fault plane, such that $\|\boldsymbol{\tau}(\mathbf{x})\|_2 = \tau_L$. When a relative displacement $\boldsymbol{u}_r$ develops between the two fault surfaces, the shear vector $\tau_L \in \boldsymbol{T}$ acting at the point $\mathbf{x}$ is the one maximizing the work W_f of the friction strength, such that:

$$W_f(\mathbf{x}) = \boldsymbol{\tau}(\mathbf{x})^T \boldsymbol{u}_r \qquad \forall \boldsymbol{\tau}(\mathbf{x}) \in \boldsymbol{T} \tag{3.25}$$

the vector $\boldsymbol{\tau}_L$ must have the same direction as $\boldsymbol{u}_r$:

$$\boldsymbol{\tau}_L = \tau_L \frac{\boldsymbol{u}_r}{\|\boldsymbol{u}_r\|_2} \tag{3.26}$$

The system composed of the equations (3.25) and (3.26) allows to uniquely define the fault strength at any point $\mathbf{x}$ of the contact surface.

3.3 Variational formulation

The main problem of finding the displacements $\boldsymbol{u}(\mathbf{x})$ which are in equilibrium with a given set of external forces can be solved using the virtual work principle. The introduction of the Lagrange multipliers $\boldsymbol{\lambda}$ helps to find the solution in case of faults. From a physical point of view, the Lagrange multipliers are the strengths acting on the interface between the fault surfaces [Franceschini et al., 2016]. In particular, let us call $\boldsymbol{\lambda}_n(\mathbf{x})$ and $\boldsymbol{\lambda}_s(\mathbf{x})$ the vectors of the normal and tangential components of the contact strengths, respectively.

In practice, two scenarios are possible:

- The Mohr-Coulomb criterion (3.24) is satisfied: then, the multipliers will ensure the continuity of the displacement $\boldsymbol{u}(\mathbf{x})$.
- The Mohr-Coulomb criterion is violated, because either $\tau_s = \tau_L$ or $\sigma_n = 0$: then, the fault strengths are known while the surfaces are free to move.

Let us take into consideration a 3D body Ω having an external boundary $\partial\Omega$ and subject to a set of body forces $\boldsymbol{b}$ and surface traction $\boldsymbol{t}$. A fault Γ is present inside the domain Ω and it consists of two surfaces Γ_T and Γ_B, top and bottom, respectively. Let us assume that the criterion (3.24) does not hold on a portion of the fault $\bar{\Gamma} \subset \Gamma$. Hence, the relative displacement between contact surfaces can occur and it is conventionally defined as:

$$\boldsymbol{u}_r = \boldsymbol{u}_B - \boldsymbol{u}_T \tag{3.27}$$

being $\boldsymbol{u}_B$ the displacement of the point belonging to the bottom surface and and $\boldsymbol{u}_T$ the corresponding one on the top surface.

The usual form of the virtual work principle is:

$$\delta W_i - \delta W_e = 0 \tag{3.28}$$

but considering also the work contribution from the fault it becomes:

$$\delta W_i + \delta W_f - \delta W_e = 0 \tag{3.29}$$

where δW_i, δW_f and δW_e are the internal, fault and external virtual works, respectively. Let us analyze each term one by one.

The internal virtual work can be written as:

$$\delta W_i = \int_\Omega \delta \boldsymbol{\epsilon}^T \hat{\boldsymbol{\sigma}} \, dV \tag{3.30}$$

where $\boldsymbol{\epsilon}$ is the strain vector presented in equation (3.4) and $\hat{\boldsymbol{\sigma}}$ is the total stress vector reported in equation (3.3). Considering Terzaghi's principle for porous media (3.5) and substituting it in equation (3.30) the result is:

$$\delta W_i = \int_\Omega \delta \boldsymbol{\epsilon}^T \boldsymbol{\sigma} \, dV - \int_\Omega \delta \boldsymbol{\epsilon}^T \boldsymbol{i} \alpha p \, dV \tag{3.31}$$

The fault virtual work is composed of two parts: the first is connected to the portion of the fault Γ where the continuity is preserved and the second one represent the fault portion $\bar{\Gamma}$ where slidings and openings are present. The relation is written as:

$$\delta W_f = \int_{\Gamma \setminus \bar{\Gamma}} \delta \boldsymbol{u}_r^T \boldsymbol{\lambda} \, dS + \int_{\Gamma \setminus \bar{\Gamma}} \delta \boldsymbol{\lambda}^T \boldsymbol{u}_r \, dS + \int_{\bar{\Gamma}} \delta \boldsymbol{u}_r^T \boldsymbol{\tau}_L \, dS \tag{3.32}$$

It has to be noted that in case of opening, the open part of the fault $\bar{\Gamma}$ is not contributing to the virtual work as the normal and shear strength are null ($\boldsymbol{\lambda}_n = \boldsymbol{\lambda}_s = 0$), while if there is sliding, only the shear strength $\boldsymbol{\lambda}_s$ provides a non-zero contribution.

The external virtual work takes into account the body force $\boldsymbol{b}$ and the surface traction $\boldsymbol{t}$ and can be written as:

$$\delta W_e = \int_\Omega \delta \boldsymbol{u}^T \boldsymbol{b} \, dV + \int_{\partial\Omega} \delta \boldsymbol{u}^T \boldsymbol{t} \, dS \tag{3.33}$$

The final expression of the virtual work principle is then:

$$\begin{aligned} \int_\Omega \delta \boldsymbol{\epsilon}^T \boldsymbol{\sigma} \, dV + \int_{\Gamma \setminus \bar{\Gamma}} \delta \boldsymbol{u}_r^T \boldsymbol{\lambda} \, dS + \int_{\Gamma \setminus \bar{\Gamma}} \delta \boldsymbol{\lambda}^T \boldsymbol{u}_r \, dS + \int_{\bar{\Gamma}} \delta \boldsymbol{u}_r^T \boldsymbol{\tau}_L \, dS = \\ = \int_\Omega \delta \boldsymbol{\epsilon}^T \boldsymbol{i} \alpha p \, dV + \int_\Omega \delta \boldsymbol{u}^T \boldsymbol{b} \, dV + \int_{\partial\Omega} \delta \boldsymbol{u}^T \boldsymbol{t} \, dS \end{aligned} \tag{3.34}$$

3.4 One-way coupled model

When simulating the effects caused by the injection and removal of fluids from underground fields, the numerical problems to account for are the flux movement and the geomechanical response, as it was previously explained. Based on the work of Biot [1941], who was the first to describe the relation between these two processes, the coupled approach is usually applied for simulations. This method consists in the solution of the two models together as the equations are connected by the same unknowns. However, Gambolati et al. [2000] and Settari et al. [2008] have demonstrated that for simulations in reservoirs located in the Po river plain, the one-way coupled (also known as uncoupled) approach between the flow model and the geomechanical solution produces equally accurate results. Moreover, these solutions appear to be fully warranted at any timescale of practical interest.

In this thesis, the uncoupled method is applied following these steps:

1. the pressure field is computed through the flow model and extended from the reservoir domain to the confining aquifer. The model will solve the continuity equation
$$\frac{\partial}{\partial x}\left(K_x\frac{\partial p}{\partial x}\right)+\frac{\partial}{\partial y}\left(K_y\frac{\partial p}{\partial y}\right)+\frac{\partial}{\partial z}\left(K_z\frac{\partial p}{\partial z}\right)=S_s\frac{\partial p}{\partial t} \tag{3.35}$$
where $S_s=\gamma_w(n\beta+c_M)$ is the specific elastic storage;

2. the flow model output is used as input for the geomechanical model;

3. the displacement field (including the physically measurable quantities of land subsidence and horizontal displacement) is computed through the geomechanical model which solves this system of equations:
$$\begin{cases}\nabla\boldsymbol{\sigma}+\boldsymbol{f}=0\\ d\boldsymbol{\sigma}=Dd\boldsymbol{\epsilon}\\ \boldsymbol{\epsilon}=L\boldsymbol{u}\end{cases} \tag{3.36}$$

3.5 Numerical modeling

3.5.1 The Finite Element method

In order to solve the partial differential equations described in the previous sections, it is necessary to adopt the Finite Element (FE) method which belongs to the wider category of the variational methods. Unlike the finite difference methods where the differential operator is approximated, with this approach the solution of the equations is directly approximated using a combination of local basis functions. The discretization of the equations in the space domain is achieved by subdividing it into smaller and simpler parts called, indeed, finite elements. Hence, inside the domain N points namely nodes are identified, corresponding to the vertices of the elements.

As explained in Franceschini [2014], in this way we are able to move from the original unknowns, which are functions, to the model unknowns, which are the nodal values, as the interpolation functions are a priori known. Thus, the problem can be expressed as a non linear system of equations in the form of $\mathbf{K}(\mathbf{u})\ \mathbf{u} = \mathbf{f}$, where $\mathbf{K}(\mathbf{u})$ is the discretized version of the differential operator, $\mathbf{u}$ is the vector of unknowns (i.e. nodal displacements) and $\mathbf{f}$ is the vector of external forces.

In this thesis, the chosen finite elements are tetrahedra with linear base functions. Hence, as explained by Gambolati and Ferronato [2015], for a generic element e delimited by the four nodes i, j, k and m (Figure 3.2), the shape function ξ_i^e associated to the node i is

$$\xi_i^e = \frac{a_i + b_i x + c_i y + d_i z}{6V^e} \tag{3.37}$$

where V^e is the element volume taken with its sign and it is

$$V^e = \frac{1}{6} \det \begin{bmatrix} 1 & x_i & y_i & z_i \\ 1 & x_j & y_j & z_j \\ 1 & x_k & y_k & z_k \\ 1 & x_m & y_m & z_m \end{bmatrix}$$

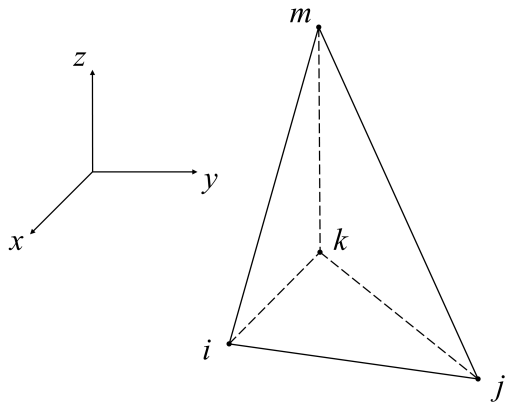

FIGURE 3.2: Tetrahedric finite element.

and the other coefficients are:

$$a_i = \det \begin{bmatrix} x_j & y_j & z_j \\ x_k & y_k & z_k \\ x_m & y_m & z_m \end{bmatrix} \qquad b_i = -\det \begin{bmatrix} 1 & y_j & z_j \\ 1 & y_k & z_k \\ 1 & y_m & z_m \end{bmatrix}$$

$$c_i = \det \begin{bmatrix} 1 & x_j & z_j \\ 1 & x_k & z_k \\ 1 & x_m & z_m \end{bmatrix} \qquad d_i = -\det \begin{bmatrix} 1 & x_j & y_j \\ 1 & x_k & y_k \\ 1 & x_m & y_m \end{bmatrix}$$

The solution to the problem can be therefore expressed using the displacements as unknowns, which have three components for each node. The displacement of a generic point inside the element can be written in a vectorial form as

$$\boldsymbol{u} = \begin{bmatrix} \boldsymbol{N}_1 & \boldsymbol{N}_2 & \boldsymbol{N}_3 & \boldsymbol{N}_4 \end{bmatrix} \begin{bmatrix} \mathbf{u}_1 \\ \mathbf{u}_2 \\ \mathbf{u}_3 \\ \mathbf{u}_4 \end{bmatrix} \tag{3.38}$$

where $\boldsymbol{N}_i$ are the matrices equal to the shape function multiplied by the identity matrix $\boldsymbol{N}_i = \xi_i \boldsymbol{I}_3$. The displacements $\mathbf{u}_i$ are vectors made of three components u_x, u_y and u_z, representing the displacement in the three directions, equal to $\mathbf{u}_i = [\ \mathrm{u}_{x,i}, \mathrm{u}_{y,i}, \mathrm{u}_{z,i}\ ]^T$.

In order to express everything as a function of the displacements, the strain vector $\boldsymbol{\epsilon}$, recalling equation (3.17), can be written in a compact form as

$$\boldsymbol{\epsilon} = L\boldsymbol{u} \tag{3.39}$$

where L is the first order differential operator relating strains and displacements.

As the strains are constant inside the element, also the stresses, in agreement, are constant in each element. Hence, the effective stress $\boldsymbol{\sigma}$ is expressed through the constitutive model, that can be written in the incremental form as:

$$d\boldsymbol{\sigma} = D_t d\boldsymbol{\epsilon} \tag{3.40}$$

where D_t is the tangent constitutive matrix.

In order to solve the problem, proper boundary conditions are required. In general, three types of boundary conditions can be assumed:

- Dirichlet conditions: defined on the unknown function u;
- Neumann conditions: defined on the derivative of the unknown function $\frac{\partial u}{\partial n}$, with n the normal direction to the boundary;
- Cauchy conditions: defined on the function and its derivatives.

In the application described in this thesis, only Dirichlet and Neumann conditions are considered. In particular, referring to the structural problem, Dirichlet conditions represent imposed displacements while Neumann conditions represent applied forces.

3.5.2 Solution of the structural problem with interface elements

The just introduced FE method is applied in order to numerically solve the variational equation (3.34) using a node-to-node formulation, as explained by Franceschini et al. [2016]. Based on equation (3.38), the displacement of a point $\boldsymbol{u}(\mathbf{x})$ is approximated with the function $\boldsymbol{u}^h(\mathbf{x}) \in \mathcal{U}^h$, where $\mathcal{U}^h$ is the Hilbert function space generated by the

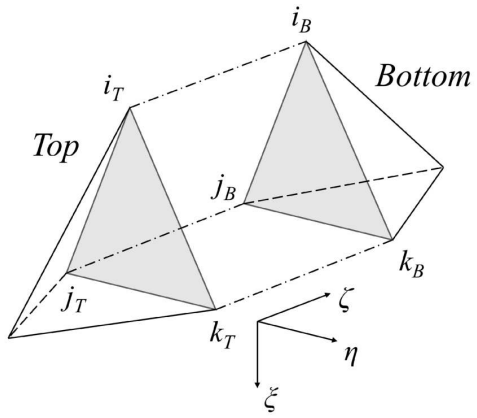

FIGURE 3.3: Interface Element.

piecewise polynomials l_i, with $i = 1, ..., n_\Omega$ as n_Ω is the number of nodes in Ω:

$$\boldsymbol{u}^h(\mathbf{x}) = \begin{bmatrix} u_x^h(\mathbf{x}) \\ u_y^h(\mathbf{x}) \\ u_z^h(\mathbf{x}) \end{bmatrix} = \begin{bmatrix} \sum_{i=1}^{n_\Omega} l_i(\mathbf{x}) \mathrm{u}_{x,i} \\ \sum_{i=1}^{n_\Omega} l_i(\mathbf{x}) \mathrm{u}_{y,i} \\ \sum_{i=1}^{n_\Omega} l_i(\mathbf{x}) \mathrm{u}_{z,i} \end{bmatrix} = N_u(\mathbf{x})\mathbf{u} \tag{3.41}$$

In a similar way also the fault strength $\boldsymbol{\lambda}(\mathbf{x})$ can be approximated with the function $\boldsymbol{\lambda}^h(\mathbf{x}) \in \mathcal{L}^h$, where $\mathcal{L}^h$ is another Hilbert function space generated by the piecewise polynomials ϕ_j, with $j = 1, ..., n_\Gamma$ as n_Γ is the number of nodes in Γ_T and Γ_B:

$$\boldsymbol{\lambda}^h(\mathbf{x}) = \begin{bmatrix} \lambda_x^h(\mathbf{x}) \\ \lambda_y^h(\mathbf{x}) \\ \lambda_z^h(\mathbf{x}) \end{bmatrix} = \begin{bmatrix} \sum_{j=1}^{n_\Gamma} \phi_j(\mathbf{x}) \lambda_{x,j} \\ \sum_{j=1}^{n_\Gamma} \phi_j(\mathbf{x}) \lambda_{y,j} \\ \sum_{j=1}^{n_\Gamma} \phi_j(\mathbf{x}) \lambda_{z,j} \end{bmatrix} = N_\lambda(\mathbf{x})\boldsymbol{\lambda}_g \tag{3.42}$$

To simulate the opening and slippage of faults in a discrete domain using the Finite Element method, it is necessary to introduce a special type of element called Interface Element (IE). These particular elements, first introduced by Goodman et al. [1968], allow to violate the congruence of displacements which is always assured by the traditional finite elements. The IE has no thickness and it is composed of two triangular finite elements located each one on a contact surface of the fault. The nodes are then set as couples having the same coordinates (Figure 3.3).

It is more convenient to consider a local reference system for the elements present

on the surfaces Γ_T and Γ_B in order to express the fault strength. The local system $\xi - \eta - \zeta$ is composed such that the ζ axis is directed in the normal direction to the contact surface and conventionally oriented from Γ_T to Γ_B; while the other two axes, ξ and η, are defined to complete the anticlockwise tern. To switch from the local strength $\boldsymbol{\lambda}$ to the global vector $\boldsymbol{\lambda}_g$ a rotation matrix R is introduced such that:

$$\boldsymbol{\lambda}^h(\mathbf{x}) = N_\lambda R\boldsymbol{\lambda} = N_\lambda \boldsymbol{\lambda}_g \tag{3.43}$$

Considering equation (3.41), the relations (3.39) and (3.40) can be written as

$$\boldsymbol{\epsilon}^h = L\boldsymbol{u}^h = LN_u\mathbf{u} = B\mathbf{u} \tag{3.44}$$

$$d\boldsymbol{\sigma}^h = D_t d\boldsymbol{\epsilon}^h \tag{3.45}$$

where B is the strain matrix.

The novel contribution to the equation (3.34) is due to the presence of the virtual work of the fault. The relative displacement $\boldsymbol{u}_r^h$ along $\bar{\Gamma}$ in the discrete space $\mathcal{U}^h$ is defined as:

$$\boldsymbol{u}_r^h = \boldsymbol{u}_B^h - \boldsymbol{u}_T^h \tag{3.46}$$

where $\boldsymbol{u}_T^h$ and $\boldsymbol{u}_B^h$ are the restriction of $\boldsymbol{u}^h$ over $\bar{\Gamma}_T$ and $\bar{\Gamma}_B$, respectively. Introducing the matrices S_1 and S_2, mapping the nodal displacements on the fault surfaces from the global nodal displacement vector $\mathbf{u}$, the result is:

$$\boldsymbol{u}_r^h = N_u S_2\mathbf{u} - N_u S_1\mathbf{u} = N_u S\mathbf{u} \tag{3.47}$$

where $S = S_2 - S_1$.

A brief explanation of the matrices of the local unknowns at the element level is now presented. Considering a single element e, as the one in Figure 3.3, and the relations

(3.46) and (3.47), the displacement $\mathbf{u}_r^{(e)}$ is:

$$\mathbf{u}_r^{(e)} = \begin{bmatrix} \mathbf{u}_{r,i} \\ \mathbf{u}_{r,j} \\ \mathbf{u}_{r,k} \end{bmatrix} = \begin{bmatrix} -I_3 & I_3 & 0 & 0 & 0 & 0 \\ 0 & 0 & -I_3 & I_3 & 0 & 0 \\ 0 & 0 & 0 & 0 & -I_3 & I_3 \end{bmatrix} \cdot \begin{bmatrix} \mathbf{u}_{T,i} \\ \mathbf{u}_{B,i} \\ \mathbf{u}_{T,j} \\ \mathbf{u}_{B,j} \\ \mathbf{u}_{T,k} \\ \mathbf{u}_{B,k} \end{bmatrix} = S^{(e)}\mathbf{u}^{(e)} \tag{3.48}$$

where $\mathbf{u}_{r,q}$ is the vector containing the three components of the relative displacements along x, y and z between the opposite nodes q_T and q_B, while I_3 is the identity matrix 3×3. The matrix $N_u^{(e)}(\mathbf{x})$ of the local basis functions is then equal to:

$$N_u^{(e)}(\mathbf{x}) = \begin{bmatrix} \psi_i^{(e)} I_3 & \psi_j^{(e)} I_3 & \psi_k^{(e)} I_3 \end{bmatrix} \tag{3.49}$$

where the function $\psi_q^{(e)}(\mathbf{x})$ is the restriction on the IE e of the basis functions $l_{T,q}(\mathbf{x})$ and $l_{B,q}(\mathbf{x})$ as introduced in equation (3.41).

The same approach can be followed starting from equation (3.43) in order to write $\boldsymbol{\lambda}^{(e)}$ as:

$$\boldsymbol{\lambda}^{(e)} = \begin{bmatrix} \boldsymbol{\lambda}_i \\ \boldsymbol{\lambda}_j \\ \boldsymbol{\lambda}_k \end{bmatrix} \tag{3.50}$$

where $\boldsymbol{\lambda}_q$ is the vector containing the three components of nodal strength in the local axes ξ, η and ζ between the nodes q_T and q_B. Using the rotation matrix $R^{(e)}$, the matrix $N_\lambda^{(e)}(\mathbf{x})$ of the local basis functions is equal to:

$$N_\lambda^{(e)}(\mathbf{x}) = \begin{bmatrix} \phi_i^{(e)} I_3 & \phi_j^{(e)} I_3 & \phi_k^{(e)} I_3 \end{bmatrix} \tag{3.51}$$

where the function $\phi_q^{(e)}(\mathbf{x})$ is the restriction on the IE e of the basis functions $\phi_{T,q}(\mathbf{x})$ and $\phi_{B,q}(\mathbf{x})$ as introduced in equation (3.42). In particular, $\phi_q(\mathbf{x})$ is the piecewise constant

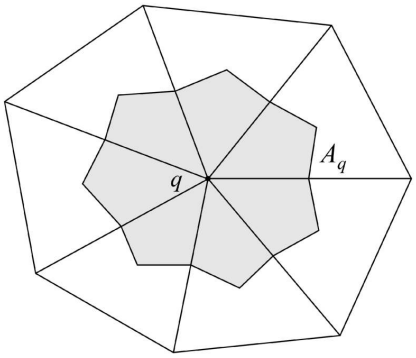

FIGURE 3.4: Partitioning of the areas connected to one node.

function such that:

$$\phi_q(\mathbf{x}) = \begin{cases} 1 & \text{if } \mathbf{x} \in A_q \\ 0 & \text{if } \mathbf{x} \notin A_q \end{cases} \tag{3.52}$$

Specifically, in equation (3.52) A_q is the area associated to the node q (Figure 3.4):

$$A_q = \sum_e \frac{A^{(e)}}{3} \tag{3.53}$$

where $A^{(e)}$ is the area of the triangle e and the sum is performed considering all the triangles sharing the node q.

Focusing again on the contact problem, the discrete shear strength $\boldsymbol{\tau}_L^h$ along $\bar{\Gamma}$ is related to τ_L and $\boldsymbol{u}_r^h$ as previously indicated in equation (3.26). Considering also the discrete function $\boldsymbol{\lambda}^h$ defined in equation (3.43) and the Mohr-Coulomb criterion (3.24), τ_L can be written as:

$$\tau_L = c - \tan\varphi \boldsymbol{n}^T N_\lambda R \boldsymbol{\lambda} \tag{3.54}$$

where $\boldsymbol{n}$ is the normal vector to the fault surface $\bar{\Gamma}$, conventionally oriented from Γ_T to Γ_B.

Substituting the relations (3.47) and (3.54) in the principle of maximum plastic dissipation (3.26), the expression of $\boldsymbol{\tau}_L^h$ will become:

$$\boldsymbol{\tau}_L^h = (c - \tan\varphi \boldsymbol{n}^T N_\lambda R \boldsymbol{\lambda}) \frac{N_u S \mathbf{u}}{\sqrt{\mathbf{u}^T S^T N_u^T N_u S \mathbf{u}}} = (c - \tan\varphi \boldsymbol{n}^T N_\lambda R \boldsymbol{\lambda}) \frac{N_u S \mathbf{u}}{\|\mathbf{u}\|_H} \tag{3.55}$$

In equation (3.55) the H-energy norm of $\mathbf{u}$ has been introduced, which is equal to:

$$\|\mathbf{u}\|_H = \sqrt{\mathbf{u}^T H \mathbf{u}} \tag{3.56}$$

where H is the matrix $H = S^T N_u^T N_u S$. Based on Franceschini et al. [2016], it can be proved that matrix H is positive semi-definite because S has not full rank, hence the energy norm can be zero even when $\mathbf{u} \neq 0$ and this is why it is called semi-norm.

Substituting all the approximations just defined in the general equation of the virtual work principle (3.34), the final numerical model reads:

$$\begin{aligned}\delta\mathbf{u}^T \int_\Omega B^T \boldsymbol{\sigma}^h \, dV + \delta\mathbf{u}^T \int_{\Gamma\setminus\bar{\Gamma}} S^T N_u^T N_\lambda R \boldsymbol{\lambda} \, dS + \delta\boldsymbol{\lambda}^T \int_{\Gamma\setminus\bar{\Gamma}} R^T N_\lambda^T N_u S \mathbf{u} \, dS + \\ + \delta\mathbf{u}^T \int_{\bar{\Gamma}} (c - \tan\varphi \boldsymbol{n}^T N_\lambda R \boldsymbol{\lambda}) \frac{H\mathbf{u}}{\|\mathbf{u}\|_H} \, dS = \\ = \delta\mathbf{u}^T \int_\Omega B^T \boldsymbol{i} \alpha p \, dV + \delta\mathbf{u}^T \int_\Omega N_u^T \boldsymbol{b} \, dV + \delta\mathbf{u}^T \int_{\partial\Omega} N_u^T \boldsymbol{t} \, dS\end{aligned} \tag{3.57}$$

As the virtual displacement $\delta\mathbf{u}$ and the virtual strength $\delta\boldsymbol{\lambda}$ are variable, the equation (3.57) must be true for any of their configuration. Hence, defining C and $\boldsymbol{f}$ as follow:

$$C = \int_{\Gamma\setminus\bar{\Gamma}} S^T N_u^T N_\lambda R \, dS \tag{3.58}$$

$$\boldsymbol{f} = \int_\Omega B^T \boldsymbol{i} \alpha p \, dV + \int_\Omega N_u^T \boldsymbol{b} \, dV + \int_{\partial\Omega} N_u^T \boldsymbol{t} \, dS \tag{3.59}$$

equation (3.57) can be written in the form of a non-linear system, with $\mathbf{u}$ and $\boldsymbol{\lambda}$ as the unknowns:

$$\begin{cases} \int_\Omega B^T \boldsymbol{\sigma}^h \, dV + C\boldsymbol{\lambda} + \int_{\bar{\Gamma}} (c - \tan\varphi \boldsymbol{n}^T N_\lambda R \boldsymbol{\lambda}) \frac{H\mathbf{u}}{\|\mathbf{u}\|_H} \, dS - \boldsymbol{f} = 0 \\ C^T \mathbf{u} = 0 \end{cases} \tag{3.60}$$

The system can be defined in a more compact way as:

$$\begin{cases} \boldsymbol{F}_1(\mathbf{u}, \boldsymbol{\lambda}) = 0 \\ \boldsymbol{F}_2(\mathbf{u}, \boldsymbol{\lambda}) = 0 \end{cases} \tag{3.61}$$

The system (3.61) can be solved using the Newton-Raphson scheme. The Jacobian matrix $J(\mathbf{u}, \boldsymbol{\lambda})$ is composed of four blocks:

$$J(\mathbf{u}, \boldsymbol{\lambda}) = \begin{bmatrix} \frac{\partial \boldsymbol{F}_1}{\partial \mathbf{u}} & \frac{\partial \boldsymbol{F}_1}{\partial \boldsymbol{\lambda}} \\ \frac{\partial \boldsymbol{F}_2}{\partial \mathbf{u}} & \frac{\partial \boldsymbol{F}_2}{\partial \boldsymbol{\lambda}} \end{bmatrix} = \begin{bmatrix} J_{11} & J_{12} \\ J_{21} & J_{22} \end{bmatrix} \tag{3.62}$$

where:

$$J_{11} = \frac{\partial \boldsymbol{F}_1}{\partial \mathbf{u}} = \int_\Omega B^T D_t B \, dV + \int_{\bar{\Gamma}} (c - \tan\varphi \boldsymbol{n}^T N_\lambda R \boldsymbol{\lambda}) \frac{\|\mathbf{u}\|_H^2 H - (H\mathbf{u})(H\mathbf{u})^T}{\|\mathbf{u}\|_H^3} \, dS =$$

$$= K(\mathbf{u}) + E(\mathbf{u}, \boldsymbol{\lambda}) \tag{3.63}$$

$$J_{12} = \frac{\partial \boldsymbol{F}_1}{\partial \boldsymbol{\lambda}} = C - \int_{\bar{\Gamma}} \tan\varphi \frac{H\mathbf{u}}{\|\mathbf{u}\|_H} \boldsymbol{n}^T N_\lambda R \, dS = C - F(\mathbf{u}) \tag{3.64}$$

$$J_{21} = \frac{\partial \boldsymbol{F}_2}{\partial \mathbf{u}} = C^T \tag{3.65}$$

$$J_{22} = \frac{\partial \boldsymbol{F}_2}{\partial \boldsymbol{\lambda}} = 0 \tag{3.66}$$

The solution $(\mathbf{u}, \boldsymbol{\lambda})$ is obtained using an iterative procedure and starting from an initial value $(\mathbf{u}^{(0)}, \boldsymbol{\lambda}^{(0)})$:

$$\begin{bmatrix} \mathbf{u}^{(k+1)} \\ \boldsymbol{\lambda}^{(k+1)} \end{bmatrix} = \begin{bmatrix} \mathbf{u}^{(k)} \\ \boldsymbol{\lambda}^{(k)} \end{bmatrix} + \begin{bmatrix} \Delta\mathbf{u} \\ \Delta\boldsymbol{\lambda} \end{bmatrix} \tag{3.67}$$

where the corrections $\Delta\mathbf{u}$ and $\Delta\boldsymbol{\lambda}$ are computed solving a linear system with the Jacobian matrix $J^{(k)} = J(\mathbf{u}^{(k)}, \boldsymbol{\lambda}^{(k)})$:

$$J^{(k)} \begin{bmatrix} \Delta\mathbf{u} \\ \Delta\boldsymbol{\lambda} \end{bmatrix} = - \begin{bmatrix} \boldsymbol{F}_1(\mathbf{u}^{(k)}, \boldsymbol{\lambda}^{(k)}) \\ \boldsymbol{F}_2(\mathbf{u}^{(k)}, \boldsymbol{\lambda}^{(k)}) \end{bmatrix} \tag{3.68}$$

The Newton-Raphson procedure is said to be convergent if some vector norm value is lower than a prefixed tolerance. Typical norms are the norm of the displacement increment and the norm of the unbalanced forces. The norms are usually normalized by their initial value. In this thesis the norm of unbalanced forces has been chosen.

Chapter 4

Model application

The FE model previously described has been applied to simulate the geomechanical response of the reservoir and its surroundings due to the gas storage activity. In the following sections the construction of the mesh, the calibration and application of the flow and geomechanical models are presented. Finally, the modeling results are shown and discussed.

4.1 Mesh definition

The first step is the definition of the computational domain and its discretization: the domain should be large enough to avoid that the imposed boundary conditions can affect the simulation outcomes in the reservoir area; moreover, the mesh resolution has to be larger in the area of the reservoir to accurately reproduce the geologic structure. Thus, it is elected to use a model domain with a dimension of 42 x 30 km and with the reservoir position almost at the center. As previously stated, the 3D mesh is composed of tetrahedra, hence the 2D elements are triangles with an average size of about 50 m in the reservoir area, in agreement with the grid dimension in the Eclipse model, and then increasing towards the boundary up to about 2,000 m. The 2D mesh has been created using the software Argus ONE by Argus Holdings [1997] and consists of 13,301 nodes and 26,526 elements (Figure 4.1).

The 3D mesh has been built using a mesh generator which, basically, projects the 2D mesh nodes in the vertical direction, taking into account the stratigraphy. Based on the maps at regional scale provided by Stogit S.p.A., the model has been subdivided into 11 macro-layers. However, as the reservoir area must be more refined and all these

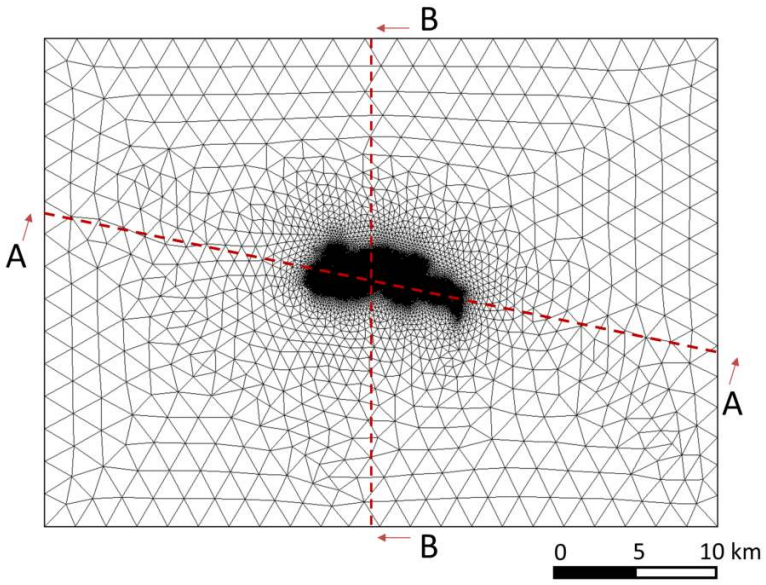

FIGURE 4.1: The 2D mesh used to build the 3D mesh. The reservoir is located in the center where the mesh is more refined. In red are indicated the sections A-A and B-B.

layers have different thickness, each geological unit has been further subdivided for a total number of layers equal to 41, as reported in Table 4.1. In particular, the number of layers composing the macro-layers of Pool A, the interlayer and Pool C are 5, 3 and 8, respectively, in agreement with the Eclipse model.

For simplicity, seven soil types are considered in the model:

1. surrounding rock (everything that is not reservoir or aquifers);
2. aquifer around Pool A;
3. aquifer of the interlayer between the pools;
4. aquifer around Pool C;
5. Pool A;
6. interlayer between the pools;
7. Pool C.

The presence of faults within the domain requires the introduction of IEs on their surfaces, therefore the total node number increases since, for these elements, for each

Surface name	Elevation [m]	Number of layers
DEM	50	2
Alluvial base	-346	2
Santerno top (Asti base)	-1,024	2
Upper Pliocene sands base	-1,152	3
Pool A top (Pliocene base)	-1,410	5
Pool A base	-1,476	3
Pool C top	-1,498	8
Pool C base	-1,515	2
Miocene clays top (Miocene sands base)	-1,543	2
Marls top	-1,543	10
Limestones top	-8,655	2
Model bottom	-10,000	—

TABLE 4.1: The major surfaces considered in the geomechanical model. They are listed from top to bottom together with the elevation relative to the point A016VJP (see Figure 2.15 for the position). The number of layers is referred to the subdivision between that surface and the one below it.

position the nodes are duplicated. The final 3D mesh is therefore composed of 496,136 nodes and 2,891,095 tetrahedral elements in the continuous case, while in the faulted case the nodes are 508,495 with a total number of 26,598 interface elements.

4.2 Calibration of the models

One of the key aspects of the model calibration regards the relation expressing the vertical uniaxial compressibility c_M as a function of the effective vertical stress σ_z. Based on the works by Baú et al. [2002] and Ferronato et al. [2013] for the Northern Adriatic sedimentary basin, the relation for virgin loading (I loading cycle) is

$$c_M = 1.0044 \times 10^{-2} \sigma_z^{-1.1347} \tag{4.1}$$

where σ_z is in MPa and c_M in MPa^{-1}. However, during the UGS cycles the relation differs as the compressibility in unloading/reloading conditions (II loading cycle) must

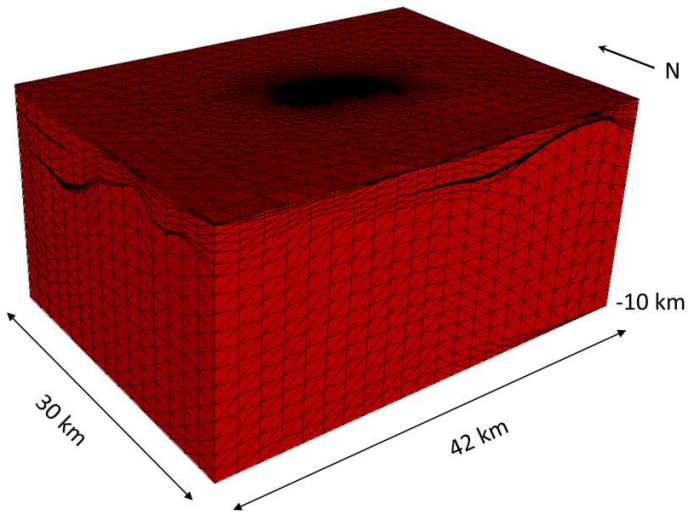

FIGURE 4.2: Axonometric view of the 3D FE model. The vertical scale is exaggerated by a factor 2 with respect to the horizontal one.

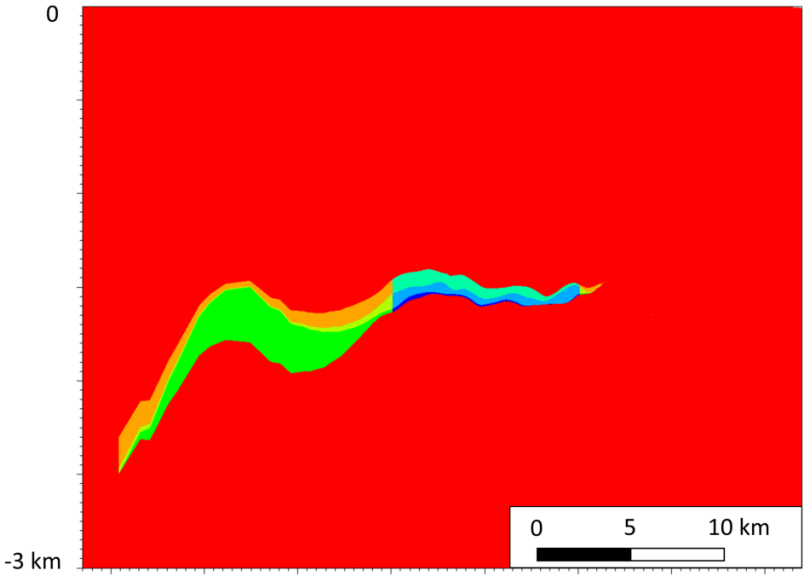

FIGURE 4.3: Vertical section along the alignment A-A in Figure 4.1 viewed from SW to NE. The colors represent the seven adopted materials. The vertical scale is exaggerated by a factor 10 with respect to the horizontal one.

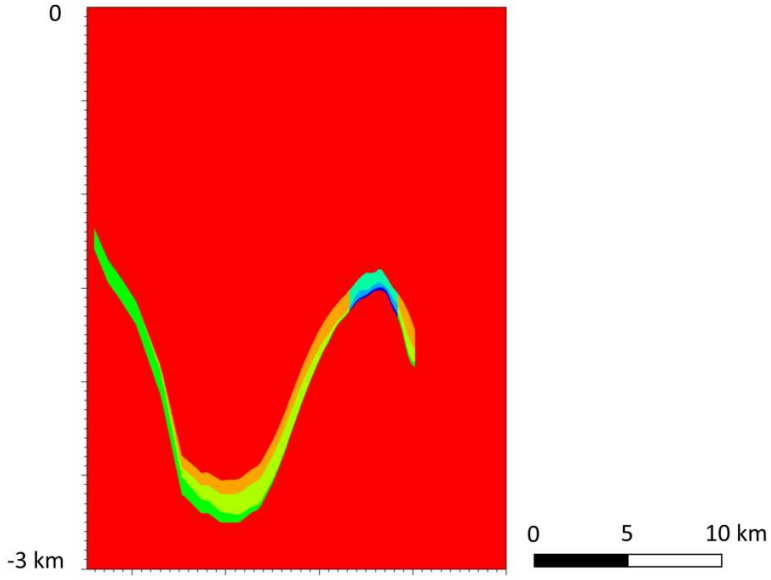

FIGURE 4.4: Vertical section along the alignment B-B in Figure 4.1 viewed from East to West. The colors represent the seven adopted materials. The vertical scale is exaggerated by a factor 10 with respect to the horizontal one.

be considered. c_R is the ratio between loading and unloading/reloading compressibility at the load inversion and has been estimated between 3.5 - 4.0 for σ_z from 20 to 30 MPa in the case studies investigated by Ferronato et al. [2013]. This range, which was derived from InSAR measurements above UGS reservoirs, is in good agreement with the outcomes by Baú et al. [2002] and Ferronato et al. [2003] based on in-situ compaction/expansion measurements of deep reservoirs carried out by the radioactive marker technique. Hence, the constitutive matrix in equation (3.22) for transversely isotropic material has been implemented in the FE geomechanical model using the non-linear relationship in equation (4.1) for the vertical compressibility, and the ratio c_R to obtain the II cycle compressibility at the load inversion. As a result, a non-linear hysteretic hypo-plastic model is used, the calibration of which is assessed by detecting a proper value of c_R.

4.2.1 Flow model

Groundwater flow simulations in saturated conditions were carried out to propagate the pressure variations from the reservoir in the hydraulically connected aquifers. This procedure has been applied starting from the information obtained from the Eclipse

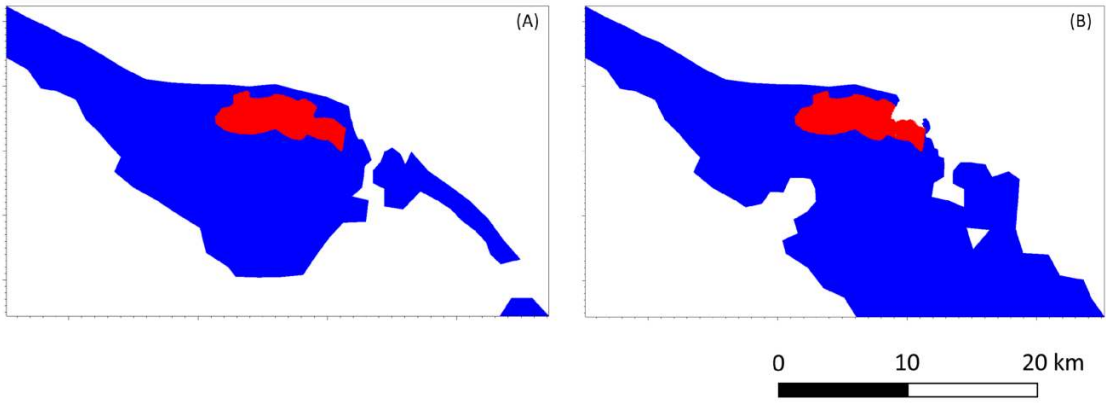

FIGURE 4.5: Plan view of the two sub-meshes used for the flow simulation: (A) for Pool A and (B) for Pool C. The red area is the reservoir while the blue is the aquifer.

models and considering the propagation limited by the regional faults according to Stogit S.p.A. information. Two sub-meshes, one for each pool (Figure 4.5), have been extracted from the global 3D mesh in order to apply the flow model only in the interested layers, thus reducing the computational burden. The pressure field obtained by the simulation is then used in the geomechanical model as forcing factor. The sub-meshes do not contain the interface elements as the presence of the faults is not accounted for in this part of the work.

To calibrate the flow model, the most important parameter to set is the average hydraulic conductivity of the aquifer. By satisfying the so-called material balance equation, a calibration procedure based on trial and error allows one to numerically estimate the average hydraulic conductivity of the aquifer. This balance consists in the constraint that the sum of the residual hydrocarbon volume and the interstitial water volume in each pool of the reservoir, the volume of water encroached from the adjacent aquifer, and the loss of pore volume due to the reservoir compaction must be constant any time during the production life (Teatini et al. [2011], Ferronato et al. [2004]). The calibration is typically carried out at the end of the field production, when the field experiences the largest change in pore fluid pressure. The water volume that entered the reservoir (which obviously depends on the average aquifer hydraulic conductivity, i.e., the parameter that must be calibrated) must equal the reservoir pore volume made

	K_x [m/s]	K_y [m/s]	K_z [m/s]	ϕ [-]
Pool A	2.04×10^{-7}	2.04×10^{-7}	2.04×10^{-8}	0.20
Pool C	2.04×10^{-7}	2.04×10^{-7}	2.04×10^{-8}	0.20

TABLE 4.2: The calibrated parameters adopted in the final flow simulations: the average hydraulic conductivity along in the three reference directions and the porosity.

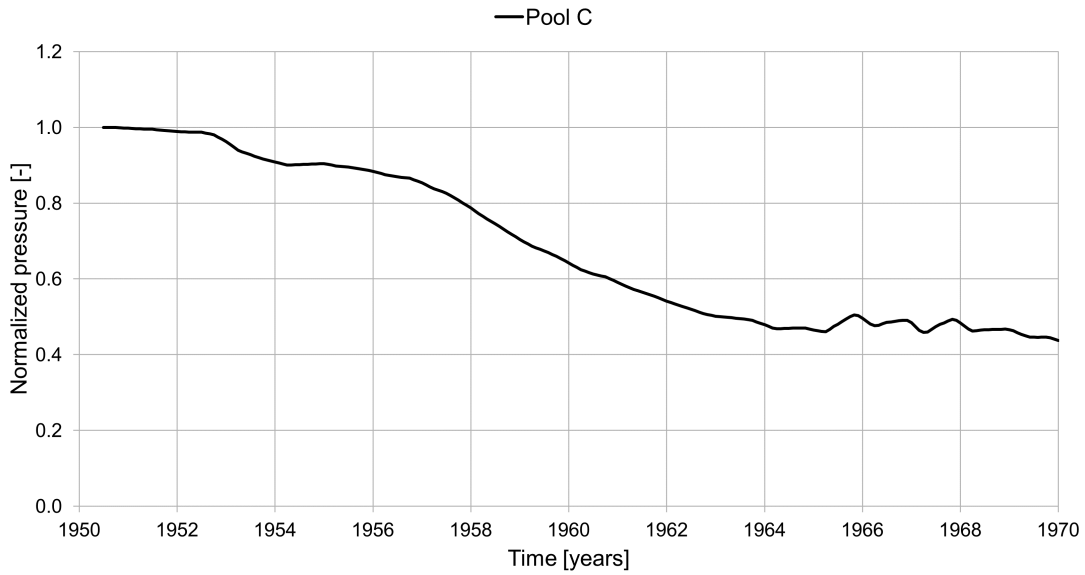

FIGURE 4.6: Behaviour versus time of the normalized average pressure in Pool C during the primary production phase.

available by gas production as provided by the Eclipse production model. For example, the target volume for Pool C was of 3.78×10^6 m^3 and the volume from the flow model is 3.75×10^6 m^3. For the first tests, some other similar works such as Teatini et al. [2000], Ferronato et al. [2004] and Teatini et al. [2011] have been taken into account to estimate a range of possible values. The final parameters adopted in the flow model, both for Pool A and Pool C, are reported in Table 4.2.

An example of pressure variation, referred to the sub-mesh of Pool C, is presented in the following. Based on the graph in Figure 4.6, the pressure drops in 1960 and 1964 (at the end of the primary production) are about 35% and 52% of the initial value, respectively. Figures 4.7 and 4.8 show the pressure variations propagating in the surrounding aquifers at these dates. Within the reservoir, the values agree with those provided in Figure 4.6.

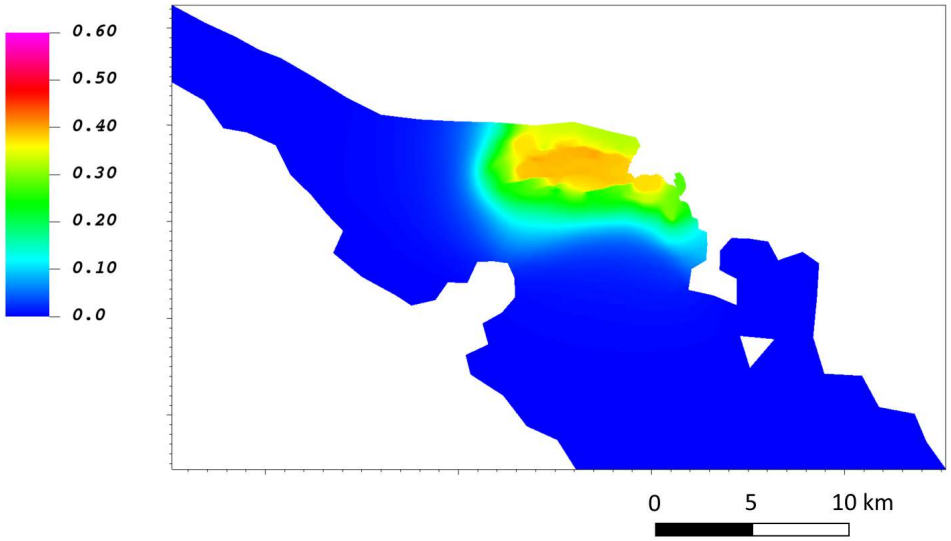

FIGURE 4.7: Normalized pressure variation in Pool C and its hydraulically connected aquifer in 1960.

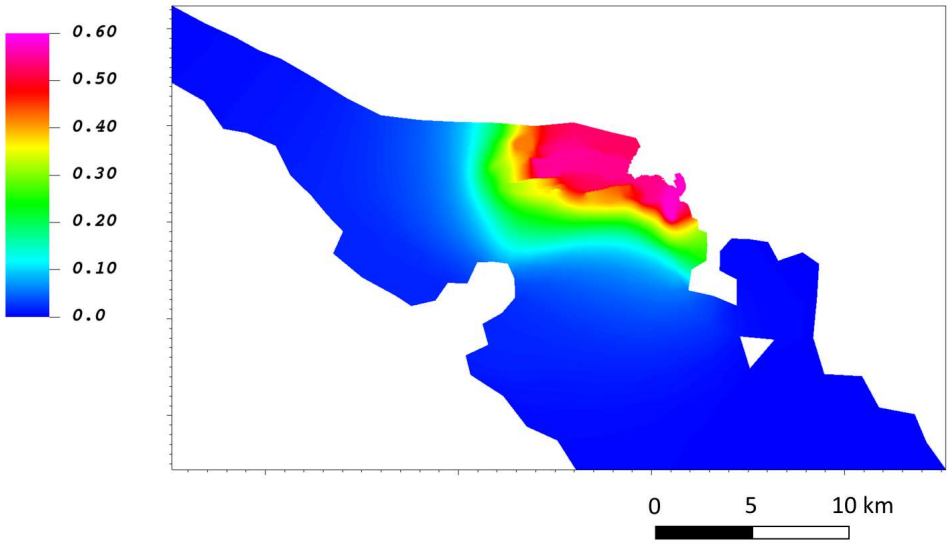

FIGURE 4.8: Normalized pressure variation in Pool C and its hydraulically connected aquifer in 1964.

4.2.2 Geomechanical model

The geomechanical model is applied to simulate land displacements and stresses associated to primary production and UGS phases. The model application requires to specify appropriate boundary conditions. For this work, Dirichlet conditions are imposed on the lateral and bottom surfaces of the domain, considering zero displacements along the three directions. A traction-free surface has been specified on the model top. Moreover, the pressure variations obtained using the flow model are now used as external forces. The model is initially applied to the continuous case, hence without the interface elements, and only in a second stage the faults presence and their possible activation are addressed.

The calibration has been performed using the land displacement dataset made available by InSAR during the UGS activity. As presented in Section 2, the available data cover the period from 2003 to 2021.

In the model calibration different constitutive laws for the soil can be used: the most common constitutive relationships are the linear elastic and the hypo-plastic laws. The main difference stands in the fact that the c_M for the former case is function of the depth only, while for the latter case it depends on the actual value of the vertical stress and the loading phase. As previously explained, various geomechanical studies have obtained satisfactory results in the area of the Northern Adriatic considering an hypoplastic relationship. Hence, it has been decided to adopt the same law for the layers with pressure variations and a simpler linear elastic model for the geologic units where the pressure remained unchanged.

The model was initially run using average geomechanical values from previous modeling studies in the area. The parameter values are provided in Table 4.3. The results were compared with the available land displacements showing a good agreement, with a certain underestimate of the seasonal fluctuations related to the UGS production and injection phases. Therefore, a second test has been designed with more deformable layers where the pressure seasonally change due to UGS. This has been achieved by decreasing the value of c_R from 5 to 3 in Pool C. The comparison between measurements and model results, relative to the three sites selected within the trace of the reservoir, are shown in Figures 4.9 - 4.11. For the same three sites, Figures 4.12 - 4.14 show the

Material	ν_z	E_h/E_z	ν_h/ν_z	G_h/G_z	c_R
Elastic	0.3	1.0	1.0	1.0	-
Hypo-plastic	0.3	3.0	0.2	1.0	3 (Pool C)
					5 (Pool A and interlayer)

TABLE 4.3: Values of the calibrated parameters adopted in the final simulation of the geomechanical model. In the first trial, c_R=5 also in Pool C.

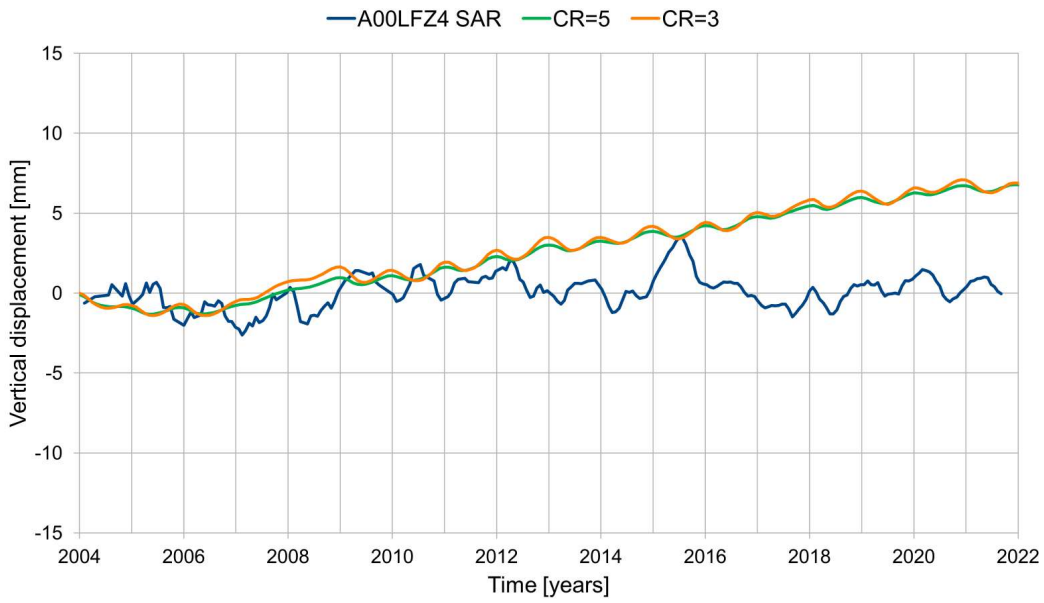

FIGURE 4.9: Comparison between the simulated vertical displacement at point A00LFZ4 (see Figure 2.15 for the position) and the measured data from 2003 to 2021. The solutions for the two values of c_R are shown.

displacements over the whole period spanned by the simulation.

The results obtained with c_R=3 for the layer corresponding to Pool C and the connected aquifer show a good match with the measurements, also catching the small details, such as the flat peak between 2017 and 2018 of point A016VNW (Figure 4.11). Thus, this calibration is adopted for the final model and the main parameters are reported in Table 4.3.

The simulated vertical displacements at the six selected points are reported from Figure 4.15 to Figure 4.20 together with the measured displacements and the pressure behaviour over time. As described above, in correspondence of the points within the trace of the reservoir the calibrated model is able to reproduce in a very good way

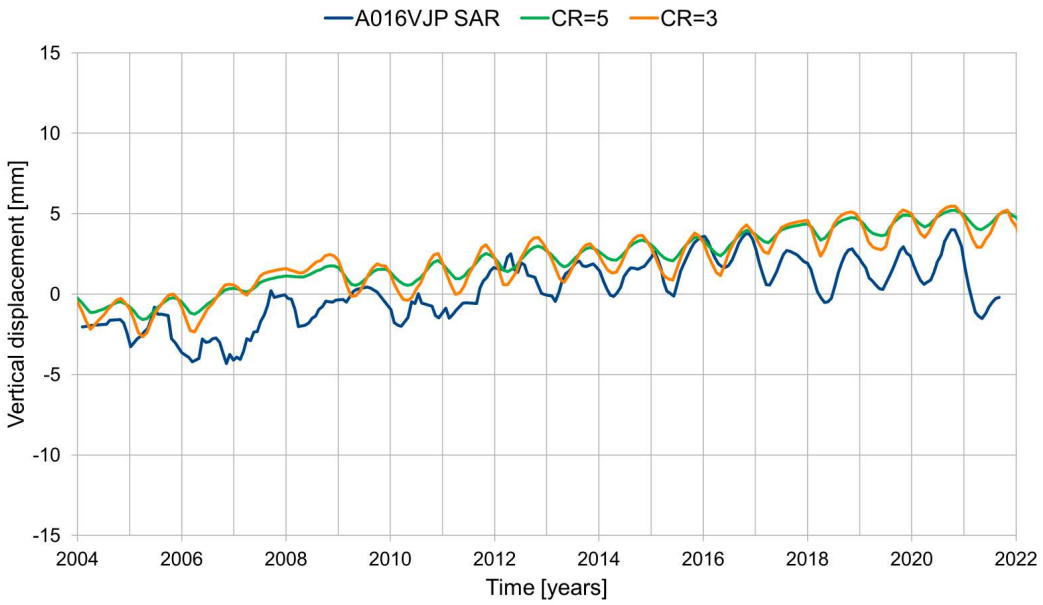

FIGURE 4.10: Comparison between the simulated vertical displacement at point A016VJP (see Figure 2.15 for the position) and the measured data from 2003 to 2021. The solutions for the two values of c_R are shown.

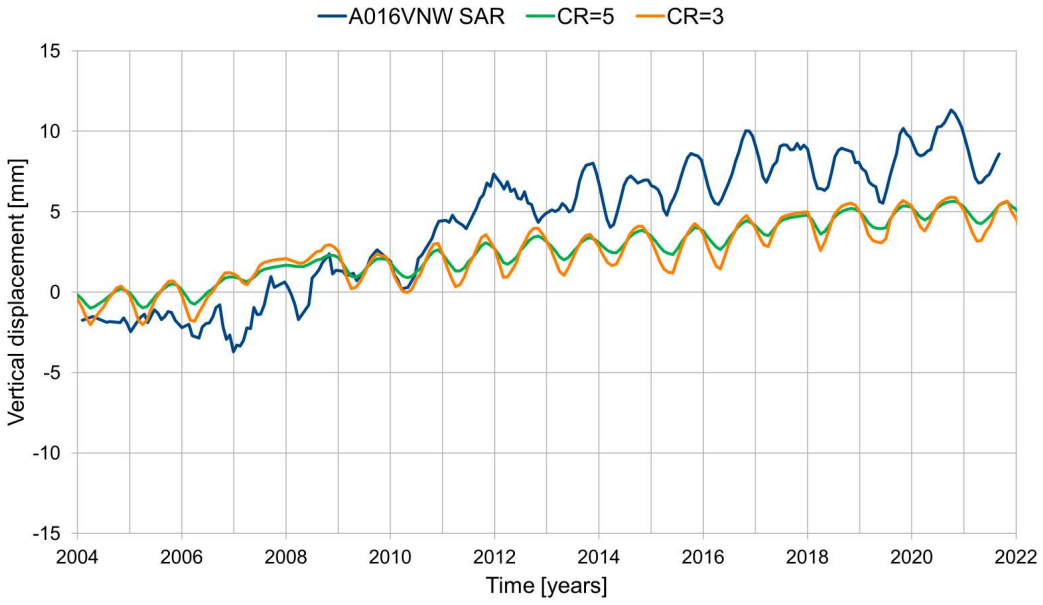

FIGURE 4.11: Comparison between the simulated vertical displacement at point A016VNW (see Figure 2.15 for the position) and the measured data from 2003 to 2021. The solutions for the two values of c_R are shown.

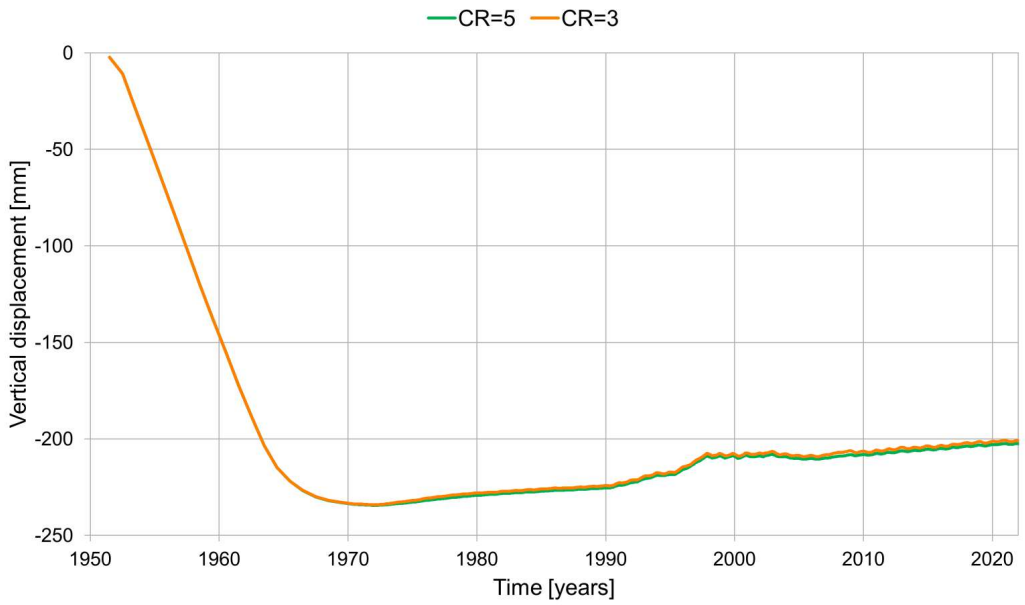

FIGURE 4.12: Comparison between the simulated vertical displacement at point A00LFZ4 (see Figure 2.15 for the position) over the entire production life (from 1950 to 2022) of the reservoir.

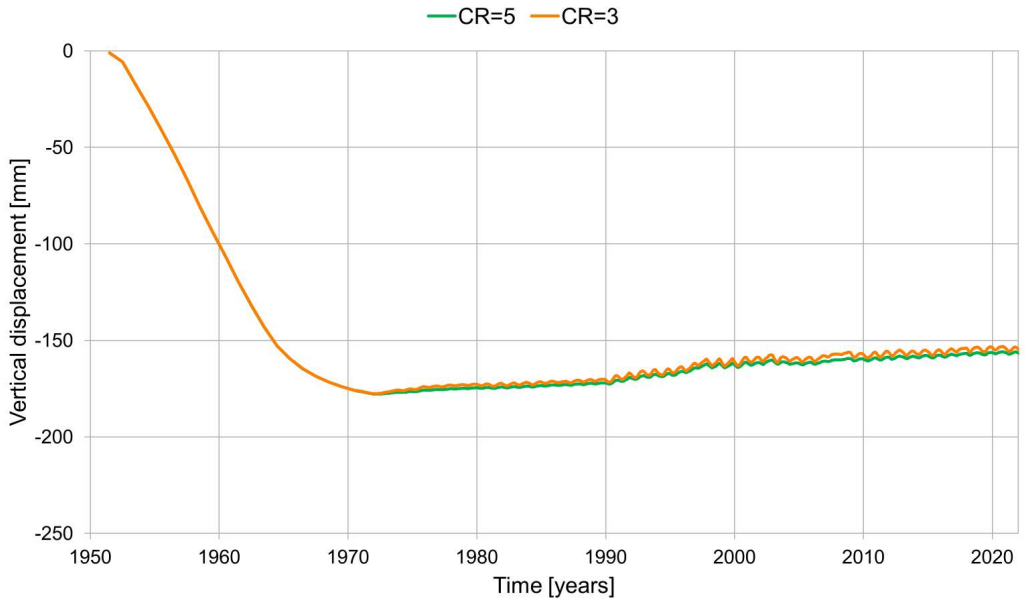

FIGURE 4.13: Comparison between the simulated vertical displacement at point A016VJP (see Figure 2.15 for the position) over the entire production life (from 1950 to 2022) of the reservoir.

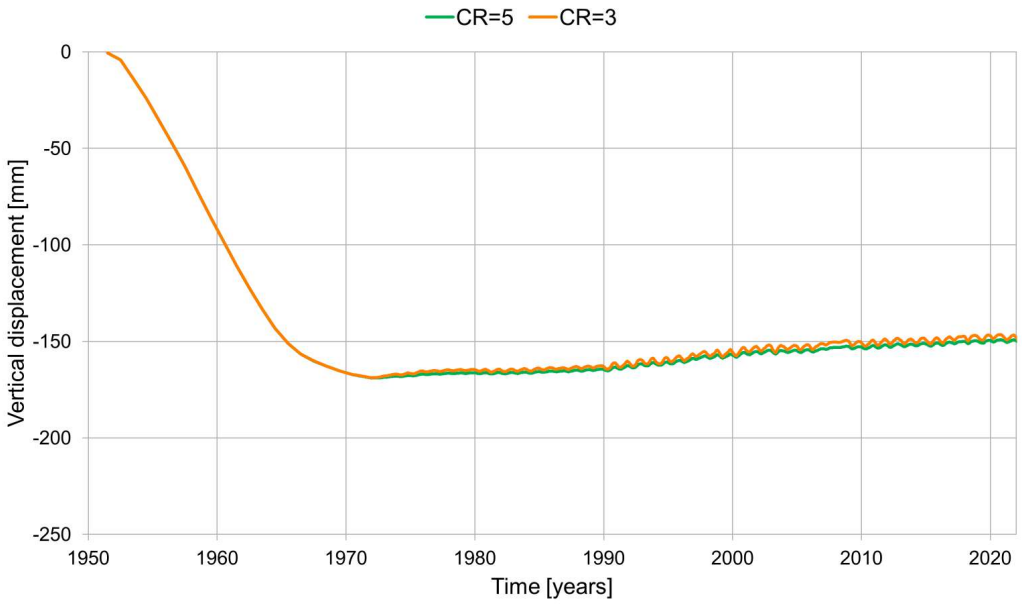

FIGURE 4.14: Comparison between the simulated vertical displacement at point A016VNW (see Figure 2.15 for the position) over the entire production life (from 1950 to 2022) of the reservoir.

the measured displacements, especially from 2013. The long trend of the vertical displacements is sometimes slightly overestimated (Figure 4.15) or underestimated (Figure 4.17), with differences less than 1 mm/year. Therefore, in general, the match is satisfactory. For the positions selected outside the trace of the reservoir, the comparison with the InSAR measurements shows a negligible correlation with the pressure behavior in the reservoir (Figures 4.18 - 4.20). Substantially, the observed fluctuations are the "characteristic" noise of this type of displacement monitoring technique. Consistently, the simulated displacements do no show any clear cyclic fluctuation but only a slight uplift trend.

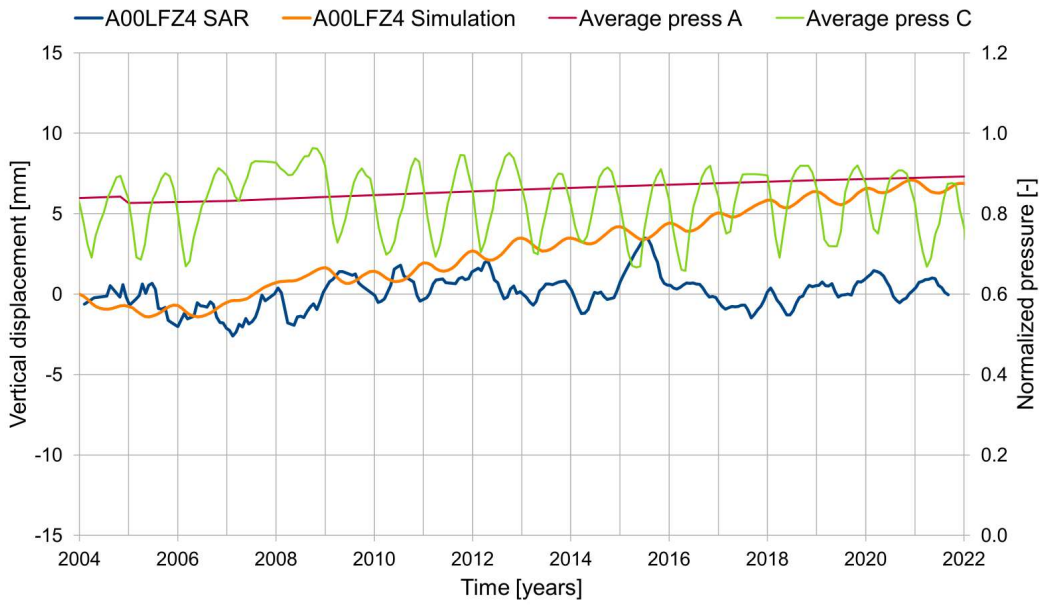

FIGURE 4.15: Comparison between the simulated vertical displacement at point A00LFZ4 (see Figure 2.15 for the position) with the final calibration and the measured displacement. The average pressure in Pool A and Pool C between 2003 and 2021 are also provided.

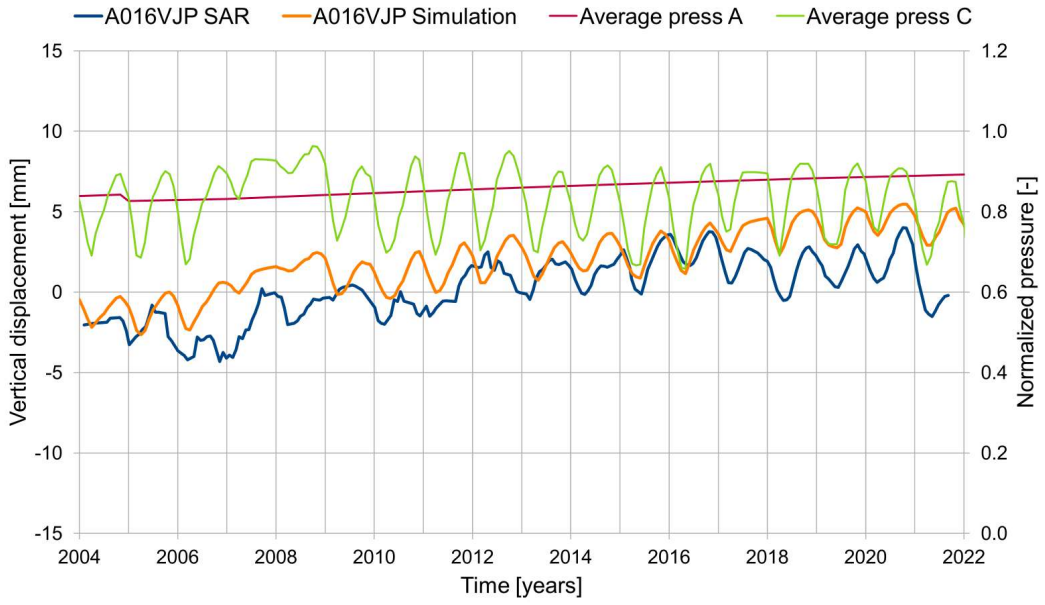

FIGURE 4.16: Comparison between the simulated vertical displacement at point A016VJP (see Figure 2.15 for the position) with the final calibration and the measured displacement. The average pressure in Pool A and Pool C between 2003 and 2021 are also provided.

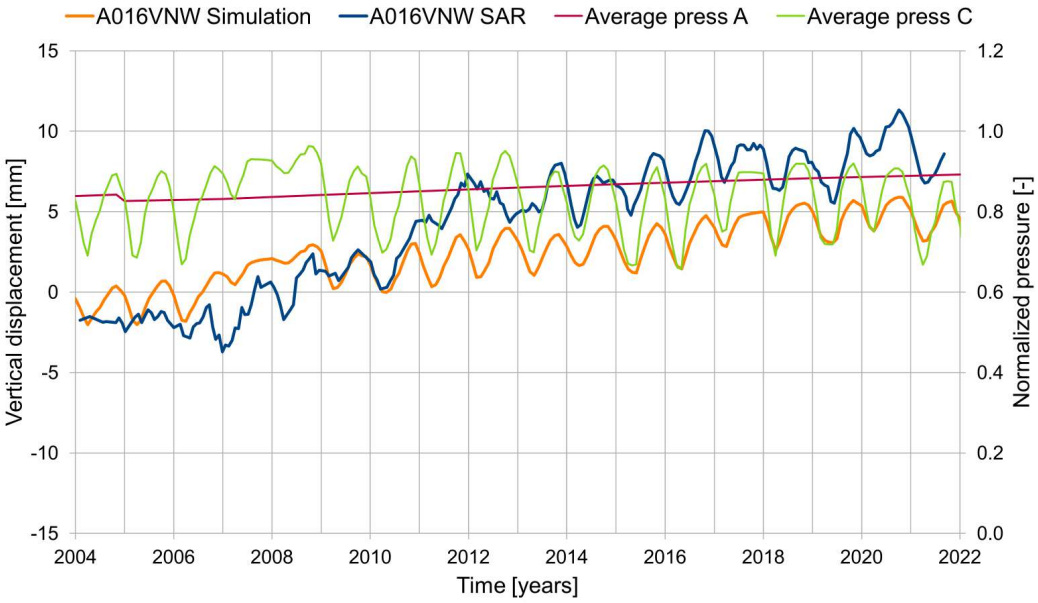

FIGURE 4.17: Comparison between the simulated vertical displacement at point A016VNW (see Figure 2.15 for the position) with the final calibration and the measured displacement. The average pressure in Pool A and Pool C between 2003 and 2021 are also provided.

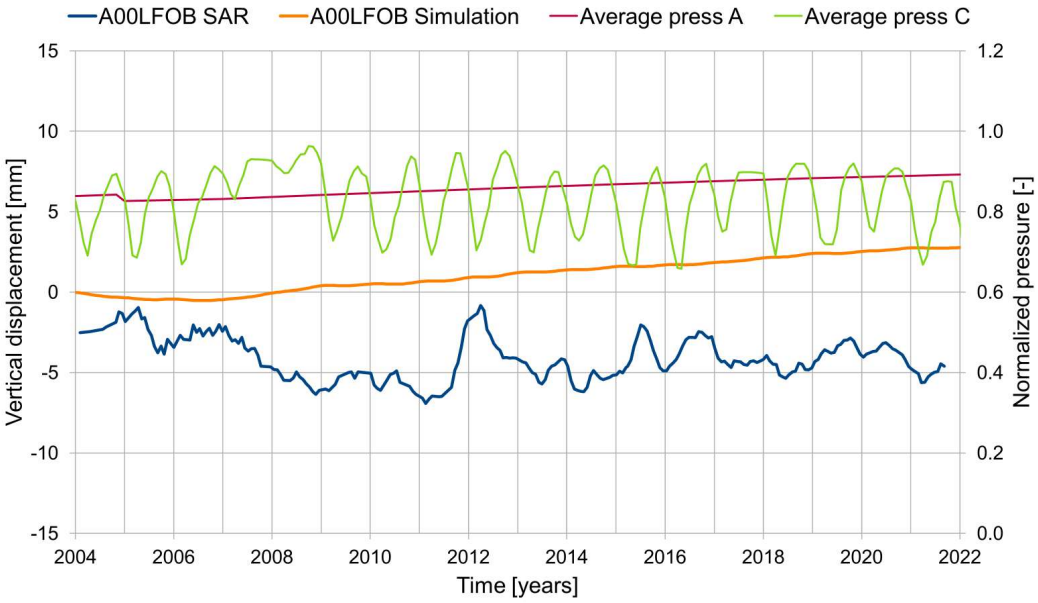

FIGURE 4.18: Comparison between the simulated vertical displacement at point A00LFOB (see Figure 2.15 for the position) with the final calibration and the measured displacement. The average pressure in Pool A and Pool C between 2003 and 2021 are also provided.

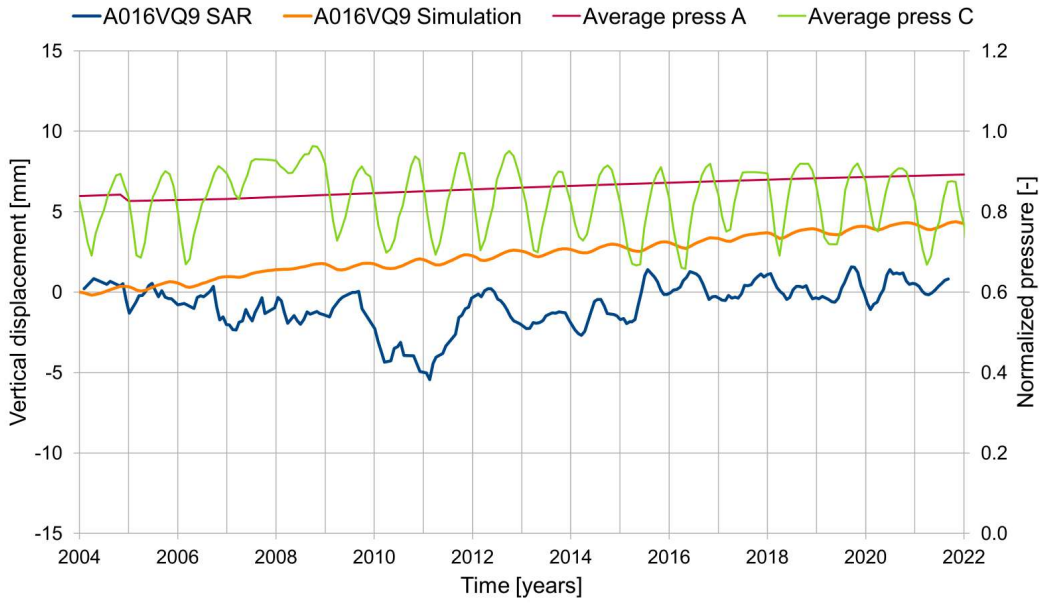

FIGURE 4.19: Comparison between the simulated vertical displacement at point A016VQ9 (see Figure 2.15 for the position) with the final calibration and the measured displacement. The average pressure in Pool A and Pool C between 2003 and 2021 are also provided.

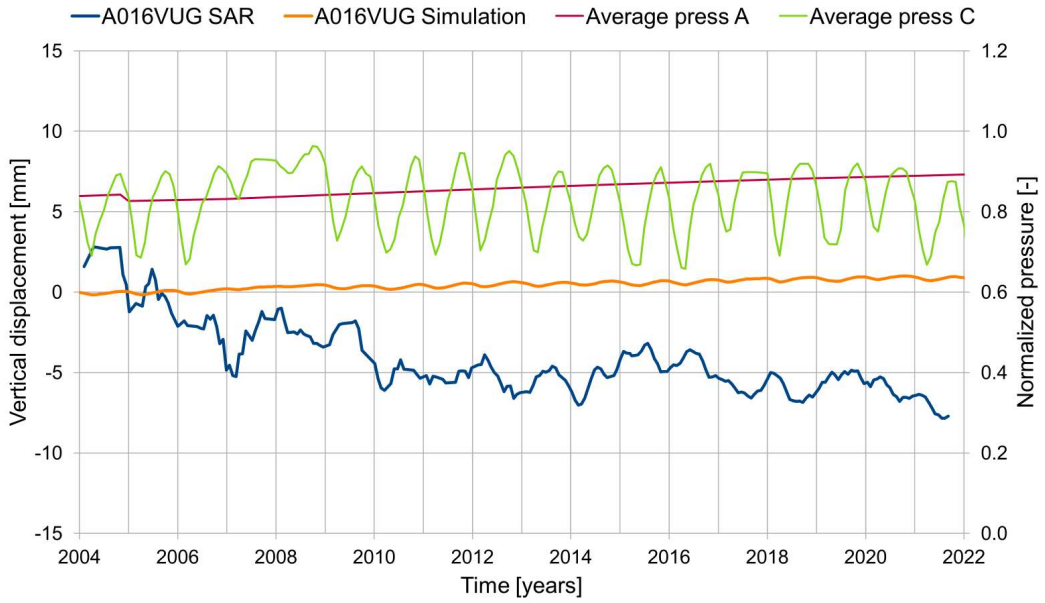

FIGURE 4.20: Comparison between the simulated vertical displacement at point A016VUG (see Figure 2.15 for the position) with the final calibration and the measured displacement. The average pressure in Pool A and Pool C between 2003 and 2021 are also provided.

4.3 Results

4.3.1 Displacements

One of the first outcomes that can be checked at the end of the simulation are the land displacements. The major concerns are relative to the last decades because in this period the storage activity was more developed, and it represents a model to follow in the coming years. Hence, the displacements in all the directions are shown from Figure 4.21 to Figure 4.23 for the representative storage phase from May 2015 to November 2015. Horizontal movements are in the order of a few millimeters, both in x (West - East) and y (South - North) directions. As expected during an injection phase, land surface moves away from the center of the reservoir where, instead, horizontal displacement nulls. Regarding the vertical displacements, the movement assumes positive values, as expected in this phase. The greatest movements are located at the center of the reservoir and do not exceed 4 mm.

For the production phase from November 2015 to May 2016 the simulated displacements are reported from Figure 4.24 to Figure 4.26. The displacements are in the opposite direction with respect to the storage cycle, so points are moving toward the center in the horizontal plane, while the vertical displacements show negative values meaning that the land surface is moving downward. In this case, however, the variations are even smaller than in the storage cycle, in fact the maximum vertical movement is lower than 2 mm.

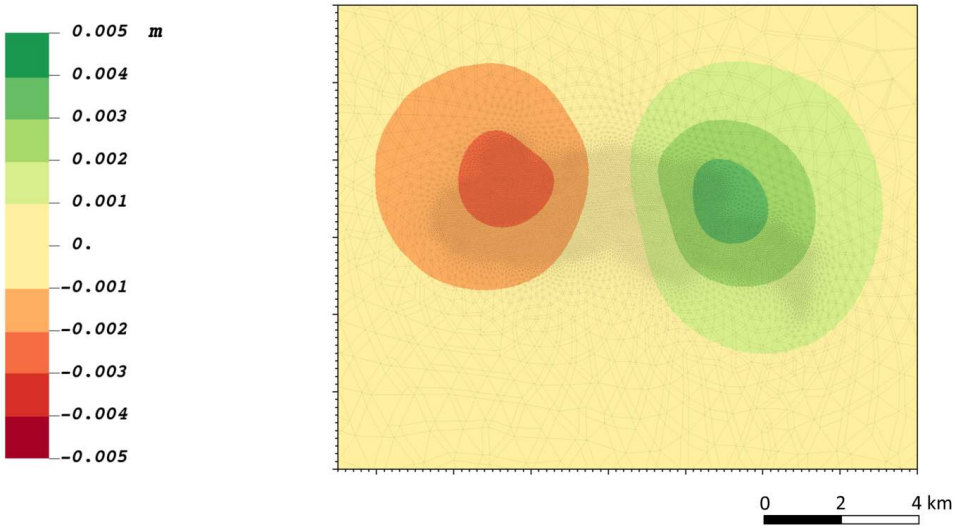

FIGURE 4.21: Displacement u_x (West - East) obtained from the geomechanical simulation during the storage phase from May 2015 to November 2015.

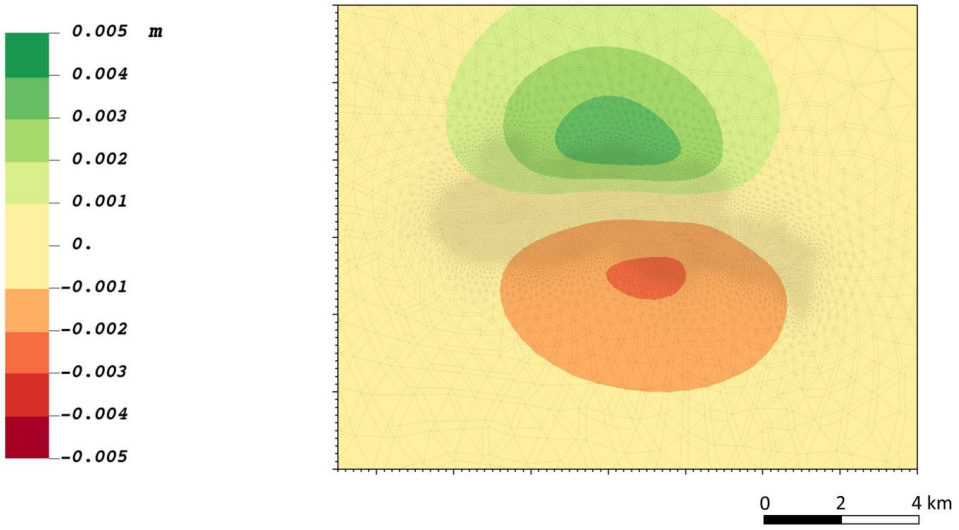

FIGURE 4.22: Displacement u_y (South - North) obtained from the geomechanical simulation during the storage phase from May 2015 to November 2015.

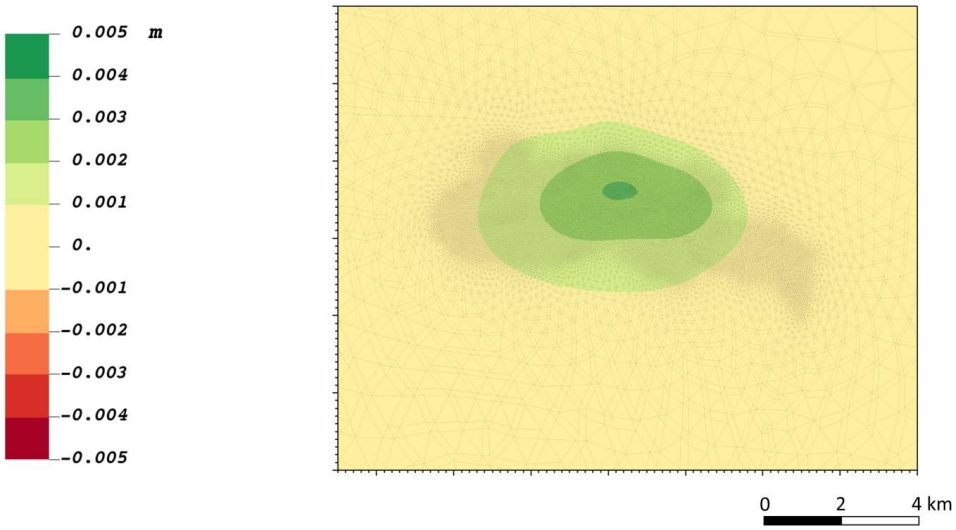

FIGURE 4.23: Displacement u_z obtained from the geomechanical simulation during the storage phase from May 2015 to November 2015.

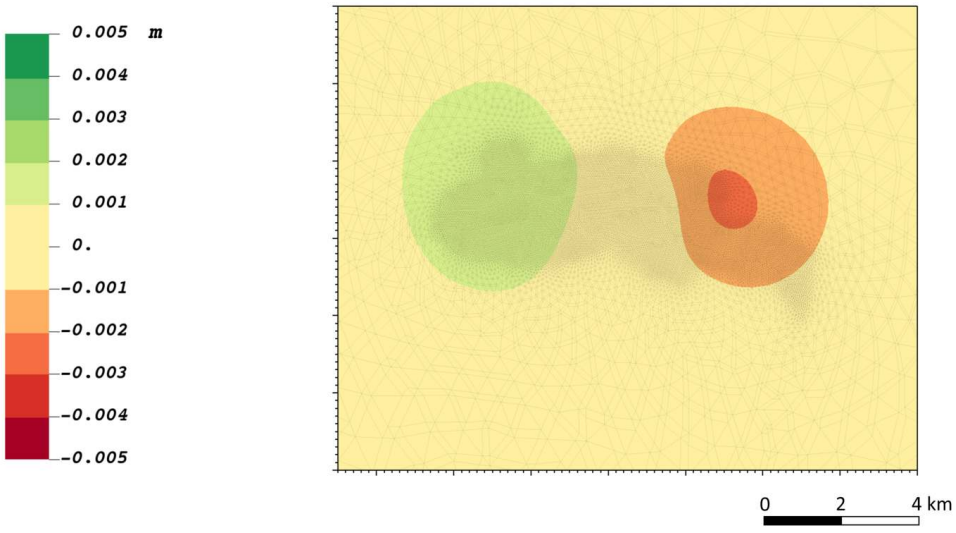

FIGURE 4.24: Displacement u_x (West - East) obtained from the geomechanical simulation during the production phase from November 2015 to May 2016.

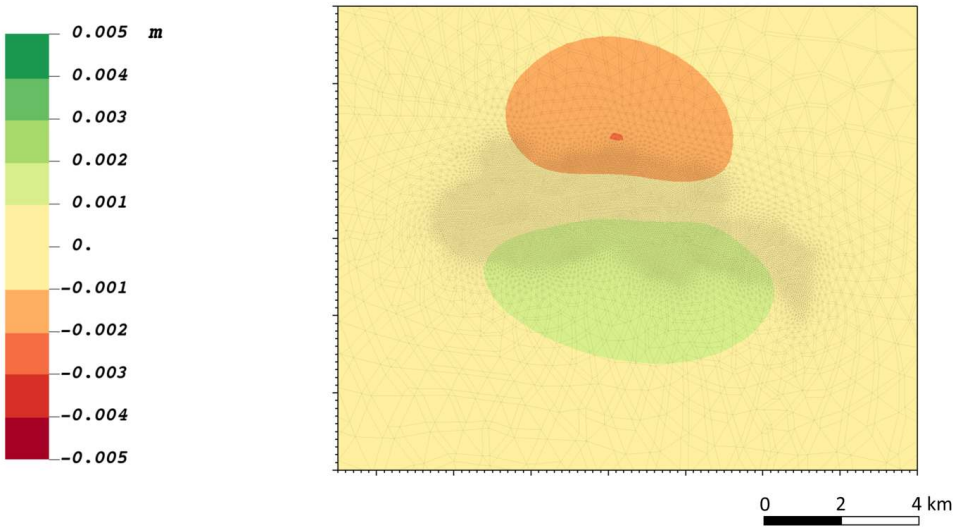

FIGURE 4.25: Displacement u_y (South - North) obtained from the geomechanical simulation during the production phase from November 2015 to May 2016.

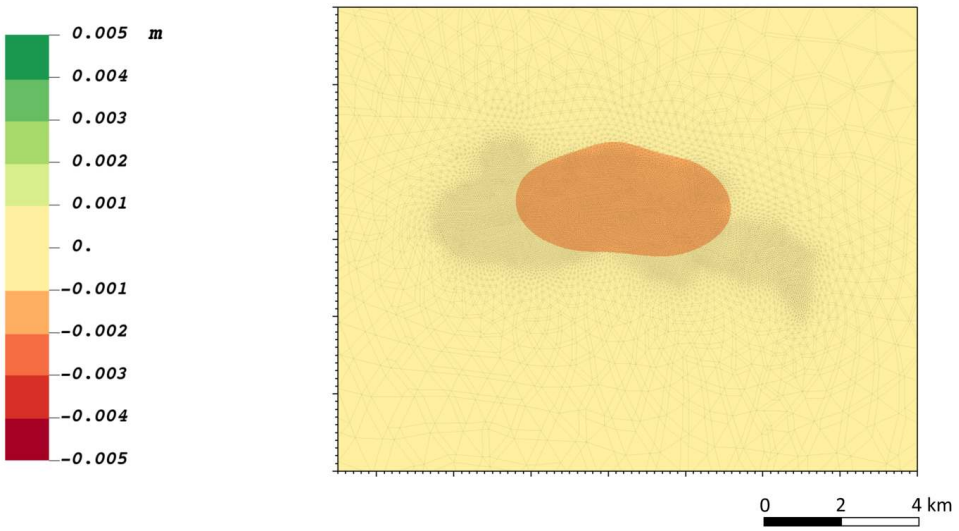

FIGURE 4.26: Displacement u_z obtained from the geomechanical simulation during the production phase from November 2015 to May 2016.

4.3.2 Stresses

The change of the stress field caused by the UGS activities is an important outcome of the model. Considering the same storage phase, the variations of normal stresses along the three principal directions on the two vertical sections traced in Figure 4.1 are presented from Figure 4.27 to Figure 4.32. The values are normalized with the initial average pressure of Pool C. Notice that the variation of σ_z is coherent with the pressure variation in Pool C, during that time interval. The stress change remains largely confined within this pool layer, with a very limited propagation to the surroundings. Moreover, the variation of σ_z is almost three times higher than the horizontal stresses variation, as expected from the confinement factor. The stress changes are also analyzed on the top of Pool C (Figures 4.33 - 4.35): it is evident that they do not propagate significantly above the top of the reservoir, or just for a very small portion but with almost negligible values.

The same analysis has been performed for the injection phase. In this case, the values are almost the same as the storage phase even though the variations show a negative sign because the stress and pressure are decreasing. Therefore, the considerations done before about the limited propagation outside Pool C and the ratio between vertical and horizontal stresses hold in the production phase too.

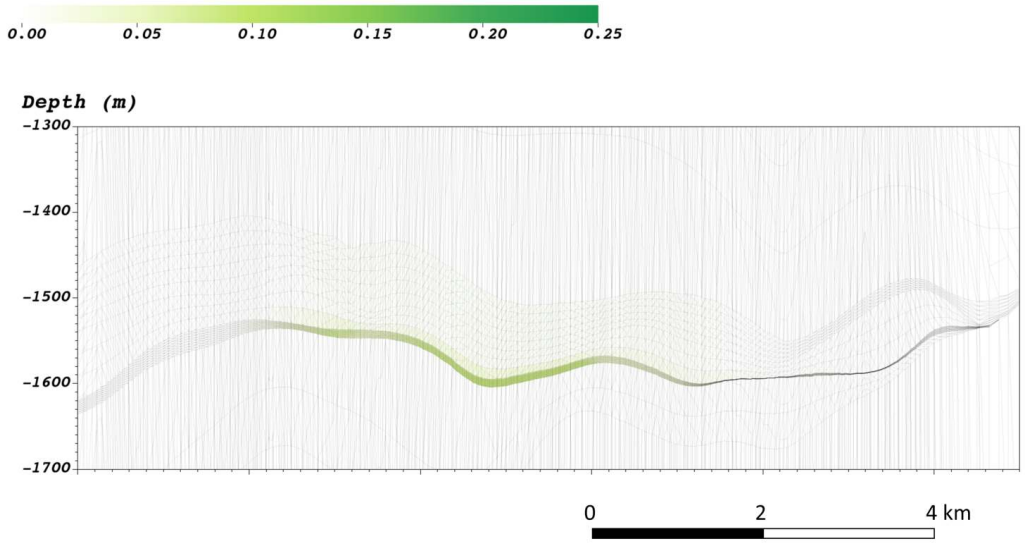

FIGURE 4.27: Normalized variation of stress σ_x along the section A-A traced in Figure 4.1 during the storage phase from May 2015 to November 2015. The vertical scale is exaggerated by a factor 10 with respect to the horizontal one.

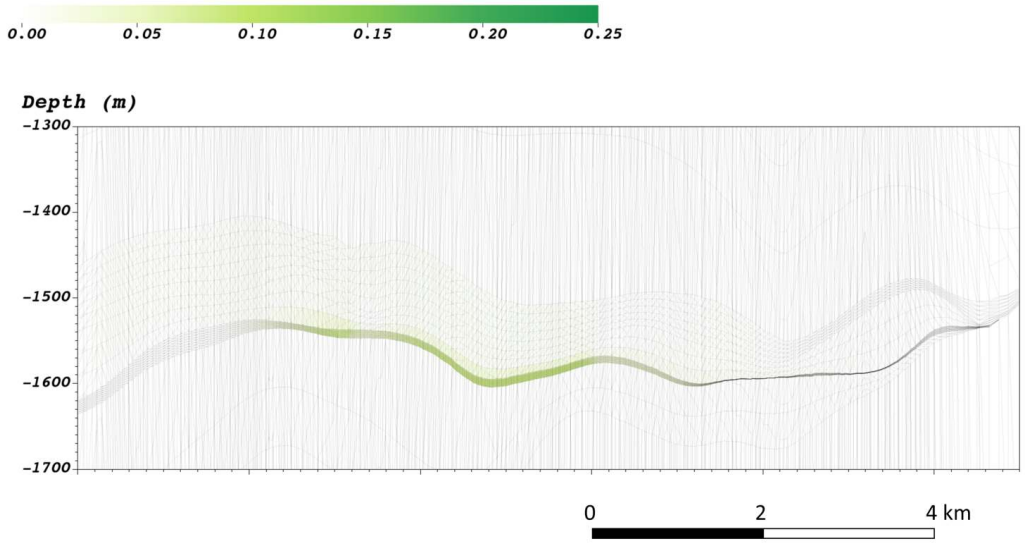

FIGURE 4.28: Normalized variation of stress σ_y along the section A-A traced in Figure 4.1 during the storage phase from May 2015 to November 2015. The vertical scale is exaggerated by a factor 10 with respect to the horizontal one.

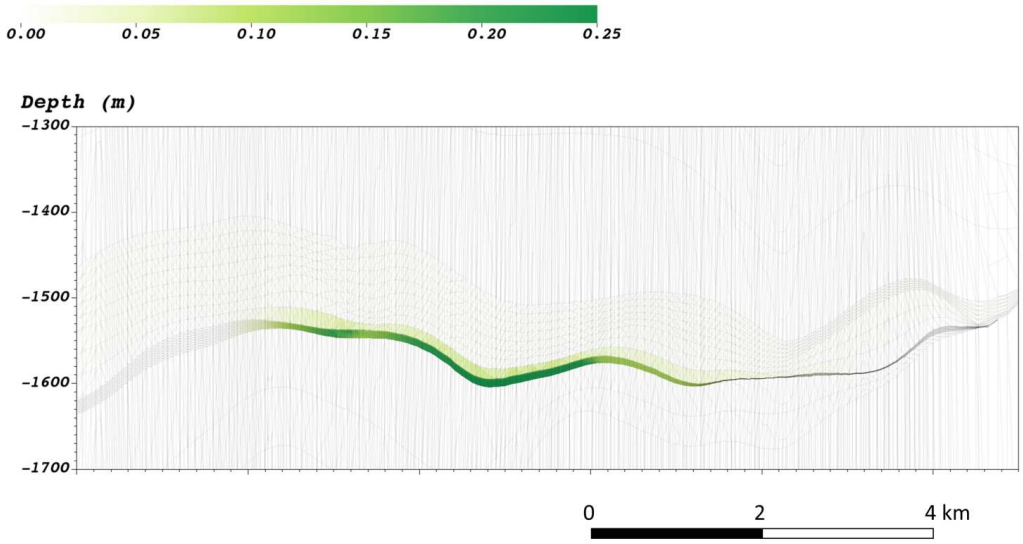

FIGURE 4.29: Normalized variation of stress σ_z along the section A-A traced in Figure 4.1 during the storage phase from May 2015 to November 2015. The vertical scale is exaggerated by a factor 10 with respect to the horizontal one.

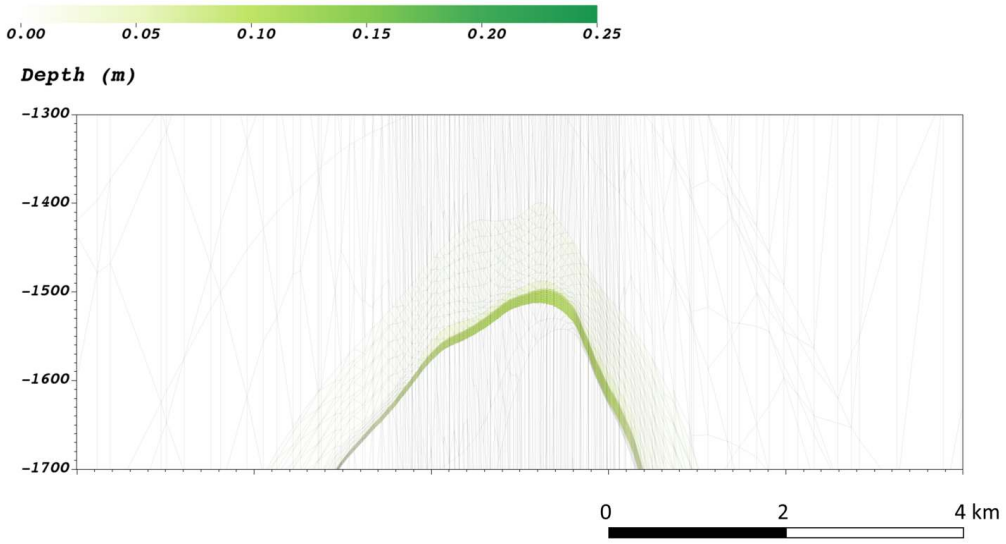

FIGURE 4.30: Normalized variation of stress σ_x along the section B-B traced in Figure 4.1 during the storage phase from May 2015 to November 2015. The vertical scale is exaggerated by a factor 10 with respect to the horizontal one.

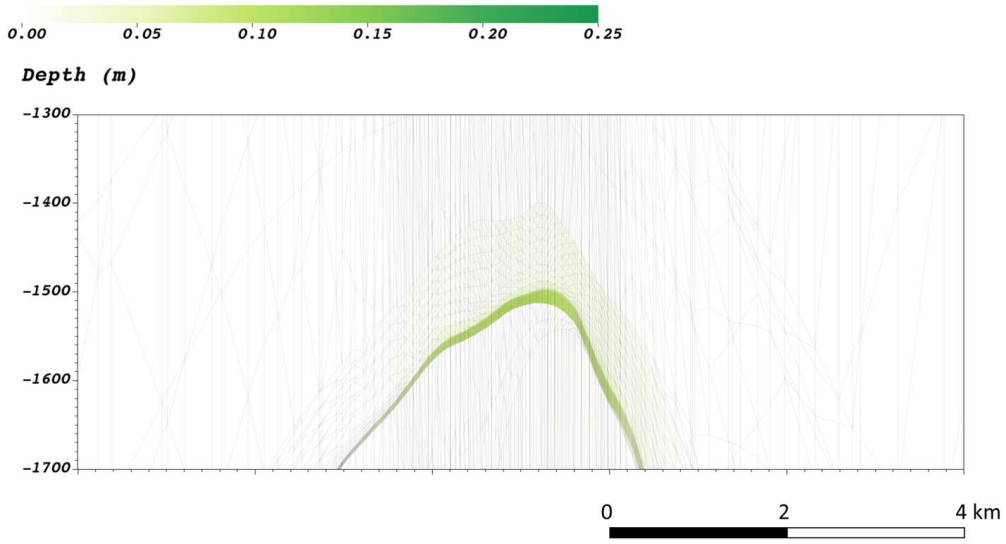

FIGURE 4.31: Normalized variation of stress σ_y along the section B-B traced in Figure 4.1 during the storage phase from May 2015 to November 2015. The vertical scale is exaggerated by a factor 10 with respect to the horizontal one.

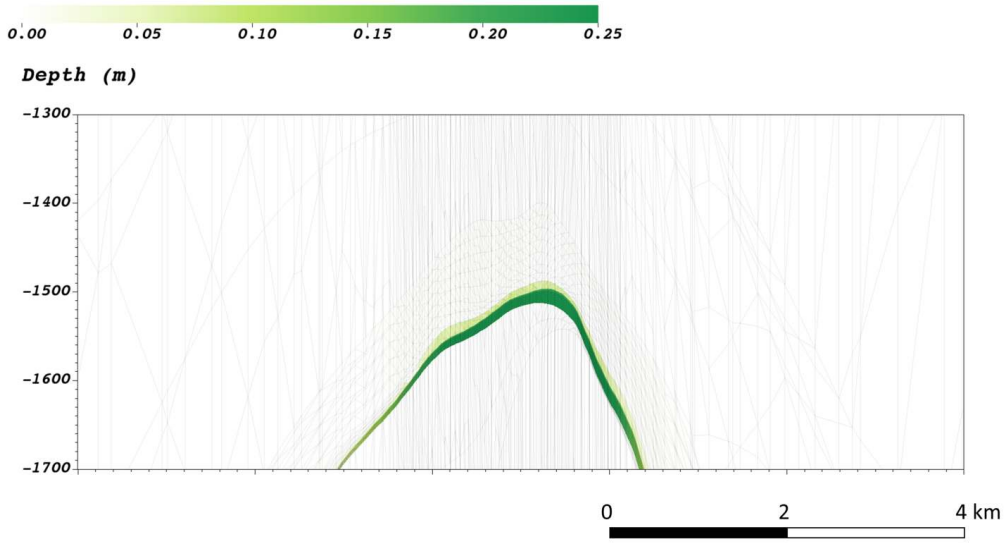

FIGURE 4.32: Normalized variation of stress σ_z along the section B-B traced in Figure 4.1 during the storage phase from May 2015 to November 2015. The vertical scale is exaggerated by a factor 10 with respect to the horizontal one.

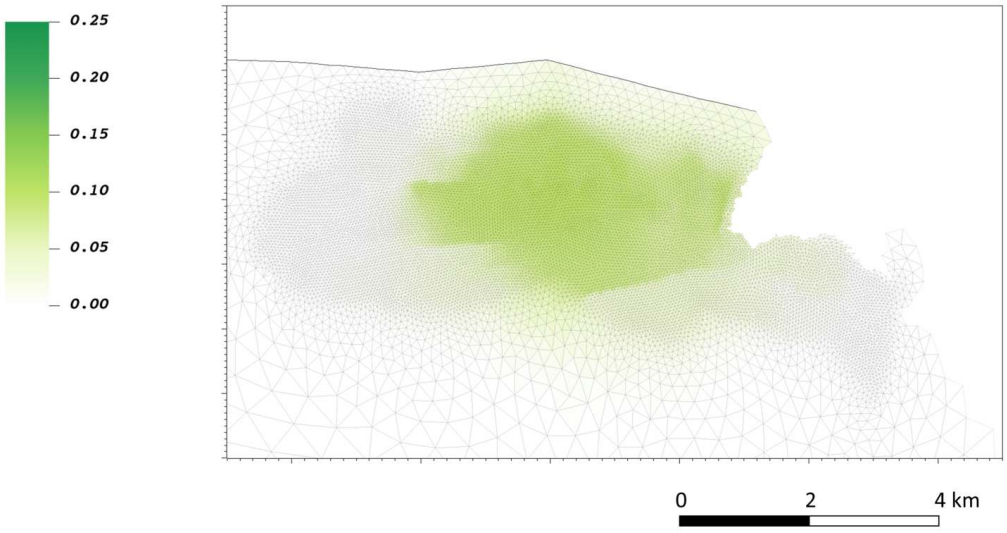

FIGURE 4.33: Normalized variation of stress σ_x at the top of Pool C during the storage phase from May 2015 to November 2015.

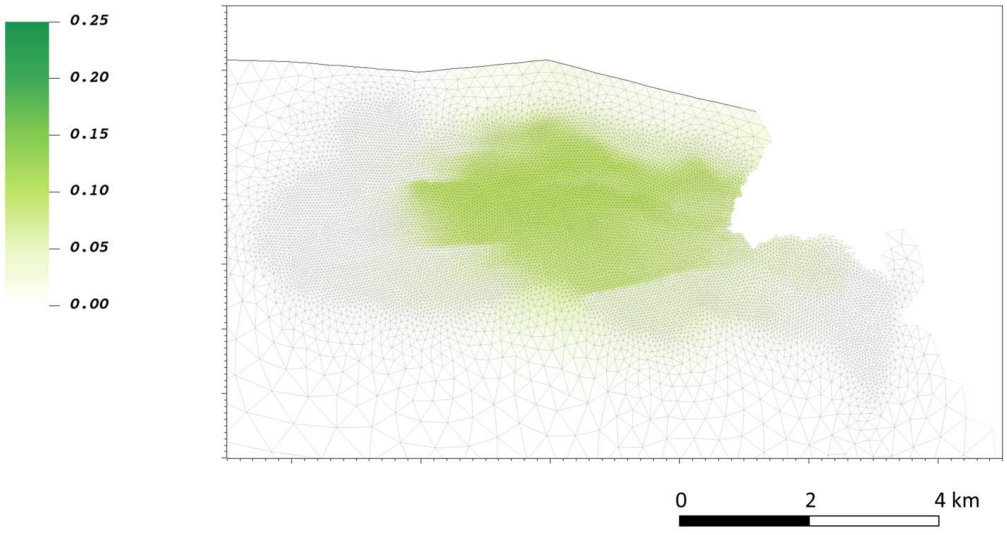

FIGURE 4.34: Normalized variation of stress σ_y at the top of Pool C during the storage phase from May 2015 to November 2015.

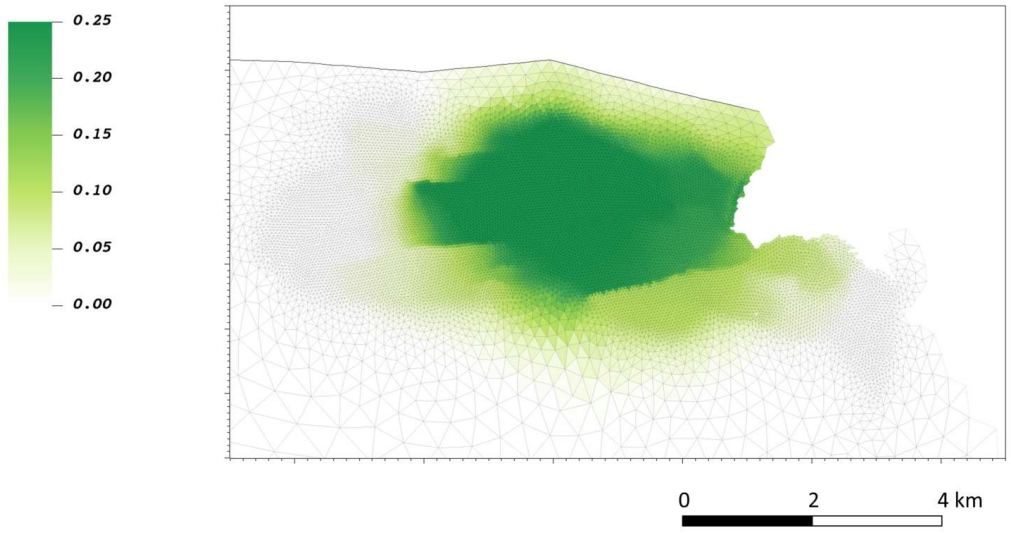

FIGURE 4.35: Normalized variation of stress σ_z at the top of Pool C during the storage phase from May 2015 to November 2015.

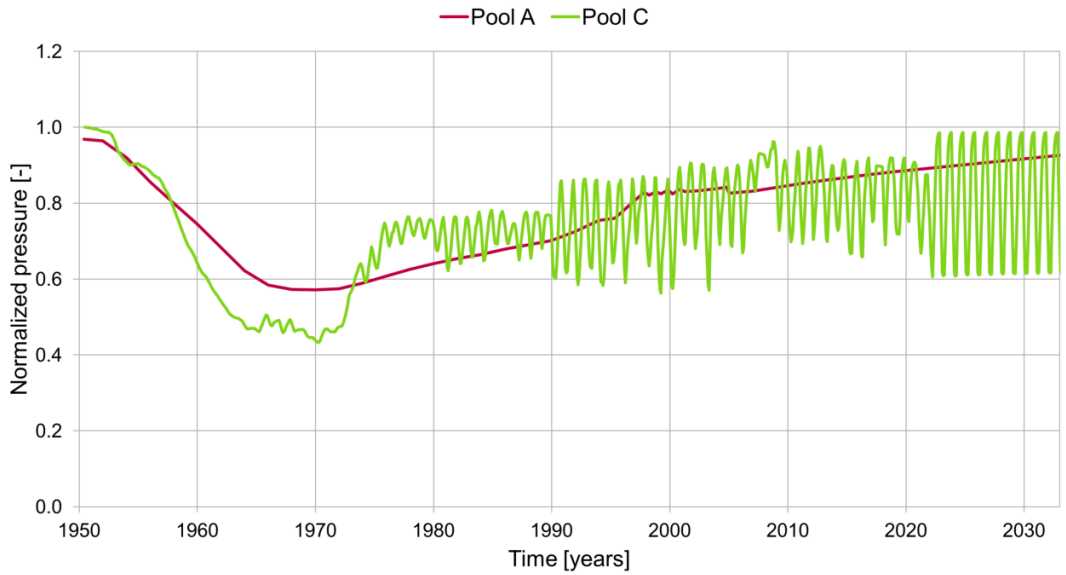

FIGURE 4.36: Behaviour over time of the normalized average pressure in Pool A and in Pool C considering also the forecast trend until 2033.

4.3.3 Forecast

As the storage activity is expected to continue in the next years, it is interesting to simulate the geomechanical effects associated to the future storage/production cycles. The average pressure behaviour until 2033 as provided by Eclipse is shown in Figure 4.36. In this scenario, the difference between the minimum and the maximum pressure is supposed to be greater than the one registered in the last years (from around 25% to 37%). As these data are only forecasts, the cycles are all identical.

The land displacement variations simulated during one of the storage cycles (Figures from 4.37 to 4.39) are similar to that computed for the year 2015 (Figures from 4.21 to 4.23). The variations are still limited to 5 mm, with values slightly greater as well as the extension of the area subject to land movements. This behavior is caused by the increase in pressure difference during seasonal cycles.

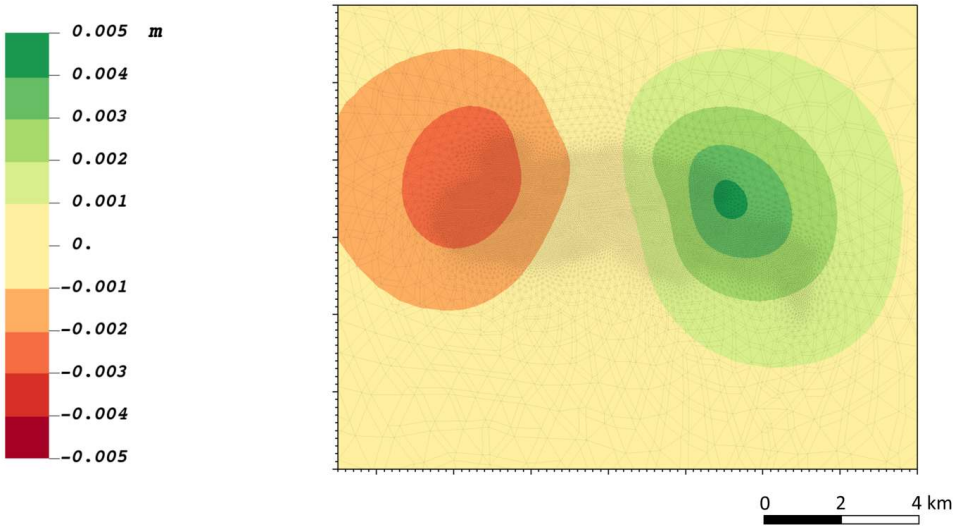

FIGURE 4.37: Displacement u_x obtained from the geomechanical simulation during the storage phase forecast from May 2025 to November 2025.

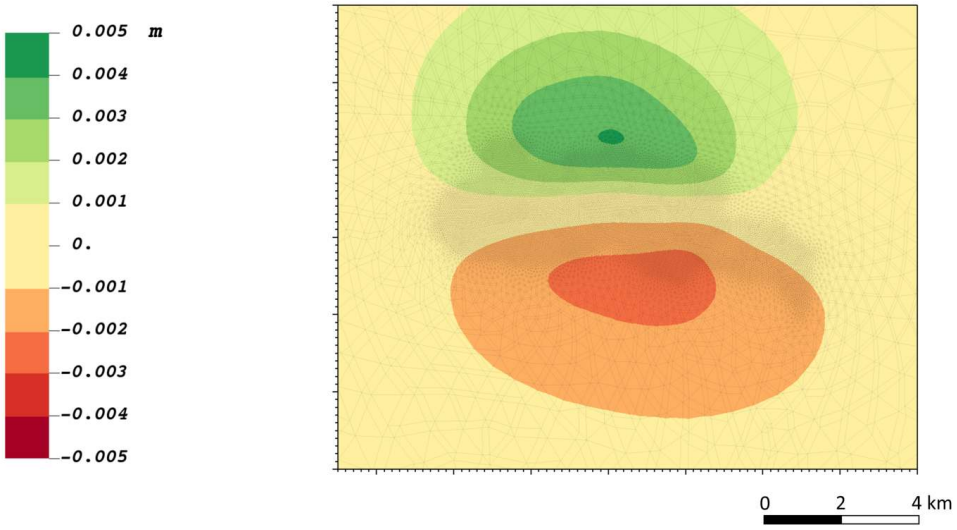

FIGURE 4.38: Displacement u_y obtained from the geomechanical simulation during the storage phase forecast from May 2025 to November 2025.

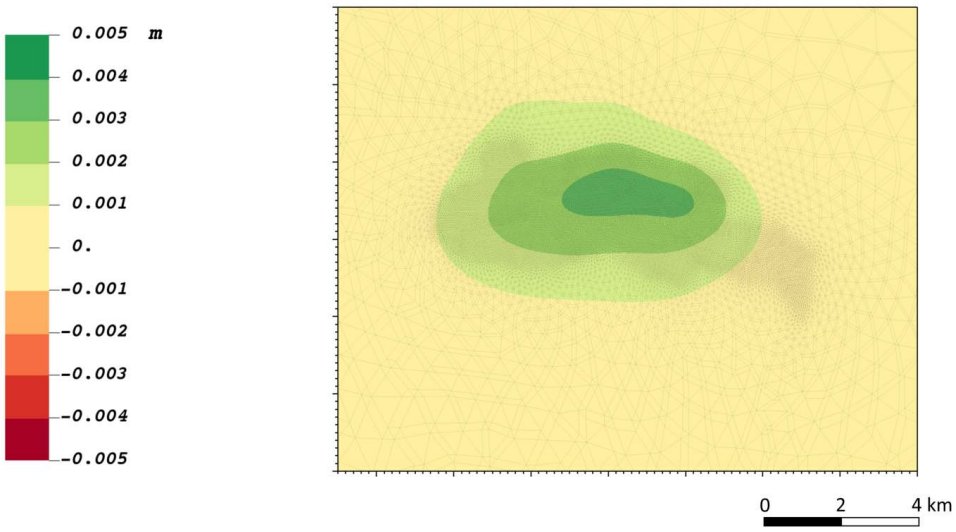

FIGURE 4.39: Displacement u_z obtained from the geomechanical simulation during the storage phase forecast from May 2025 to November 2025.

4.3.4 Fault activation

Finally, the simulation is run considering the presence of the faults, so using the mesh containing the IEs. As the results of the simulation regarding the land displacements and the stresses inside the reservoir have already been described, the main focus is now on the possible faults activation, in particular during the storage activity. For this reason, the simulation has been run only for one of the most recent full storage phase.

The results of the simulation show no relevant values on the safety parameters quantifying the possible activation of the faults, especially for the local discontinuities crossing the reservoir. To be sure that also regional faults are not affected by the storage activity, a new simulation has been run using a less refined mesh to reduce the computational burden and, simultaneously, giving us the possibility of a proper discretization (with elements not too distorted) of the fault surfaces (Figure 4.40). Based on the available geologic information, the faults extend vertically between -500 and -5,000 m and their initial state of stress, which is function of the depth, is reported in Figure 4.41 and Figure 4.42.

Recalling Section 3, the activation of a fault is related to the limit shear strength τ_L defined in Eq. (3.24). Hence, the factor of safety χ can be computed as

$$\chi = \frac{|\tau_s|}{\tau_L} = \frac{|\tau_s|}{c - \sigma_n \tan\varphi} \tag{4.2}$$

where τ_s is the actual shear strength.

The model outcome show that χ was estimated to be around 0.1 considering both the minimum and the maximum pressure values (Figure 4.43 and Figure 4.44). As χ ranges from 0 to 1, where 0 is representative of the most safe condition and 1 is the worst case, we can conclude that the UGS activities do not induce the activation of the regional faults.

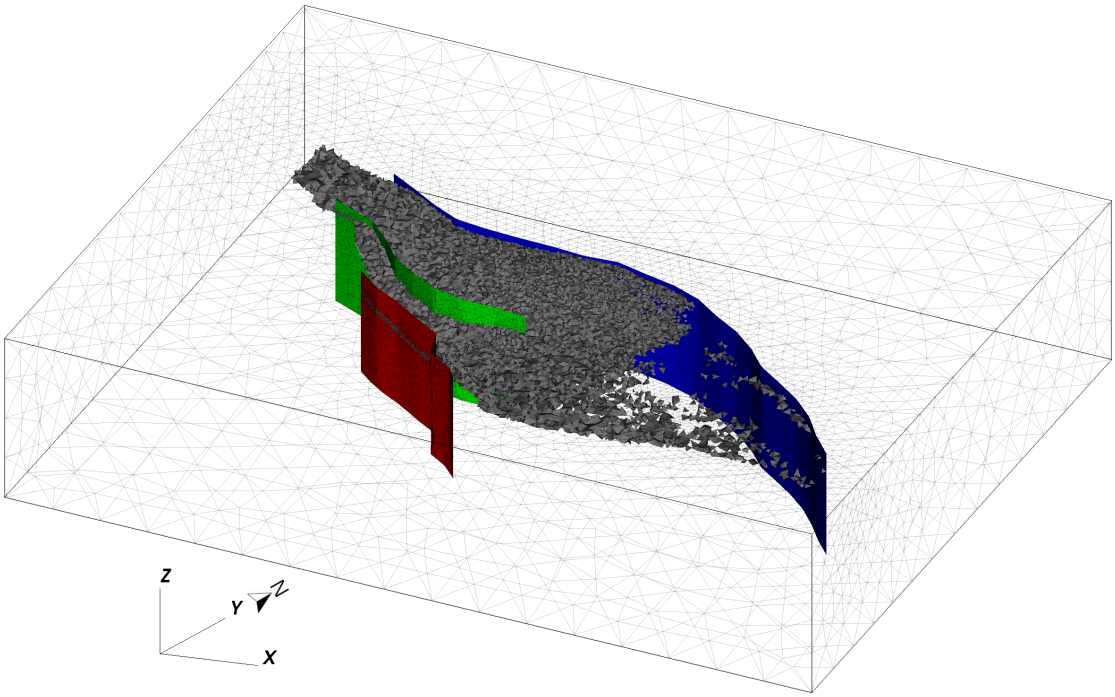

FIGURE 4.40: Axonometric view of the new coarse mesh used for the analysis of the possible activation the regional faults.

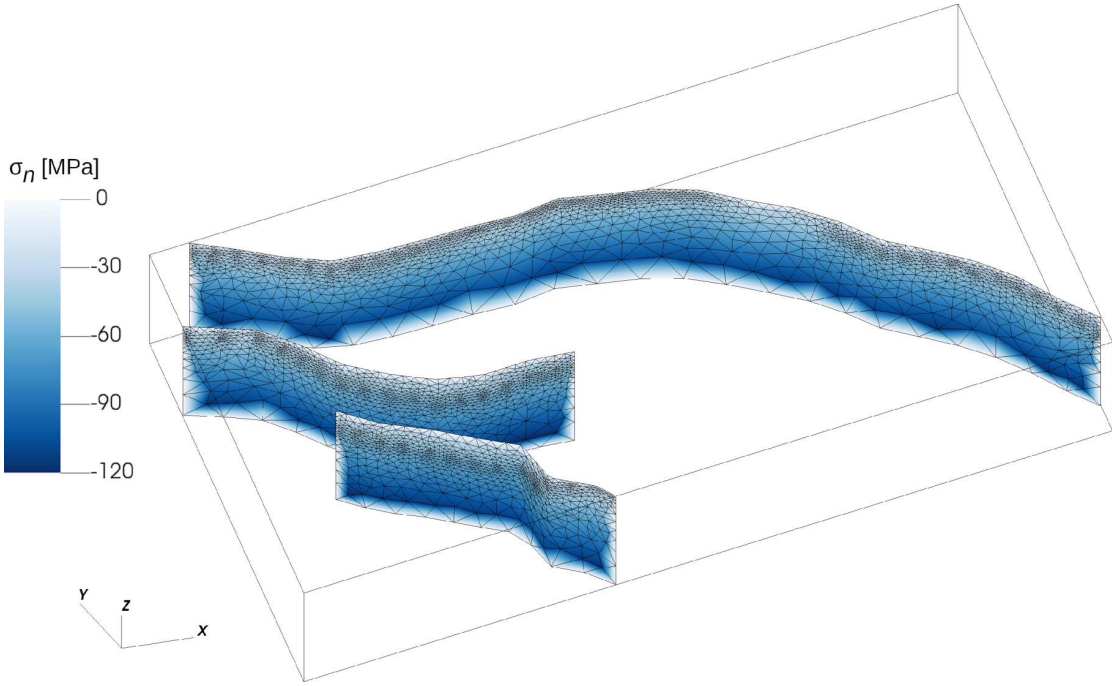

FIGURE 4.41: Initial normal stress on the regional faults surfaces.

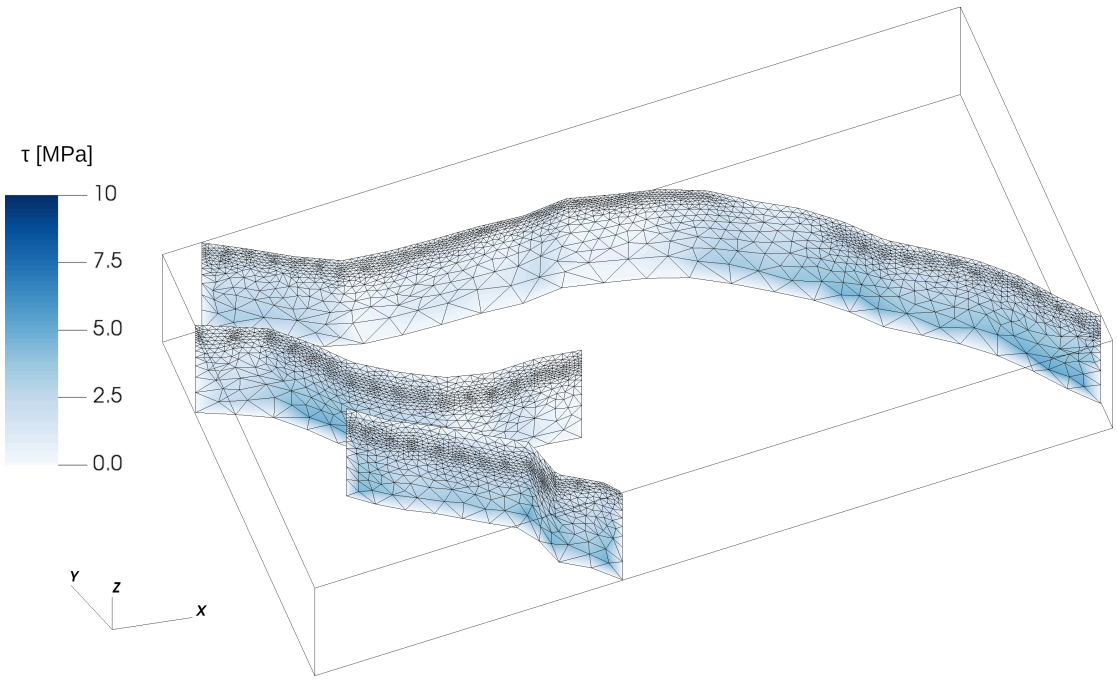

FIGURE 4.42: Initial shear stress on the regional faults surfaces.

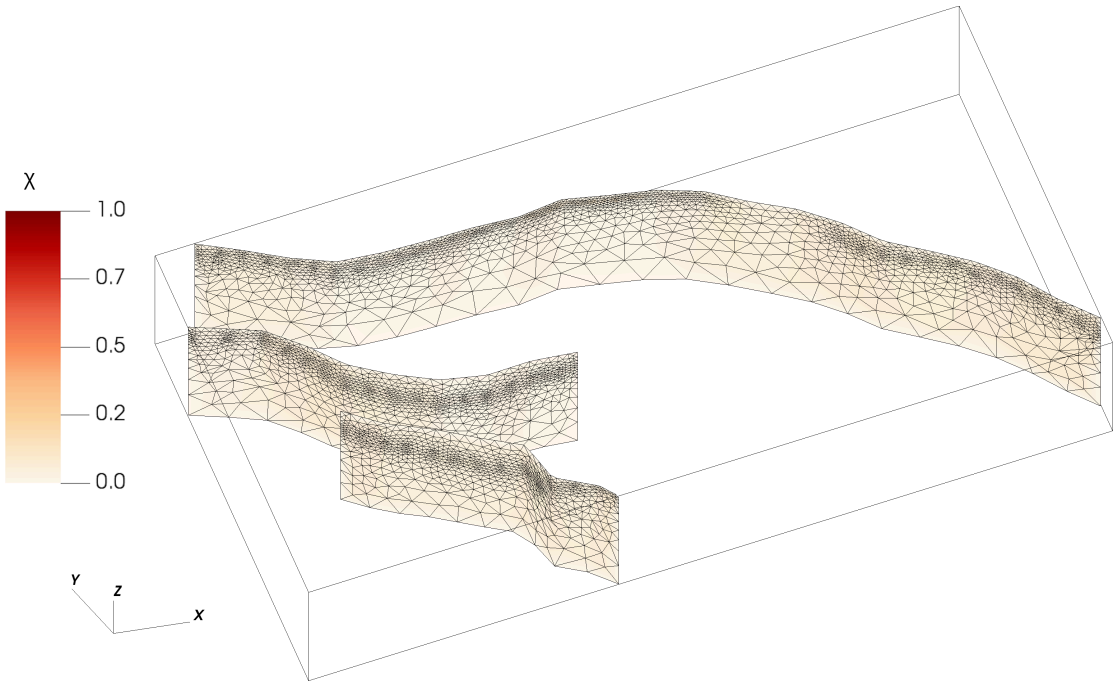

FIGURE 4.43: Value assumed by the factor of safety χ on the regional faults considering the scenario with the minimum pressure.

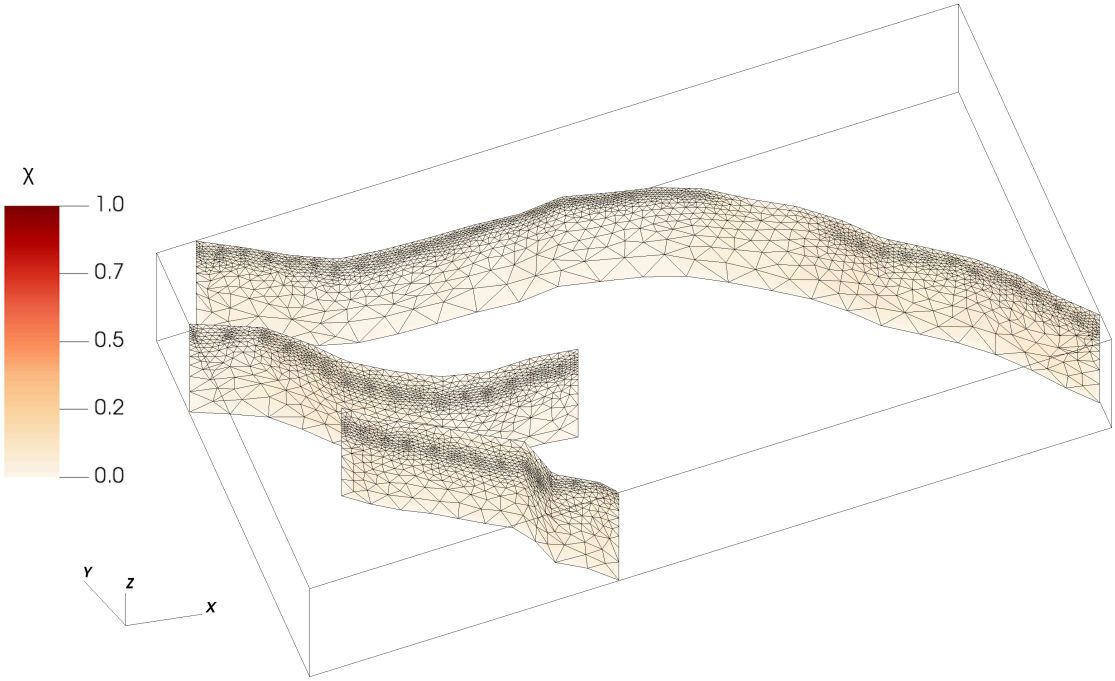

FIGURE 4.44: Value assumed by the factor of safety χ on the regional faults considering the scenario with the maximum pressure.

Chapter 5

Conclusions

The geomechanical simulation of UGS sites is fundamental to understand how the removal and injection of gas will affect the soil behaviour, especially in terms of land displacements and stress changes at depth, which can cause issues related to induced seismicity. The simulation of a case study in northern Italy is performed through the application of a one-way coupled approach linking a flow and a geomechanical simulator. The mathematical models are solved using the Finite Element method.

The flow model calibration has been performed estimating the value of the hydraulic conductivity that allows to satisfy the material balance equation, in order to propagate the pressure field to the hydraulically connected aquifers. The results are then used as a forcing factor in the geomechanical model, which has been calibrated considering a hypo-plastic constitutive relationship for the layers with pressure variation and a linear elastic law for the surrounding rock. The value of the compressibility ratio c_R has been set equal to 5 for Pool A and the interlayer, and 3 for Pool C where UGS activities are in operation. The results from the calibration show that, for the radar targets within the trace of the reservoir, the model is able to reproduce in a very good way the measured displacements.

The results of the geomechanical simulation have been analyzed considering the variations during the UGS phase and, specifically, the difference between the minimum and maximum values registered for the removal/injection period between May 2015 and May 2016. Land displacements do not exceed 4 mm, both in the vertical and horizontal directions, and are concentrated above the center of the reservoir. The fact that they are less evident during the production phase can be explained considering that only in Pool C storage activities are in operation, while Pool A is left to natural

re-pressurization. Hence, their behaviour are in contrast during winter and so the subsidence effect is reduced. On the contrary, the uplift during summer is more visible. Considering the forecast cycles, where the pressure variation is supposed to increase, the displacements are still limited to 5 mm. The stress change do not propagate significantly outside the boundary of Pool C, both in the vertical and horizontal directions, and the vertical variation is consistent with the pressure difference. Concerning the problem of the possible fault reactivation, the local discontinuities show no relevant values in the safety parameters. Moreover, the safety factor of regional faults results equal to 0.1, very close to the safest condition, leading to the conclusion that UGS activities are not causing problems of induced seismicity in the analyzed reservoir.

The following stages of this work could include, but are not limited to, a sensitivity analysis of the most relevant parameters. Considering also the parameters that have not yet been calibrated, the outcome could result in a more accurate knowledge of the subsurface response to human activities. Furthermore, the analysis of the possible fault reactivation was limited to a single storage cycle, although a simulation starting from the primary production phase would complemented the modeling investigation.

Bibliography

Argus Holdings, L. *Argus ONE User's Guide*. Jericho, NJ, USA, 1997. URL http://www.argusone.com/pub/OnLineDocs/ArgusONE_UsersGuide.pdf.

Baú, D., Ferronato, M., Gambolati, G., and Teatini, P. Basin-scale compressibility of the northern Adriatic by the radioactive marker technique. *Géotechnique*, 52:605–616, 10 2002. doi: 10.1680/geot.2002.52.8.605.

Biot, M. A. General Theory of Three-Dimensional Consolidation. *Journal of Applied Physics*, 12:155–164, 02 1941. doi: 10.1063/1.1712886.

Cornot-Gandolphe, S. Underground Gas Storage in the World - 2018 Status. Technical report, Cedigaz, 2018.

Ferronato, M., Gambolati, G., Teatini, P., and Baú, D. Unloading-reloading uniaxial compressibility of deep reservoirs by marker measurements. In *Proceedings of the 11th International FIG Symposium on Deformation Measurements*, pages 341–346. Geod. and Geod. Appl. Lab., Dep. of Civ. Eng., Univ. of Patras, Patras, Greece, 2003.

Ferronato, M., Gambolati, G., and Teatini, P. On the role of reservoir geometry in waterdrive hydrodynamics. *Journal of Petroleum Science and Engineering*, 44:205–221, 11 2004. doi: 10.1016/j.petrol.2004.04.001.

Ferronato, M., Castelletto, N., Gambolati, G., Janna, C., and Teatini, P. II cycle compressibility from satellite measurements. *Géotechnique*, 63:479–486, 05 2013. doi: 10.1680/geot.11.p.149.

Franceschini, A. *Formulazione lagrangiana del problema del contatto applicato a faglie geologiche*. PhD thesis, Università degli Studi di Padova, 2014.

Franceschini, A., Ferronato, M., Janna, C., and Teatini, P. A novel Lagrangian approach for the stable numerical simulation of fault and fracture mechanics. *Journal of Computational Physics*, 314:503–521, 06 2016. doi: 10.1016/j.jcp.2016.03.032.

Gambolati, G. and Ferronato, M. *Lezioni di metodi numerici per l'ingegneria*. Edizioni Progetto, second edition, 2015.

Gambolati, G., Gatto, P., and Ricceri, G. Land subsidence due to gas/oil removal in layered anisotropic soils by a finite element model. In *Proceedings of the 3rd International Symposium on Land Subsidence*, volume 151, pages 29–42. IAHS, 1984.

Gambolati, G., Teatini, P., Baú, D., and Ferronato, M. Importance of poroelastic coupling in dynamically active aquifers of the Po River Basin, Italy. *Water Resources Research*, 36:2443–2459, 09 2000. doi: 10.1029/2000wr900127.

Goodman, R. E., Taylor, R. L., and Brekke, T. L. A Model for the Mechanics of Jointed Rock. *Journal of the Soil Mechanics and Foundations Division*, 94:637–659, 05 1968. doi: 10.1061/jsfeaq.0001133.

Orlic, B., Wassing, B., and Geel, C. Field Scale Geomechanical Modeling for Prediction of Fault Stability During Underground Gas Storage Operations in a Depleted Gas Field in the Netherlands. In *Proceedings of the 47th US Rock Mechanics / Geomechanics Symposium*, volume All Days. ARMA, 06 2013.

Schlumberger. *ECLIPSE Reference Manual*, 2014. URL http://www.ipt.ntnu.no/~kleppe/TPG4150/EclipseReferenceManual.pdf.

Settari, A., Walters, D. A., Stright, D. H., and Aziz, K. Numerical Techniques Used for Predicting Subsidence Due to Gas Extraction in the North Adriatic Sea. *Petroleum Science and Technology*, 26:1205–1223, 06 2008. doi: 10.1080/10916460701833889.

Teatini, P., Castelletto, N., Ferronato, M., Gambolati, G., Janna, C., Cairo, E., Marzorati, D., Colombo, D., Ferretti, A., Bagliani, A., and Bottazzi, F. Geomechanical response to seasonal gas storage in depleted reservoirs: A case study in the Po River basin, Italy. *Journal of Geophysical Research: Earth Surface*, 116, 04 2011. doi: 10.1029/2010jf001793.

Teatini, P., Baú, D., and Gambolati, G. Water-gas dynamics and coastal land subsidence over Chioggia Mare field, northern Adriatic Sea. *Hydrogeology Journal*, 8:462–479, 10 2000. doi: 10.1007/s100400000092.